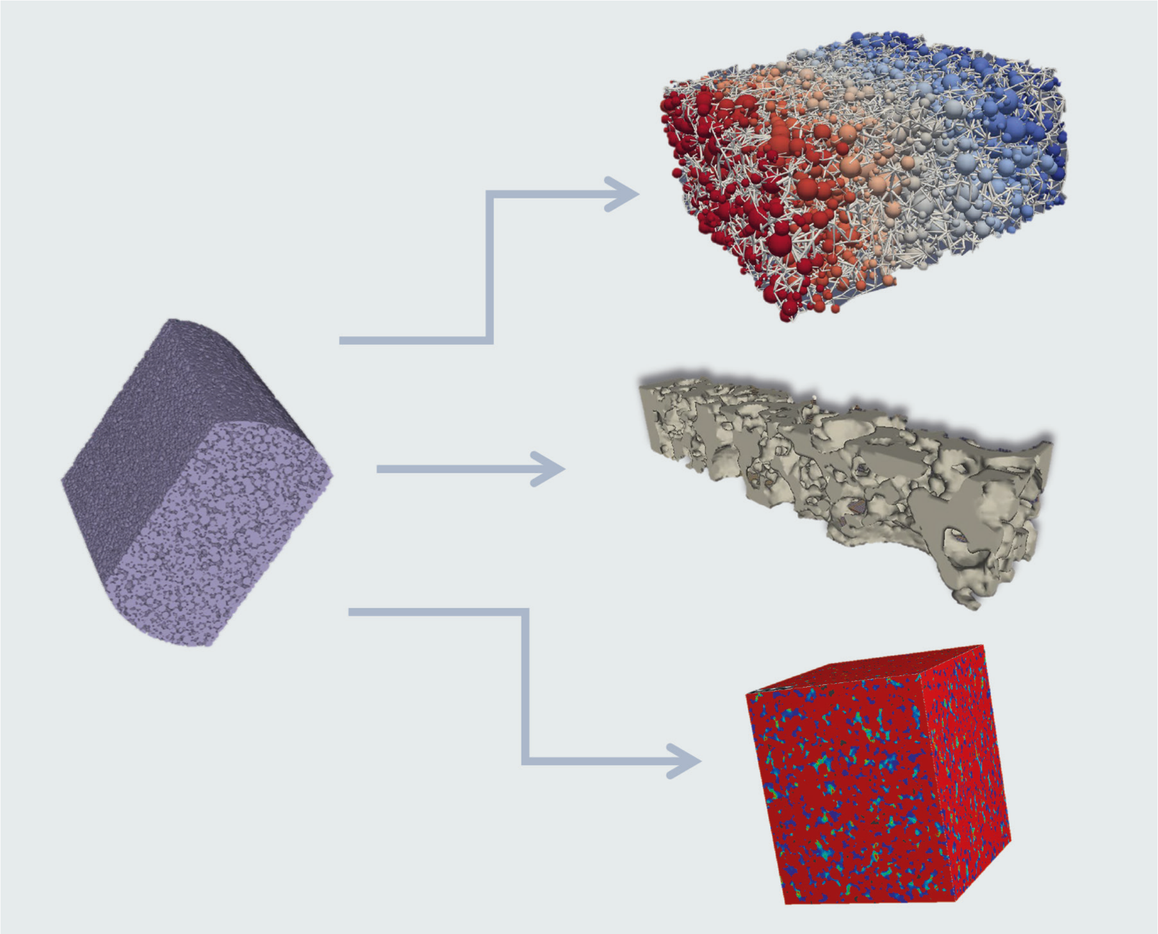

Two-phase Flow in Porous Transport Layers of Polymer Electrolyte Membrane Electrolysers

Deepjyoti Borah

Energie & Umwelt / Energy & Environment
Band / Volume 546
ISBN 978-3-95806-564-2

Mitglied der Helmholtz-Gemeinschaft

JÜLICH
Forschungszentrum

Schriften des Forschungszentrums Jülich
Reihe Energie & Umwelt / Energy & Environment Band / Volume 546

Forschungszentrum Jülich GmbH
Institut für Energie- und Klimaforschung
Elektrochemische Verfahrenstechnik (IEK-14)

Two-phase Flow in Porous Transport Layers of Polymer Electrolyte Membrane Electrolysers

Deepjyoti Borah

Schriften des Forschungszentrums Jülich
Reihe Energie & Umwelt / Energy & Environment Band / Volume 546

ISSN 1866-1793 ISBN 978-3-95806-564-2

Bibliografische Information der Deutschen Nationalbibliothek.
Die Deutsche Nationalbibliothek verzeichnet diese Publikation in der Deutschen Nationalbibliografie; detaillierte Bibliografische Daten sind im Internet über http://dnb.d-nb.de abrufbar.

Herausgeber und Vertrieb: Forschungszentrum Jülich GmbH
Zentralbibliothek, Verlag
52425 Jülich
Tel.: +49 2461 61-5368
Fax: +49 2461 61-6103
zb-publikation@fz-juelich.de
www.fz-juelich.de/zb

Umschlaggestaltung: Grafische Medien, Forschungszentrum Jülich GmbH

Druck: Grafische Medien, Forschungszentrum Jülich GmbH

Schriften des Forschungszentrums Jülich
Reihe Energie & Umwelt / Energy & Environment, Band / Volume 546

D 82 (Diss. RWTH Aachen University, 2021)

ISSN 1866-1793
ISBN 978-3-95806-564-2

Abstract

Polymer electrolyte membrane (PEM) water electrolysis is an important technology for the electrochemical splitting of water. Inside PEM electrolysers, the porous transport layers (PTL) facilitate mass-transport and electric conduction. An understanding of the gas-water flow inside the PTL is a prerequisite to improving cell performance. To the best of the author's knowledge, experimentally measured relative permeability of PEM electrolyser PTLs has not yet been published in literature. This thesis aims to achieve this through experiments and to validate results from simulations.

For experimental characterisation, six different PTLs were chosen, and similar techniques for measurements of geological samples were considered. However, their microscale size presents unique challenges in applying these techniques directly. Hence, a new test cell was developed, and both absolute, and relative permeability were determined.

Computer tomography (CT) images were taken for all six samples to generate 3D-models of the porous PTL structures. The flow simulations were performed using four different tools: pore network model (OpenPNM), voxel-based computation (GeoDict), conventional computational fluid dynamics (ANSYS Fluent), and Lattice Boltzmann method (Palabos). Two-phase flow simulations were performed only with OpenPNM and ANSYS Fluent. Out of the four methods, GeoDict and Palabos required the minimum amount of preprocessing. Pore network method was the least computationally expensive method. ANSYS Fluent required the most amount of preprocessing and computation time. Three-dimensional meshes were created using different open-source and proprietary tools, but only a relatively small portion of the image stack could be used due to computational limitations. GeoDict and Palabos produced nearly identical results. Except for ANSYS Fluent, all the other tools computed through-plane permeability values close to experimental values. The simulations did not match the experimental in-plane permeability values. Relative permeability was computed from pore network simulations. Computed air relative permeability curves and the respective measurements agreed. The water relative permeability curves did not match experiments, although both were very small in magnitude.

It is observed that relative permeability saturation correlations used in literature are not experimentally validated. This work produced experimental relative permeability curves for sintered titanium porous transport layers of PEM electrolyser systems for the first time.

Kurzfassung

Die Polymer-Elektrolyt-Membran (PEM)-Wasserelektrolyse ist eine wichtige Technologie zur elektrochemischen Aufspaltung von Wasser. In PEM-Elektrolyseuren ermöglichen die porösen Transportschichten (PTL) den Stofftransport und die elektrische Leitung. Ein tiefergehendes Verständnis des Gas-Wasser-Flusses innerhalb der PTL ist eine Voraussetzung für die Verbesserung der Zellleistung. Nach dem besten Wissen des Autoren wurde die experimentell gemessene relative Permeabilität von PEM-Elektrolyseur-PTLs in der Fachliteratur noch nicht veröffentlicht. Ziel dieser Arbeit ist es, dies durch Experimente zu erreichen und die Ergebnisse durch Simulationen zu validieren.

Für die experimentelle Charakterisierung wurden sechs verschiedene PTLs ausgewählt und ähnliche Techniken für die Vermessung von geologischen Proben berücksichtigt. Ihre geringere Größe stellt jedoch einzigartige Herausforderungen für die direkte Anwendung dieser Techniken dar. Daher wurde eine neue Testzelle entwickelt und sowohl die absolute als auch die relative Permeabilität wurden bestimmt.

Für alle sechs Proben wurden Computertomographie-Aufnahmen gemacht, um 3D-Modelle der porösen PTL-Strukturen zu generieren. Die Strömungssimulationen wurden mit vier verschiedenen Methoden durchgeführt: Porennetzwerkmodell (OpenPNM), voxelbasierte Berechnung (GeoDict), konventionelle numerische Strömungsberechnung (ANYSY Fluent) und Lattice-Boltzmann-Methode (Palabos). Zweiphasen-Strömungssimulationen wurden nur mit OpenPNM und ANSYS Fluent durchgeführt. Von den vier Methoden erforderten GeoDict und Palabos den geringsten Vorverarbeitungsaufwand. Die Porennetzwerk-Methode war die am wenigsten rechenaufwändige Methode. ANSYS Fluent erforderte den größten Aufwand an Vorverarbeitung und Rechenzeit. Dreidimensionale Netze wurden mit verschiedenen Open-Source- und proprietären Programmen erstellt; aber nur ein kleiner Teil des Bildstapels konnte aufgrund beschränkter Rechenkapazitäten verwendet werden. GeoDict und Palabos lieferten nahezu identische Ergebnisse. Mit Ausnahme von ANSYS Fluent berechneten alle anderen Tools Permeabilitätswerte durch die Ebene, die nahe an den experimentellen Werten lagen. Die Simulationen der Permeabilitätswerte in der Ebene stimmten nicht mit den experimentellen Werten überein und zeigten keine ausgeprägte Anisotropie. Die relative Permeabilität wurde aus Porennetzwerk-Simulationen berechnet. Die berechneten Kurven der relativen Luftdurchlässigkeit und die Messungen zeigten eine gute Übereinstimmung. Die Kurven der relativen Permeabilität von Wasser stimmten nicht mit den Experimenten überein, obwohl deren Größenordnung jeweils sehr klein war.

Es ist zu beobachten, dass die in der Literatur verwendeten Korrelationen der relativen Permeabilität für die Sättigung nicht experimentell validiert sind. In dieser Arbeit wurden experimentelle relative Permeabilitätskurven für gesinterte poröse Titantransportschichten von PEM-Elektrolyseuren zum ersten Mal vorgestellt.

Acknowledgement

I would like to express my sincere gratitude to Prof. Dr. Werner Lehnert for being my advisor. I cannot imagine finishing this project without his support and guidance over the last five years. There were many moments of doubt, and it was his support that really kept me going. I am also thankful to Prof. Dr. Singheiser and Prof. Dr. Corves for being part of my exam committee.

I am thankful to Dr. Martin Müller for his support. I thank Dieter Froning for being so supportive. He has helped me a lot since the days of my master studies. My sincere thanks to Richard Wegner and Nobert Commerscheidt. I am particularly indebted to Walter Zwaygardt for being such a wonderful person. All those long experiments would not have been possible without him.

I thank my friends Sayed, Edward, Ali and Cinar. Sayed is one of the most helpful persons I have known. I cannot thank Edward enough for all the discussions we had together and for being such a good friend. I also thank my colleagues Ulla Panchenko and Michael Höh, who have helped me in my PhD project.

I am grateful to Dr. Robert Mücke of IEK-1 for allowing me to use the computational resources of his group. Dr. Tobias Arlt, Dr. Henning Markötter, and Dr. Nikolaj Kardjilov helped me a lot during my experiments at Helmholtz-Zentrum Berlin. I am grateful to them.

I thank Abhinav Hazarika, Nagadatta Madhu and Simson Rodrigues for being supportive and enthusiastic colleagues. I am also grateful to other colleagues at my institute.

I am immensely grateful to Ilya, Felix, Jan, Alejandro, Mirjam and Inês for being part of my extended family. They have made my life in Germany much more warm and enjoyable. This journey would not have been complete without the support of my good friends Atul, Nikhil, Ravi, Nabha and Piyush. I will always be thankful to them.

Finally, I would like to thank my family. My mother, who has supported me all the time, I am grateful to her. Thanks to my wonderful sister with whom I can discuss all my issues. Thanks to my nephews, whose smiling faces always brighten my days. For all these long years of understanding, love and support, I am grateful to Simi, my wife. I cannot thank her enough for her patience.

I must not forget all the beautiful music— from peruvian to nordic folk, from ancient Sanskrit chants to modern day EDM, from classic Jazz to 80's Rock — that provided comfort whenever I needed. Thanks to those bands, singers and creators.

Contents

Chapter 1

Introduction

There is a global consensus for fighting against climate change, and many countries have agreed to obey carbon constraints over the years. To reduce fossil fuel consumption and minimize adverse environmental effects, people have looked for alternative energy sources [1–3]. The knowledge of wind and solar energy has existed for quite some time, but making it entirely viable for all practical purposes still requires much research. The significant drawback of the energy obtained directly from renewable sources is its intermittent nature. The available energy changes according to different hours of the day, days of the month or season, and weather conditions. All practical devices require a steady supply of current and voltage to perform properly. Thus, renewable sources' energy needs proper storage and conditioning before they can be put to use. There are two dominant methods at present to store this energy: battery and electrolysis. Batteries store the energy through electrochemical conversion. On the other hand, electrolysis produces hydrogen by splitting water. That can be stored in tanks for future use as a fuel in fuel cells or other industrial processes. Each of these methods has its advantages and disadvantages. However, this literature will deal only with one particular electrolysis method, namely Polymer Electrolyte Membrane or PEM electrolysis.

The use of hydrogen as a component in producing synthetic gas from coal, wood, or waste gasification can be considered the earliest hydrogen usage as a fuel. In the 1950s and 60s, hydrogen was produced from the off-peak power of nuclear reactors, which eventually led to the concept of the hydrogen economy. This idea was further extended in the context of energy from renewable sources [4]. Hydrogen economy means an entire system that, apart from supplementing existing energy infrastructure, can also function as a stand-alone unit capable of meeting any industrial or individual demands. Different aspects of production, storage, and effective utilization of hydrogen have been discussed by researchers [5–8]. The prospect of hydrogen production from solar cells for the year 2000 was analyzed by

Ogden in the year 1991 [9]. The same author also described a future hydrogen economy consisting of large scale hydrogen infrastructure including systems of production, storage, and distribution for all types of industrial and individual requirements [1, 4, 10]. Goltsov and Veziroglu have not only discussed about hydrogen economy, but also about a multi-step transition towards a hydrogen civilization [11–13]. A European Union-wide long term commitment towards a hydrogen economy has been discussed by Adamson [14].

There are mainly three methods of electrolysis of hydrogen, namely

- Alkaline water electrolysis
- Solid oxide electrolysis
- Polymer electrolyte membrane (PEM) water electrolysis

One of the oldest, most mature, and widely employed techniques for producing hydrogen is alkaline water electrolysis [15]. It was discovered by Troostwicjk and Diemann in 1789 [16]. An alkaline electrolyser system contains a 20–30 % KOH solution separated by a diaphragm. The diaphragm allows selective permeation of the hydroxide ion but blocks the passage of the product gases. Although widely used in practice, they suffer from drawbacks like low partial load range, limited current density, and low operating pressure [17].

Although solid oxide electrolysis cells have prior history, the first literature on this topic was published by Dönitz and Erdle in the 1980s [18]. Unlike alkaline electrolyser, a solid oxide electrolysis cell (SOEC) uses a solid oxide or a ceramic electrolyte to produce hydrogen and oxygen. SOECs are capable of operating with high efficiency. Their high operating temperature allows them to be used for the electrolysis of to CO, and co-electrolysis of to . The durability of the ceramic material under high-temperature conditions and long-term operation needs to be ensured before this technology can be adopted for mass production of hydrogen [17].

A major technological breakthrough happened in the 1960s when researchers at General Electric produced the first electrolyser based on solid polymer electrolyte [19]. This electrolysis method is also termed as proton exchange membrane (PEM) or solid polymer electrolyte (SPE) electrolysis. The cell is called PEM water electrolysis cell (PEMEC). Apart from a compact design, proton exchange membrane electrolysis offers advantages like smaller membrane thickness (20–300 m), high proton conductivity, low gas crossover, and high-pressure operation. It is capable of higher current density operation, works smoothly under a wide range of inputs and provides a fast response. However, the high-pressure operation also implies increased cross permeability through the membrane, requiring thicker materials that result in performance degradation. The major drawback of PEM electrolysers originates from the corrosive acidic working environment. This necessitates noble catalysts like Pt, Ir and Ru, and titanium-based porous transport layers and separator plates. The usage of such materials leads to higher expenses. A detailed analysis of PEM electrolyser systems can be found here [17].

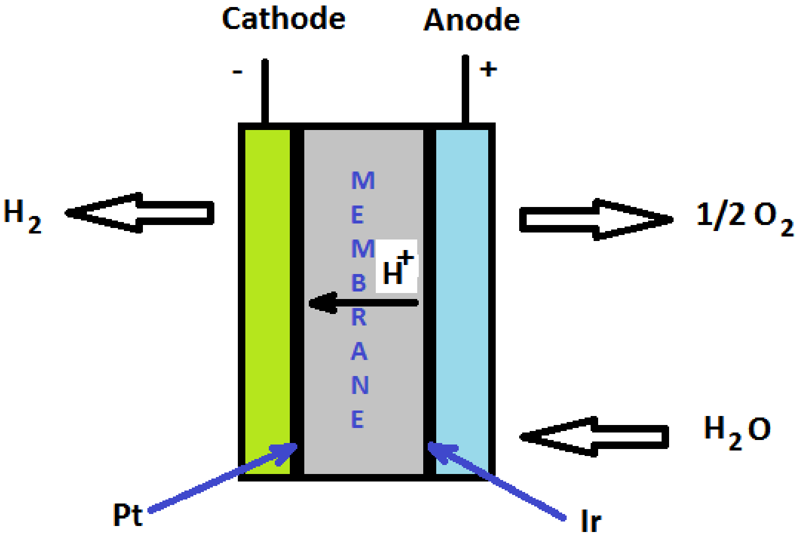

Figure 1.1: PEM electrolyser schematic diagram

A typical PEM electrolyser consists of polymer electrolyte membrane (usually Nafion®), porous transport layers (PTL), bipolar plates, and a catalyst layers attached to the membrane or the porous transport layers. Figure 1.1 shows the schematic of a PEM electrolyser. Generally, the porous transport layer on the anode side is prepared from sintered titanium or expanded mesh that can withstand the corrosive environment. On the cathode side, carbon materials can be used. Water is fed into the anode side that gets distributed through flow field present in the bipolar plate. The water then goes through the porous transport layer to reach the catalyst coated membrane where oxygen and protons evolve. The protons move through the membrane to the cathode side and gets reduced to hydrogen. For smooth and continuous production of hydrogen, the membrane must always be hydrated. That means any product gas that evolves needs to be removed as quickly as possible. This is where the porous transport layer, also known as the current collector, plays an important role. It facilitates electrical contact between the bipolar plate and the membrane and allows gas-water transport. To have lower electrical resistance, it should have a dense solid matrix, but it should have higher porosity for better mass transport. On the other hand, both gas and water flow in directions opposite each other inside the PTL. Thus, the PTL structure has a significant influence on the performance of the electrolysis cell.

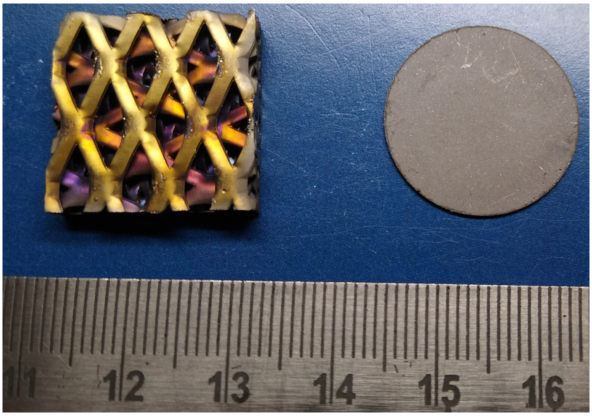

Figure 1.2: Porous transport layers made from expanded metal mesh (left) and sintered titanium powder (right). The ruler divisions are in mm.

The PTL of an electrolysis system consists of sintered titanium powder (Figure 1.2, right), titanium felt, or an expanded mesh (Figure 1.2, left) made from titanium or stainless steel. Ohmic resistance and porosity of the PTL impact the electrolyser cell performance. However, these two terms are insufficient to characterise the PTL completely. Even for the same porosity, the actual mass transport can depend on many factors. The pore size distribution, their connectivity, and wettability of the material influence the two-phase flow significantly. Thus, understanding mass transport inside the PTL is one of the prerequisites for PEM electrolyser performance improvement.

1.1 Aim of this Work

In the context of PEM electrolysis, the PTLs have not been studied by many researchers. In the field of fuel cells, the experimental measurement of relative permeability is reported by different authors. Sole measured relative permeability of PEM fuel cell gas diffusion media using a novel cell design [20]. Relative permeability measurement in both in-plane and through-plane direction of PEMFC gas diffusion media has been reported by Hussaini and Wang [21, 22]. Gostick et al. measured in-plane and through-plane permeability of carbon based gas diffusion media and reported that materials with highly aligned fibres display greater anisotropy [23]. In-plane permeability measurement using a radial flow device has been performed by Feser et al [24]. On the other hand, Dwenger [25] has characterised gas diffusion media with mixed wettability characteristics via experiment and simulation. Some researchers have attempted to model the PTL behaviour with pore network model as well [26, 27]. There exist different tools for simulating mass transport inside such porous layers. Such simulations must be comparable not only among themselves but also validated against experiments. Thus, this thesis attempts to achieve this, particularly in the context of thin porous transport layers of PEM electrolysers. We study the two-phase flow inside the PTL with a particular interest in the material's structural properties. A better understanding of the two-phase flow is essential for future improvements in the design of the PTLs in particular and performance optimisation of electrolysers in general. The objectives of this dissertation are as follows:

- To design a test setup to measure absolute and relative permeability of PTLs
- To study the effect of material structure on mass transport using artificially constructed pore networks. Artificial networks allow manipulation of parameters with reasonable control.
- To obtain -CT images of the PTLs and perform transport simulations on networks extracted from these materials.
- To obtain the correlation between PTL structure and mass transport characteristics
- To compute transport parameters with other simulation software, namely GeoDict, Lattice Boltzmann Method, and ANSYS Fluent to compare with the experiments.

This work is structured as follows:

- The second chapter will deal with the necessary theoretical background for this thesis.
- The third chapter will review PEM electrolyser modelling and simulation. This chapter will also discuss prior work related to absolute and relative permeability measurement of thin porous transport layers of PEM fuel cells and electrolysers.
- The fourth chapter will describe different preprocessing steps and the workflow of pore network modelling, ANSYS Fluent, and GeoDict. Experimental techniques for porous media characterisation will also be discussed.

- The fifth chapter will contain the results of experimental characterisation. Here in-plane, and through-plane permeability and relative permeability measurements will be presented.
- In the sixth chapter simulations carried out will be presented. I will compare results from pore network model, voxel-based calculation in GeoDict, Lattice Boltzmann simulations in Palabos and direct numerical simulations in ANSYS Fluent. Impact of structural properties on the transport behaviour will be studied, and the simulation results will be compared with experimental results.
- In the seventh chapter results from both simulations and experiments will be discussed.
- The final chapter will highlight key findings and suggest possibilities for future work.

Chapter 2

Fundamentals

This chapter will deal with the fundamental principles necessary for carrying out the tasks intended within this thesis. To understand mass transport inside the PEM electrolyser, it is essential to study the components of the system and to understand their working principles. An understanding of flow inside porous media is also a necessary prerequisite. Thus this chapter will discuss the following topics

- An overview of the PEM electrolyser system
- An overview of two-phase flow in porous media
- Overview of multiphase flow modelling
- Numerical methods for flow problems

2.1 PEM Electrolyser System

A PEM electrolyser uses electrical energy to split water to produce hydrogen and oxygen as products. There are five main parts in a PEM electrolyser cell (Figure 2.1)

- membrane
- ionomer
- catalyst layer (CL)
- porous transport layers or current collectors
- separator or bipolar plates

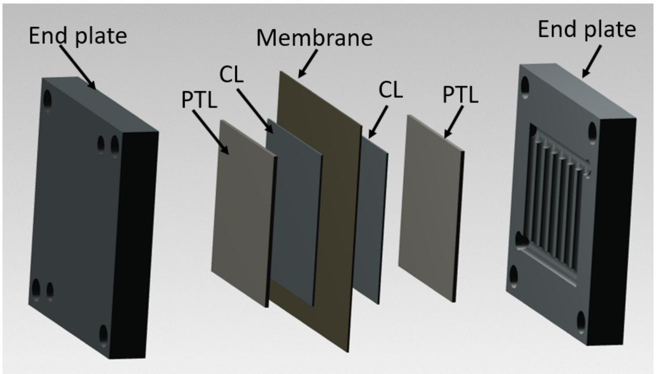

Figure 2.1: A PEM electrolyser cell and its components

2.1.1 Components and Operation

The membrane is the central part of the cell. It allows conduction of only protons from the anode to the cathode side. The catalyst layer is formed by catalyst particles and carbon or conducting oxides. The ionomer is a conducting polymer solution that extends from the membrane to the catalyst layer such that the protons can reach the reaction zone. The catalytic material lowers the activation energy required for the reaction at low temperature. The PTL or current collector consists of highly porous material with high electric conductivity. The function of the PTL is multipurpose; it must provide good conductivity and maintain high porosity for reactant and product transport. The transport process has two counteracting phenomena; while the water should quickly reach the catalyst layer, the product gas bubbles need to be removed simultaneously. The bipolar plates provide structural support, paths for reactant and product transfer, and electric connection.

For membrane, typically a thin sheet of perflourosulfonate polymer (PFS) is used [15, 19, 28, 29]. Nafion® is such an offering formerly produced by Dupont®, now by the company Chemours. The membrane is expected to have high ionic conductivity, and stay stable under high operating temperature and pressure. Overall operation efficiency is improved if the membrane has low ohmic losses. Presently Nafion® is a good membrane material that provides high proton conductivity, mechanical strength, thermal and chemical stability [15, 28]. The presence of fluorine in the material makes the disposal of such polymer membranes problematic [29]. Also, their cost of production is high. On the other hand, temperatures beyond 100 °C causes dehydration resulting in lower ionic conductivity [30]. Cheaper alternatives such as suphonated polytheretherketone or SPEEK have been developed; however, they have not been able to surpass the performance of Nafion® [28].

In a typical cell, the catalyst layers are coated onto the membrane, creating a catalyst coated membrane or CCM. In some cases, the catalyst is coated on the porous transport layer or gas diffusion layer, making a CCG [31]. In the CCM configuration, the ionomer, a polymer solution with ionic transport properties (e.g. Nafion ionomer), connects the catalyst and the polymer membrane. This results in decreased ohmic losses and enhanced proton conductivity to the membrane from the bulk of the catalyst layer. It also acts as a binder for the catalyst layer providing stability and structural support [17]. Thus, in this part of the electrolyser the polymer binder provides proton conduction paths, the catalyst material allows for electron conduction paths, and the pore structure provides for reactant transport paths. However, the polymer opposes electron conduction and makes the catalyst more hydrophilic. This can cause mass transport issues [17]. Thus, a balance is required.

The primary reaction occurs at the triple-phase boundary, where the ionomer, catalyst layer and the reactants meet. The catalyst layer consists of catalytic material, ionomer and supporting material. Pt, Rh and Ir are commonly used as catalyst, while , and are typical examples of supporting material [17]. These materials are rare and expensive, and their usage optimisation has been one of the primary research interests [19, 32]. Two reactions occur in the catalyst layer, namely the oxygen evolution reaction (OER) at the anode and the hydrogen evolution reaction (HER) at the cathode represented by equations 2.1 and 2.2 [33].

$$\mathrm{H\ O} \qquad -\mathrm{O} \qquad \mathrm{H} \qquad \mathrm{e} \qquad \mathrm{E_{oxidation}} \qquad\qquad \mathrm{V} \tag{2.1}$$

$$\mathrm{H} \qquad \mathrm{e} \qquad \mathrm{H} \qquad \mathrm{E_{reduction}} \qquad\quad \mathrm{V} \tag{2.2}$$

Platinum group of materials are considered suitable as the catalyst for PEM electrolysis due to their sufficient activity and stability in the corrosive acidic environment. To optimise such materials' usage, the strategy is to use very fine particle of the catalyst to achieve a higher surface to weight ratio. While platinum nano-particles supported on carbon are used on the cathode side, is considered as the state-of-the-art catalyst on the anode side [17].

During operation, water is usually fed to the anode side of the cell. The water spreads through the flow channels of the separator plate and enters the PTL. Then it diffuses to the reaction sites of the catalyst layer. Simultaneously the evolved oxygen flows against the water flow towards the flow channels and finally leaves the cell through the exit. The protons move through the membrane towards the cathode side. The electrons complete a path through the external circuit to reduce the protons to hydrogen on the cathode side. Thus, for optimal performance of a cell, the PTL needs to have lower ohmic losses to allow higher electron conductivity while possessing higher porosity to allow better mass transport. Additionally, the PTL should be able to withstand the highly corrosive environment and provide mechanical support. High porosity can improve mass transport but reduces electronic conduction. Low porosity improves electronic conduction but hinders mass transport due to the entrapment of gas bubbles. Therefore, the PTL needs optimization based on pore structure, pore size distribution, electron conductivity, and corrosion resistance. Due to the corrosive environment, carbon materials cannot be used on the anode side. Hence, the most commonly chosen material for PTL is titanium. Usually, thin layers made from sintered titanium powders are used for this purpose. Other alternatives include titanium felt, or expanded meshes made of stainless steel or titanium.

The separator plates provide structural support, electronic and thermal conduction and contain the flow field structure for efficient media distribution. According to research, up to 48 % of total stack costs come together from separator plates and catalyst layers [17]. Apart from providing structural support, the separator plate should have lower ohmic resistance, higher thermal conductivity and stability under highly corrosive environment. Titanium is the preferred choice here as well. Gold or platinum-coated stainless steel is another alternative. To improve performance and to prevent the formation of passivation layer, gold coating can be applied [34]. However, it should be noted that any process involving materials like gold or platinum can increase the cost.

2.1.2 Electrolysis Cell Thermodynamics

The following equation can express the electrochemical splitting of water inside a PEM electrolysis cell:

$$\underbrace{\qquad\qquad}_{\text{electrical energy}} \quad \underbrace{\qquad\qquad}_{\text{heat}} \qquad\qquad - \qquad\qquad\qquad \text{kJ/mol} \tag{2.3}$$

where is the enthalpy of the cell reaction under standard conditions. The effective electrical energy for the reaction is

$$\tag{2.4}$$

where is the free energy, is the entropy, and is the temperature. For liquid water, under standard conditions, the values of and are and , respectively. Thus, if only the energy required for the electrochemical conversion is considered, according to Nernst equation, the reversible cell potential becomes

$$\frac{}{}\qquad\frac{}{} \tag{2.5}$$

where is the number of moles of electrons transferred, and is Faraday's constant. In practice, some energy is utilized as heat in the reaction. Therefore to sustain the cell reaction energy equivalent to the enthalpy of formation needs to be supplied. This defines the thermoneutral voltage of the cell which can be calculated as

$$\frac{}{}\qquad\frac{}{} \tag{2.6}$$

The above value of the reversible cell potential is valid only under standard conditions. In reality, it is a function of temperature and pressure, and it is calculated from the following equation

$$\frac{}{}\left(\frac{{}_{2}\sqrt{}\quad{}_{2}}{{}_{2}}\right) \tag{2.7}$$

where is universal gas constant, and with given subscripts represent activities of the respective species. When the activities are replaced with the partial pressure at standard temperature normalized to the operating pressure ( ), the reversible potential becomes [35]

$$\frac{}{}\left(\frac{{}_{2}\quad\sqrt{}\quad{}_{2}}{{}_{2}}\right) \tag{2.8}$$

There are some relationships for finding which are discussed in Section 3.1.1.

The activation overpotentials can be found from Butler-Volmer Kinetics. Combining the forward and backward reaction at an electrode, one can write

$$\left[\left(\frac{}{}\quad\right)\quad\left(\frac{}{}\quad\right)\right] \tag{2.9}$$

In the above equation is the current density, and is the exchange current density. The term represents the symmetry factor, is the number of electrons transferred, and is the activation overpotential. When is assumed to be , the above equation yields

$$\frac{}{}\qquad\left(\frac{}{}\right) \tag{2.10}$$

$$\frac{}{}\qquad\left(\frac{}{}\right) \tag{2.11}$$

The subscripts and refer to the anode and the cathode respectively.

There is certain resistance in a cell due to the electrical components, and the corresponding overvoltage (defined here as) would increase in direct proportion to the current density. Similarly, overvoltage due to resistance to proton transport ( ) will increase as a function of current density. Ohmic overvoltage ( ) is the sum of overvoltage due the membrane and electrical components, i.e.

(2.12)

When the cell current density is high, the rate of production of gas increases. Therefore quick removal of products and faster supply of reactants to the reaction sites becomes important. The porous medium's structural limitations would result in an overpotential known as diffusion or mass transfer overpotential (, discussed in Section 3.1.2). Thus, combining all the overpotentials described above the cell potential can be expressed as

(2.13)

The sum of Nernst voltage and these losses results in the actual cell voltage. In the above equation contains the sum of activation overvoltage for both the electrodes. In Figure 2.2, this is shown as a function of current density of the electrolysis cell. With the increase in current density, the mass transfer effects become more noticeable. According to Suermann et al. [36] mass transfer effects can contribute between 20-25 % of the total overpotential.

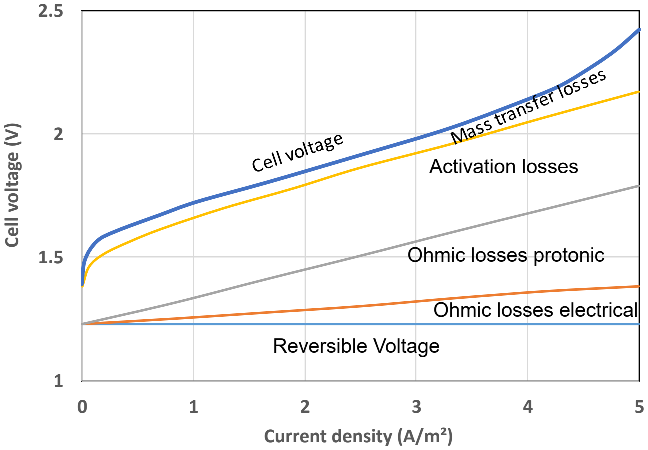

Figure 2.2: A representative figure for cell voltage as a contribution of different overpotentials

2.2 Flow in Porous Media

Flow inside a porous media can be discussed from two different perspectives. In the first approach, one can consider the whole porous media as a single unit and approximate properties of interest for the whole unit. The other approach is to consider the pore structure's individual parts like pores and throats in their geometric detail or approximate representation of the same. Depending on the requirement, one can choose the method and find out the porous media properties of interest for a particular purpose. The following sections would address different concepts essential for the understanding of flow inside porous media.

2.2.1 Flow without Inertial Effects: Darcy's Law

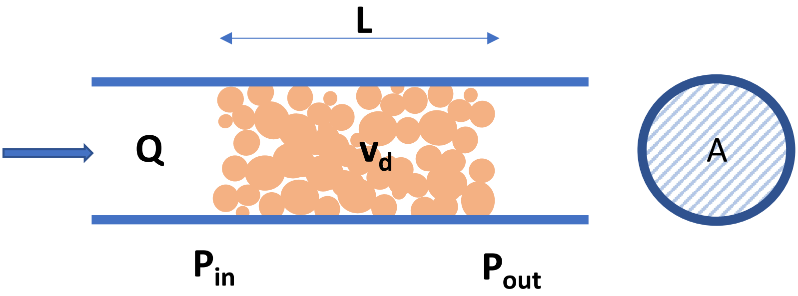

Figure 2.3: A representation of flow through porous media

Darcy's law is attributed to the French scientist Henry Darcy. He carried out a series of steady-state unidirectional flow experiments on sand columns and based on the observations proposed an empirical relation [37, 38]. For unidirectional flow, the flux can be related to the piezometric head as given by the following equation

— (2.14)

In the above equation, is the flux, is the hydraulic conductivity, is the applied pressure, is the density and is the acceleration due to gravity. The flux has the unit of velocity. It is also known as Darcy velocity or superficial velocity as it does not represent the actual flow velocity inside the pore space. This velocity is also denoted by . Based on the total volume flow rate ( ) and the cross-sectional area ( ) of the porous medium as depicted in Figure 2.3, it is possible to write

(2.15)

When gravitational effects are ignored, the three-dimensional extension of Darcy's law takes the following form

$$\overline{\overline{}} \quad \frac{\ }{\ } \tag{2.16}$$

where $\overline{\overline{}}$ is the permeability tensor, and is the dynamic viscosity. The components of the permeability tensor are given by

$$= \begin{bmatrix} & & \\ & & \\ & & \end{bmatrix} \tag{2.17}$$

For the situation in Fig. 2.3, the permeability of the medium in its simplest form can be calculated from

$$\frac{\ }{\ } \quad \frac{\ }{\ } \quad \frac{\ }{\ } \quad \frac{\ }{\ } \tag{2.18}$$

where is the length, is the pressure at the inlet, and is the pressure at the outlet. In SI units the unit of permeability is . But most of the practical problems require units much smaller than this. People commonly use another unit called "Dacry unit". The following conversion formula defines it

$$\text{Darcy} \tag{2.19}$$

It should be noted that Darcy's law is valid only for slow laminar flow. It is not applicable for faster flow where inertial effects dominate. Different authors have discussed the applicability of Darcy's law for different materials and flow conditions. According to literature, Darcy's flow is valid for Reynold's number in the range of values from less than 1 to 10 [39, 40].

2.2.2 Flow with Inertial Effects: Forchheimer Flow

When Reynold's number increases, the inertial effects start to dominate the flow. As a result, the pressure drop no longer has a linear relationship with the flow rate. Such a flow is termed as non-Darcy flow [41, 42]. Based on his work on high-velocity flow through porous media, modification to the Darcy's equation was suggested by the scientist Phillip Forchheimer [43, 44]. This modification includes a second order velocity term to the pressure gradient. As a result, the modified equation in the vector form can be written as [44, 45]:

$$\frac{\ }{\ } \tag{2.20}$$

where is Forchheimer's coefficient, and is Forchheimer's velocity calculated in the same manner as Darcy velocity. It is possible to find out the Forccheimer's coefficient analytically [46]; but it is, in general, a tedious process. Based on experimental data, the coefficient can be determined using curve-fitting techniques [39, 40, 47]. Based upon experiments on flow through packed columns and fluidized beds, Ergun et al. [48, 49] suggested an empirical relation as:

$$\frac{}{\sqrt{}} \tag{2.21}$$

where is known as Ergun's coefficient. The value of this coefficient depends on the flow regime. For slower flow, the value of this coefficient becomes negligible. Under this situation, one can recover the original Darcy's equation from Frochheimer's equation.

2.2.3 Flow through Pipe: Hagen-Poiseuille Equation

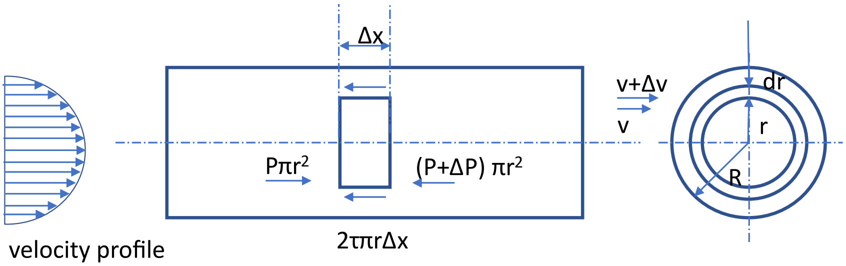

Figure 2.4: Derivation of Hagen-Poiseuille equation by considering force balance on a cylindrical fluid element

Hagen-Poiseuille equation describes flow through a pipe when certain assumptions are valid. This equation plays a vital role in solving fluid flow problems in practical applications ranging from the size of conventional pipes to the scale of microscale porous media. This equation can also be derived as a special case of the Navier-Stokes equations. This equation or law is applicable when the following assumptions are valid:

- The fluid is incompressible
- The flow is laminar
- The cross-section is uniform, and the length is much larger as compared to the cross-section
- The fluid is Newtonian, i.e. viscous stress due to the flow is directly proportional to the strain rate.

- There is no relative motion between fluid particles and solids at the fluid-solid boundary, i.e., no-slip boundary condition.

The ideal case of a flow through a pipe can be depicted with the help of Figure 2.4. One can consider a cylindrical element of length with radius . The outer diameter of the pipe is . The fluid is flowing from the left to the right. For a Newtonian fluid, the shear stress is given by:

$$\frac{}{} \tag{2.22}$$

This means that the velocity of concentric layers of fluid would change with respect to its distance from the pipe's centre. A force balance can be applied to the fluid element, which yields:

$$\tag{2.23}$$

When is considered to be infinitesimally small, the following relation can be obtained:

$$\frac{}{} \quad \frac{}{} \tag{2.24}$$

Now the expression for the shear stress in Equation 2.22 is substituted in Equation 2.24 resulting in the following equation :

$$\frac{}{} \quad \frac{}{} \quad \frac{}{} \tag{2.25}$$

It is important to note that the pressure gradient term is independent of . Therefore, the above equation can be integrated to obtain the velocity . This integration, when subjected to the no-slip boundary condition, i.e. at the boundary, would finally yield the complete expression for the velocity of the fluid as follows:

$$\frac{(\qquad)}{} \quad \frac{}{} \tag{2.26}$$

This equation represents a parabolic velocity profile, as shown on the left side of Figure 2.4. Now, considering a small cylindrical element of thickness as shown in the right side of the figure, the total volume of fluid flowing through the pipe can be calculated by integrating velocity over the cross-section of the pipe. This produces the Hagen-Poiseuille equation in its most common form:

$$\int \qquad \frac{}{} \left(\frac{}{}\right) \tag{2.27}$$

The above equation gives the rate of volume flow. For a pressure drop of over a length of a pipe, the flow rate can be written in a simpler form as:

$$\frac{\quad}{\quad} \quad \frac{\quad}{\quad} \tag{2.28}$$

From Darcy's law, one can write the same as:

$$\frac{\quad}{\quad} \quad \frac{\quad}{\quad} \tag{2.29}$$

A comparison of the above two equations reveals that the pipe's absolute permeability is only a function of its geometry and independent of the fluid. This observation is significant, as it can be extended to any general porous media. Thus, one concludes that a given porous medium's absolute permeability is independent of the fluid flowing through the medium. Now, Equation 2.28 can be rearranged as follows:

$$\frac{\quad}{\quad} \left(\quad \frac{\quad}{\quad} \right) \tag{2.30}$$

The first term on the right-hand side of the above equation is the pipe's hydraulic conductivity. This Hagen-Poiseuille equation for a single pipe can be extended to a bundle of tubes or a randomly connected set of tubes in a porous media. With suitable approximation techniques, it is possible to compute the hydraulic conductivity of the entire porous material.

2.2.4 Capillary Flow

Typically a porous material consists of numerous capillaries. Capillary behaviour has a significant impact on the flow inside such a material. Flow inside the microscopic capillaries of the PTLs depends on the surface tension and the wettability of the liquid on the material. Wettability, in turn, is characterized by the contact angle between the solid-fluid system. A brief description of capillary flow and related topics are discussed in this section. These topics are discussed mainly based on the literature by F.A.L. Dullien [50]. For a more detailed treatment of the topics, the reader should refer to the original text.

2.2.4.1 Surface Tension

Surface tension is a property of a liquid through which it tries to minimize the surface area. For example, in case of an interface between liquid and gaseous phases, this behaviour is an outcome of the difference of cohesive force between the liquid molecules and the adhesive force between the liquid and gas molecules on the surface. A molecule at the liquid's interior experiences zero net force due to the balance of forces from all directions. However, for molecules on the surface, the cohesive forces are not balanced by the adhesive forces, resulting in an unbalanced pull towards the liquid's interior. Because of this, the liquid tends to behave like a stretched membrane. Thus, when a given liquid's surface area needs to be expanded by amount , some amount of work needs to be performed. From this relationship, the surface tension can be defined as

$$\frac{\;}{\;} \tag{2.31}$$

When a liquid is inside a container, the difference between adhesive and cohesive forces will define the wettability, contact angle, and the shape of the meniscus. Stronger cohesive force between the liquid molecules results in lesser wetting of a container's vertical walls that produce a convex meniscus as is seen in the case of mercury in a glass container. On the other hand, when water is in a glass container, the stronger adhesive forces between water and air results in a concave meniscus.

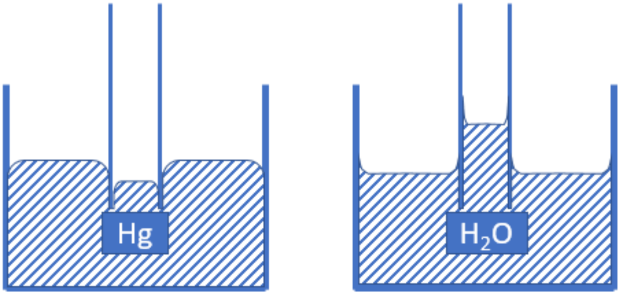

Figure 2.5: Surface tension and capillary action shown with the example of a glass capillary inside mercury and water. Mercury does not wet glass surface and forms a convex meniscus. Water wets the glass surface and gets pulled up by the adhesive forces

2.2.4.2 Contact Angle and Wettability

Different cases of flow inside porous media involve one solid, and two or more fluid phases. As shown in Figure 2.6, a three-phase system consisting of a droplet on a smooth solid surface can be considered. With reference to the figure, the contact angle is defined as the angle between the tangent at the liquid-gas interface and the tangent at the solid-liquid

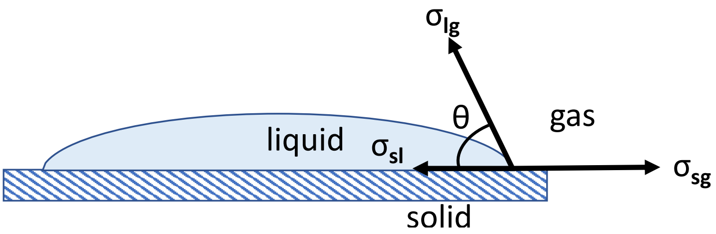

Figure 2.6: Equilibrium of surface tension forces, (adaptation from [50, P. 123])

interface. The surface tension forces would balance each other at any point along the contact line, as shown in the figure. For such an equilibrium the following relation would hold

(2.32)

The above equation is also known as Young's equation. How the liquid would spread on the solid's surface depends on the value of the contact angle. The value of can vary between ° and °. In the interval ° ° the liquid is known as wetting, i.e. it tends to spread on the solid surface. In the interval ° ° the liquid is considered as not-wetting. When the value of contact angle approaches zero, the tendency to spread on the surface increases. For a higher value of contact angle beyond °, it is more difficult for the liquid to spread on the surface. Then it would tend to have a more spherical shape. For values of closer to ° the liquid shows intermediate wettability. The terms wetting phase and non-wetting phase are used while describing multiphase systems. However, these two terms are relative and depend on the system under consideration. For example, for the gas-water flow inside a titanium PTL, water would be the wetting-phase and oxygen would be the non-wetting phase. On the other hand, for oil and gas trapped inside porous rocks, oil would be considered as the wetting phase and gas as the non-wetting phase. But for a system of oil and water inside porous rocks, water would be the wetting phase, and oil would be the non-wetting phase.

2.2.4.3 Young-Laplace Equation

The Young-Laplace equation describes the capillary pressure difference across the interface of two static fluids. It depends on the shape of the interface. As shown in Figure 2.7, one can consider a non-spherical cap on which, from a point , a circle of constant small radius is drawn. If two arbitrary orthogonal lines and with radii of curvature and are considered, then for the principal radii of curvature and , the following relationship holds

— — — — (2.33)

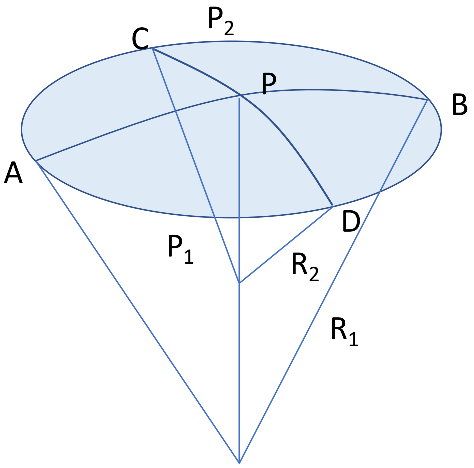

Figure 2.7: Equilibrium of forces on a non-spherical cap (adaptation from [50, P. 120])

In the given system, and are pressures on the concave and convex sides of the interface respectively. Considering surface tension , pressure difference is mathematically expressed as

$$\left[\frac{}{}\quad\frac{}{}\right] \tag{2.34}$$

If mean radius is defined, then the above equation can be written as

$$\frac{}{} \tag{2.35}$$

For a cap with a spherical shape, the mean radius would be the same as the radius of curvature, i.e. .

2.2.4.4 Capillary Pressure

Capillary pressure is an important parameter when the flow of two or more immiscible fluid phases inside porous media is concerned. To understand this, a conical capillary representing the porous media as shown in Figure 2.8 is considered. The capillary extends an angle at the point of convergence and is the angle made by the tangent to the interface with the solid surface. It is assumed that the capillary is initially filled with the wetting fluid (fluid 1), and the pressure is atmospheric. The non-wetting fluid (fluid 2) is also at equilibrium, and no flow is happening. If now the non-wetting fluid is pushed into the capillary to displace the wetting fluid, then the required pressure for the flow to occur would be given by:

$$\frac{}{} \tag{2.36}$$

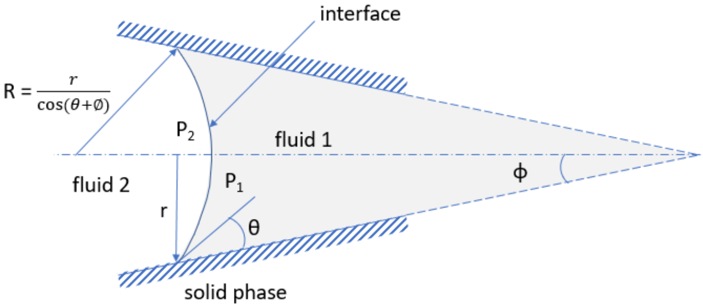

Figure 2.8: Capillary pressure in a conical capillary (adapted from [50, P. 129])

The term is the capillary pressure, and it is a positive quantity. This expression follows from the Young-Laplace equation and depends on the geometry of the capillary. When a tubular capillary is considered, the equation reduces to Washburn equation [51], which is given by:

$$\frac{}{} \tag{2.37}$$

It is important to note that the terms wetting and non-wetting are not absolute and can be used only with respect to the behaviour of two or more fluids in a given porous medium. The displacement of a wetting fluid by a non-wetting fluid is called drainage, and the opposite process is called imbibition. In the current work, the capillary pressure given by Equation 2.37 is used to find out the pressure needed for displacing a wetting fluid by a non-wetting fluid from a capillary tube.

2.2.5 Molecular Diffusion

The broad definition of diffusion is the movement of something from a region of higher concentration to a region of lower concentration. Molecular diffusion is the process of thermal motion of gas or liquid molecules in the presence of a concentration gradient. There is a net flux from the region of higher concentration to the region of lower concentration. Once the equilibrium concentration is reached, the molecules still continue their thermal motion, but the overall concentration remains unchanged. The process of diffusion can be described by two laws, also known as Fick's laws of diffusion as attributed to the scientist Adolf Fick [52]. The two laws of diffusion are:

- The diffusive molar flux is proportional to the concentration gradient, i.e.

  (2.38)

  where is the diffusive flux (mass per unit volume per unit time) for component , is the coefficient of diffusion and is the concentration.

- At any given point in space, the rate of change of concentration is proportional to the second derivative of the concentration in space, i.e.

  —— (2.39)

2.2.6 Relative Permeability

In Section 2.2.1, Darcy's law was discussed, and absolute or intrinsic permeability was defined. Absolute permeability is a material property and independent of the fluid flowing through the medium. But in practical systems like PEM electrolysers, there exists more than one phase in the porous medium. Such multi-phase systems are part of a large number of industrial and naturally occurring phenomena.

When more than one phase exists in the same porous matrix, they interact and influence the flow through the medium. Under such situations, the concept of relative permeability becomes essential. This means the permeability of one phase in the presence of another phase. For a multi-phase system Darcy law can be modified as follows:

———— (2.40)

where the subscript represents a given phase. The term is the relative permeability of the phase . The product of relative permeability and the intrinsic permeability gives the effective permeability of the phase . Relative permeability is a dimensionless number that lies between 0 and 1. In the presence of another phase, the available number of flow paths for a given phase decreases. Hence, effective permeability would always be smaller than or equal to the absolute permeability. It should be noted that relative permeability is not a single number. Depending on how much of the pore space is occupied by the second phase, the first phase's effective permeability would change. Therefore, it is customary to express relative permeability as a function of saturation of the wetting phase.

2.3 Continuum Description of Fluid Flow

A large number of natural and industrial processes involve fluid flow. Such processes can be described mathematically with the help of a set of equations. These equations are based on the principles of mass, momentum and energy conservation. One given physical quantity is considered the dependent variable in each equation, and a balance among the different entities influencing that variable must exist [53]. These are also known as Navier-Stokes equations. Most of the flow solvers (e.g. ANSYS Fluent, STAR CCM+, OpenFOAM, etc.) solve mass and momentum conservation equations for any flow problem. Some situations involve heat transfer or compressible flow. That requires energy conservation equation to be solved. Depending upon the problem under consideration, additional conservation equations, transport equations, or constitutive relations are needed to capture the flow behaviour.

The mass and momentum conservation equations are given by

$$\frac{}{} \tag{2.41}$$

$$\frac{}{} \qquad (\overline{\overline{\;}}) \tag{2.42}$$

The first equation is valid for both compressible and incompressible flow and the terms , and represent the density, the velocity and the mass source respectively. In the second equation for momentum conservation in an inertial reference frame, is the static pressure, $\overline{\overline{\;}}$ is the stress tensor, and is the gravitational body force, and accounts for external body forces.

The stress tensor $\overline{\overline{\;}}$ in the momentum conservation equation is defined as:

$$\overline{\overline{\;}} \qquad \left[\left(\qquad \right) - \qquad \overline{\overline{\;}}\right] \tag{2.43}$$

where is the molecular viscosity, $\overline{\overline{\;}}$ is the unit tensor, and relates to the effect of volume dilation due to fluid motion.

In any multiphase flow system, two or more gas, liquid or solid phases are present simultaneously. Accordingly, multiphase flows can be categorized into gas-liquid or liquid-liquid flow, gas-solid flow, liquid-solid flow and three-phase flow. It is important to note that in multiphase flow, any identifiable class of material having a particular inertial response to and interacting with the flow and the potential field in which it is immersed can be considered as a distinct phase [54]. This thesis will mainly deal with the gas-liquid two-phase flow, which can be further divided into bubbly flow, droplet flow, slug flow and stratified flow depending on how the two phases interact. It should be noted that ANSYS Fluent is the solver used for the work in this thesis, and the descriptions and notations of different terms are kept consistent with Fluent theory guide [54]. The discussion in the next sections would refer to the same unless otherwise mentioned.

2.4 Multiphase Flow modelling

The general Navier-Stokes equations give way for modelling multiphase flow. For a particular problem, depending on the desired accuracy, available computational resources and time, modelling such flow can vary from moderate to very complex. There exist two different approaches to multiphase flow modelling:

- Euler-Lagrange approach
- Euler-Euler approach

The **Euler-Lagrange approach** treats the fluid phase as a single continuum for which the Navier Stokes equations are solved. The dispersed phases, like particles or bubbles, are tracked in the Lagrangian framework. Interaction between the phases can take place through mass, momentum or energy transfer. The details of the equations can be found here [55, 56]. Different source terms can be used for interphase coupling. However, with additional details, such a system can become very complex and computationally demanding. Hence, this approach is well suited for problems where the dispersed phase volume fraction is small.

The **Euler-Euler approach** considers all phases as interpenetrating continua. The volume fraction of each phase is assumed as a continuous function of space and time such that the total volume fraction of all the phases is unity. For each phase, conservation equations are solved. Coupling between the phases is achieved with the help of shared pressure and interphase exchange coefficients which need to be modelled. Inclusion of these models depends on flow type, desired accuracy and computational resources. There are mainly three Euler-Euler category methods: the mixture model, the volume of fluid (VOF) model, and the Eulerian multiphase model. The first two models are briefly described in the next sections.

2.4.1 The Mixture Model

The mixture model is one of the simplest multiphase flow models. It allows relative velocity between phases but assumes that there exists local equilibrium over short spatial scales.

For a mixture of phases, the mixture model solves one set of mass, momentum and energy equations for the whole mixture, volume fraction equations for the secondary phases and algebraic expressions for the relative velocities. This model can be used for homogeneous flows with strong interphase coupling. It is suitable for modelling sedimentation, cyclone separators or bubbly flows where the gas volume fraction is small. The three conservation equations required for the mixture model (represented by the subscript) consisting of phases are given below [55, 57, 58].

The equation for the conservation of mass is

$$ - \tag{2.44}$$

where and represent the mass averaged velocity of the mixture and the mixture density, respectively. For a two-phase system, they can be written as

$$ \overline{\qquad\qquad\qquad} \tag{2.45}$$

$$ \tag{2.46}$$

where is the volume fraction and the subscripts refer to the individual phases.

The momentum conservation equation for the mixture model is:

$$ - \qquad [\quad (\qquad\qquad)] \\ \left(\sum \qquad\qquad \right) \tag{2.47}$$

where represents the number of phases. The terms , , represent the body force, the viscosity of the mixture and the drift velocity for the secondary phase . The mixture viscosity and the drift velocity for the phase are defined as

$$ \sum \tag{2.48}$$

$$ \tag{2.49}$$

For the mixture model the following energy equation is solved:

$$ -\sum \qquad\qquad \sum \tag{2.50}$$

where $\sum$ is the turbulent thermal conductivity that depends on the turbulence model used. The first and the second term on the right-hand side represents the energy transfer due to heat conduction and any volumetric heat source present in the flow. There exist different formulations for the computation of relative velocity and drag forces [54]. Based on those, the system of equations can be solved in the mixture model.

2.4.2 The VOF Model

The volume of fluid or VOF method was first presented by Hirt and Nichols in 1981 [59]. This method assumes that the phases are not interpenetrating. This transient method allows interface tracking between phases. A single set of momentum equations is solved, and the interface is tracked throughout the domain. A phase indicator function or a colour function is used for tracking the interface between the phases. The phase indicator function has properties similar to volume fraction. For the fluid's volume fraction in a cell, it can be interpreted as:

- means no phase exist in the cell
- means the cell is completely filled with the phase
- means an interface exists between the phase and another phase

For a system of phases, in the absence of source term or mass transfer between the phases, the volume fraction of the phase can be computed from

$$- \left[- \right] \tag{2.51}$$

Volume fraction for the primary phase is solved by using the following constraint:

$$\sum \tag{2.52}$$

The momentum and energy equations are written as

$$- \quad [\;(\quad)] \tag{2.53}$$

$$- \tag{2.54}$$

In the momentum equation, the density and the viscosity are defined as the average of the phases, i.e.

$$\begin{gathered}\sum\\ \sum\end{gathered} \tag{2.55}$$

In the energy equation, is the energy of each phase, and represents contributions due to radiation or any other volumetric heat sources. is the thermal conductivity shared by all the phases. The energy and the temperature are treated as mass-averaged variables. For energy it can be formulated as

$$\frac{\sum}{\sum} \tag{2.56}$$

The VOF model is suitable for flows where interface tracking is essential. For the VOF model to be useful, the interface length scale needs to be bigger than the computational grid. There are different methods like Geo-reconstruct, Modified HRIC (High Resolution Interface Capturing) Scheme, Compressive or CICSAM (Compressive Interface Capturing Scheme for Arbitrary Meshes) for interface capturing.

There are two ways to model surface tension in the VOF model, namely continuum surface model (CSF) by Brackbill et al. [60] and continuum surface stress model (CSS) by Gueyffier et al. [61].The CSF model implements a surface tension through a source term in the momentum equation. Surface tension is included as a pressure difference across the interface. This method is non-conservative and requires the explicit calculation of the surface curvature. CSF is valid only for constant surface tension. CSS model conservatively implements surface tension by utilizing a surface stress tensor. It is also suitable for variable surface tension and does not require explicit interface curvature calculation. However, it should be noted that both methods introduce parasitic current at the interface because of pressure gradient and surface tension force imbalance [54, 62].

2.5 Numerical Methods for Fluid Flow

The last section (2.3) discussed the analytical representation of fluid flow problems. Although it is possible to express fluid flow problems with the help of general equations, finding solutions to these non-linear differential equations is possible only for very few practical cases. Due to the involved complexity, it is almost impossible to find the exact analytical solution of most problems. Hence, it becomes necessary to compute an approximate solution to these equations with numerical methods. Application of numerical methods enables conversion of these equations to a set of algebraic equations of the form

Ax=b which can then be solved by applying appropriate boundary and initial conditions. This process is popularly known as computational fluid dynamics or CFD. There exist different techniques to obtain an algebraic system of equations from the analytical equations. Some of these techniques are Finite Difference Method (FDM), Finite Volume Method (FVM), Finite Element Method (FEM), Boundary Element Method (BEM) etc. Lattice Boltzmann Method (LBM) is one non-classical CFD method. Theoretically, it is possible to apply these methods to solve fluid flow problems in any domain. However, there exists practical limitations, advantages and disadvantage with respect to different methods. Apart from the methods already mentioned, one more method is suitable for modelling pore-scale phenomena called pore network model (PNM). Since finite volume method, lattice Boltzmann method and pore network model are relevant for this thesis; they are described in the next sections.

2.5.1 Finite Volume Method

Finite volume method or FVM is one very widely used method for discretizing the transport equations in computational fluid dynamics. Rather than solving the equations at every point of the continuous domain, the idea here is to divide the domain into finite-size volumes so that an approximate solution to the differentials equations can be estimated with reasonable accuracy. In this process, multiple non-overlapping intervals are created by subdividing the computational domain, and each grid points is inside a control volume over which the differential equations are integrated. If is the function of interest, then a piece-wise approximation of the function expressing the variation of its value across the grid points is utilized to evaluate the integrals. The averages of the fluxes are computed over the finite volumes. This process produces the discretized form of the conservation equations. Irrespective of the number of control volumes, the FVM approach ensures that the conservation principles are satisfied over any group of control volumes as well as the whole domain [53, P. 25-40]. To understand this the one dimensional hyperbolic conservation equation can be considered, which is

$$\mathbb{R} \qquad (2.57)$$

$$\mathbb{R} \qquad (2.58)$$

Now, by dividing the real line into finite intervals, we can generate control volumes
$[\qquad\qquad]$ such that each grid point can be defined as

$$\frac{(\qquad\qquad)}{} \qquad (2.59)$$

For one dimensional problem, the volume of the element is given by its length. Thus, it can be written as

$$\int_{-1\ \ 2}^{+1\ \ 2} \tag{2.60}$$

Assuming control volumes of constant length the volume average over the control volume can be introduced as

$$-\int_{-1\ \ 2}^{+1\ \ 2} \tag{2.61}$$

Integration of Equation 2.57 over the interval will produce

$$\int \tag{2.62}$$

This will lead to the next equation given by

$$- \tag{2.63}$$

Now, it is possible to construct a numerical scheme such that

$$\sum \tag{2.64}$$

where,

$$\begin{cases} & \text{if} \\ & \text{otherwise} \end{cases} \tag{2.65}$$

The solution to this problem is discontinuous at the junction of different intervals. Thus, at these points a numerical flux can be defined as . The equation 2.63 can be reconstructed

$$- \tag{2.66}$$

For this problem the initial condition can be expressed as

$$\int_{[}^{[} \tag{2.67}$$

If denote the value of at time step , and be the discrete time step size such that , then applying forward difference scheme for the time derivative leads to a fully discretized form of the equation 2.57 as

$$-\Big(\qquad \Big) \tag{2.68}$$

The above equation enables the transformation of the original conservation equation in the form of an algebraic system of equations which can be solved numerically. The equation 2.68 is similar to finite difference formulation, but the strength of FVM lies in its application to multi-dimensional problems. While it is tedious to extend finite difference formulations to general meshes in multi-dimension, the FVM formulation can be easily extended to multi-dimensional problems with general mesh [63].

2.5.2 Lattice Boltzmann Method

Lattice Boltzmann Method (LBM) constitutes a new paradigm for simulation of physical processes based on the particle or molecular description of fluid rather than the continuum description. Kinetic gas theory with Maxwell-Boltzmann statistics, Boltzmann equation, and Bhatnagar-Gross-Krook (BGK) equation form the primary basis for LBM. The idea of LBM originates from cellular automata. Stanislaw Ulam and John von Neumann first put forward the concept of cellular automata. This concept was first used for fluid flow simulation by Hardy, Pomeau and de Pazzis [64], also known as the HPP model. The FHP model suggested by Frisch et al. [65, 66] successfully provided accurate fluid flow simulation based on lattice gas cellular automata (LGCA).

The LGCA model of the gas consisted of fictitious particles that could have only binary values at a given lattice point. The flow process was simulated through a series of streaming and collision processes over the lattice. A suitable collision rule allowed for the conservation of mass, momentum and energy. However, these models lacked Gallielean invariance and were susceptible to statistical noise. To overcome such problems, the idea of having a probability distribution for the particles density was suggested [67, 68]. This led to the development of the Lattice Boltzmann Method. The introduction of the BGK single time collision operator led to further improvement of the model [69]. There exist different two and three-dimensional lattice configurations in the LBM. In Fig. 2.9, a D3Q19 configuration lattice configuration typically used in 3D flow simulations is shown. The lattice Boltzmann equation represents the time evolution of the density function of the fluid particles. The LB method involves two steps:

- Propagation or streaming step:

(2.69)

- Relaxation step:

(2.70)

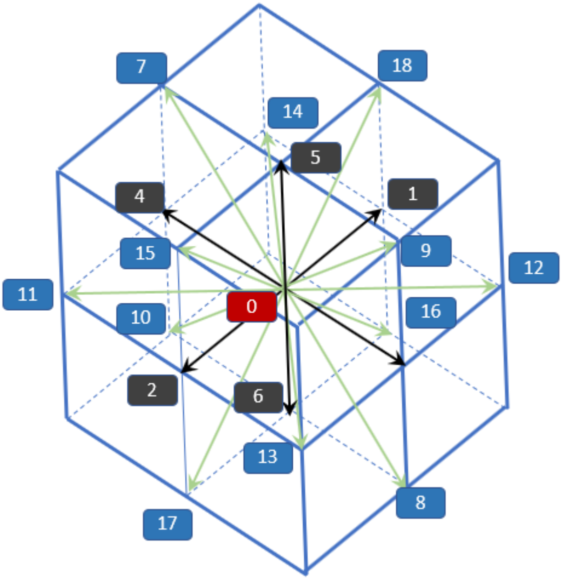

Figure 2.9: D3Q19 Lattice for LBM

In the above equations represents the component of particle density at any point at time , are the velocity vectors along each direction of the lattice and is the relaxation term. Then the equilibrium distribution is given by the following equation [69]

$$\left[\quad \frac{}{} \quad \frac{}{} \left(\frac{}{} \quad \right) \right] \tag{2.71}$$

where is a weighting factor such that at the centre, for the orthogonal directions and for the diagonal directions, resulting in values of , and . The term is the speed of sound that depends on the model. The value of is $\frac{}{}$ for D3Q19 lattice. is the macroscopic velocity, and the components and represent Cartesian components with a summation.

The macroscopic quantities can be derived from the density distribution function in the following manner

$$\sum \quad \sum \tag{2.72}$$

$$\sum \quad \sum \tag{2.73}$$

$$\tag{2.74}$$

$$\left(\frac{}{} \quad \frac{}{} \right) \tag{2.75}$$

where is the fluid density and is the viscosity [70]

2.5.3 Pore Network Model

Pore Network Model offers a different perspective to fluid flow modelling as compared to FVM or LBM. In the pore network-based approach, the porous domain is approximated as a network of interconnected pores and throats. Rules are defined for the transport of different phases in the individual pores and throats, and then the set of equations is solved for the entire set of pores and throats of the whole network. Such a network can be constructed numerically to match experimental observations for a given material; or an equivalent network can be extracted from a 3-dimensional image of the actual material using different image processing and network extraction techniques [71, 72]. In Fig. 2.10, a simplified representative pore network is shown where the pores and throats can have different dimensions or shape properties. Now for a system or spherical pores and cylindrical throats, it is possible to use Hagen-Poisseuille equation (refer Eq. 2.28) for conduction between any two pores and as

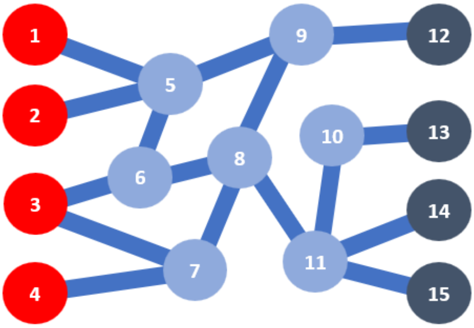

Figure 2.10: A representative pore network

$$\frac{}{} \tag{2.76}$$

It is possible to use this type equation for a general transport process such as electric conductance based on Ohm's law, or heat conductance. Thus, a general form of the equation can be written as [73]

(2.77)

where is the conductance between the pores, and is the unknown variable of interest. The above equation is implemented at the individual pore and throat level. Different techniques can be used to implement the effects of geometry and shape into this model. Now, under steady-state conditions without any source or sink, for each pore with neighbours it can be written as

$$\sum \tag{2.78}$$

This process can be applied to all the pores in the network which will result in a system of equations of the form

$$\mathbf{A}\mathbf{x} \quad \mathbf{b} \tag{2.79}$$

By applying proper boundary conditions, this system of equations can be solved using suitable numerical techniques.

Capillary dominated flow processes, or multi-phase flow processes can also be modelled using suitable techniques. As discussed in Section 2.2.4.4, the entry capillary pressure can be computed for each throat in the network. When a non-wetting fluid is allowed to invade a domain from one side, it will invade the pores and throats connected to the reservoir for which the capillary pressure is higher than the entry capillary pressure. For each incremental pressure step, the throats having entry capillary pressure less than the applied pressure connected to the invading phase gets invaded. Two types of percolation processes can be considered, namely ordinary percolation, and invasion percolation. In case of ordinary percolation, for each pressure step, all accessible throats (along with interconnected pores) having entry capillary pressure lower than the applied pressure gets invaded simultaneously. In case of invasion percolation, the process happens in increasing order of throat entry capillary pressure. The throat (and pore) with the lowest entry capillary pressure on the side of the network connected to the reservoir gets invaded with any connected throat having entry capillary pressure less than that. In the next step, among the throats connected to the invading phase, the throat or throats having the lowest entry capillary pressure gets invaded. This process is similar to a quasi-static rate-controlled injection process [73–75]. For such a process, capillary pressure can be expressed as a function of saturation of different phases in the network. In a pore network simulation, the configuration of the domain for different saturation points can be stored. Subsequently, transport simulations can be carried out for these configurations while keeping the interfaces unchanged [76, P. 130-131]. This way, relative permeability can be computed for the network under consideration.

2.6 Summary

In this chapter, the theoretical background relevant to this thesis was developed. The components of an electrolyser cell and their operation was studied. This was followed by a study of flow in porous media to develop the understanding of mass transport inside PTLs. Numerical modelling of multiphase flow and its implementation with respect to different tools of choice was also discussed.

Chapter 3

Literature Review

In this chapter, a brief review of the literature relevant to the current work will be presented. The thesis is mainly divided into two parts — modelling and simulation, and experimental measurement. Thus, the literature review is divided into two parts addressing both aspects. The first part describes the evolution of modelling and simulation approaches in the realm of PEM electrolysis over time. The second part addresses the experimental characterization of porous transport layers.

3.1 PEM Electrolyser Modelling and Simulation

Although PEM technology was developed in the 1960s, research related to modelling and simulation of PEM electrolysis started appearing only in the 1990s. After the year 2000, it got significant traction when a growing number of countries began to focus on shifting from fossil fuels to renewable sources of energy. Some of the earliest works in this area can be traced back to [77] and [78]. Based on the general approaches to model PEM electrolyser, modelling and simulation activities can be broadly classified into the following categories:

- General modelling
- Mass transfer
- 2-D modelling
- 3-D, 2-phase modelling
- Ancillary based modelling
- Wind/PV combination

- Membrane modelling
- Multi-scale modelling
- Pore network modelling
- Miscellaneous modelling

Different literature about modelling and simulation separated according to the above classification are presented in Table 3.1.

3.1.1 General Modelling

The modelling of PEM electrolyser cell based on empirical or semi-empirical approach is considered as general modelling. These models mostly represent component or cell behaviour as a current-voltage relationship described by zero or one-dimensional equations while ignoring mass transfer effects or detailed reaction kinetics. One of the earliest literature by Millet [77] developed an analytical model for the temperature profile across a Nafion® membrane. Based on validation by infrared thermography, it was found that the temperature profile depended on the membrane thickness and current density.

The cell potential is described as a combination of different overpotentials based on different assumptions. This approach defines cell voltage E as described by Equation 3.1

$$\tag{3.1}$$

where is Nernst or reversible potential, and the other terms are overpotentials due to anode activation, cathode activation, and the ohmic resistance respectively. Butler-Volmer equation is generally used for the activation overpotentials. The electrochemical reaction on the anode side (forward and backwards) is expressed as

$$\left[\left(\frac{}{}\right) \quad \left(\frac{}{}\right)\right] \tag{3.2}$$

where is the current density, is the exchange current density, is the charge transfer coefficient, is the number of electrons transferred, R is the universal gas constant, and T is the temperature. The subscripts and refer to anode and cathode respectively. Upon using and expressions for anode and cathode activation overpotentials are given by equations 3.3 and 3.4. Such expressions were first utilized by Choi et al. in 2004 [79]. In the following years various authors have used the same expressions for PEM electrolyser modelling [80–89].

$$\frac{}{} \quad \left(\frac{}{}\right) \tag{3.3}$$

$$\frac{}{} \quad \left(\frac{}{}\right) \tag{3.4}$$

where and are exchange current densities at the anode and cathode respectively. When high current density is considered, the activation overvoltage is given by Tafel equation. This equation is also common in literature. A list of such works can be found here [90–95]. This is written as shown in Equation 3.5

$$\frac{}{} \left(\frac{}{}\right) \tag{3.5}$$

If needed, the exchange current density can be expressed as a function of temperature linked to a reference exchange current density [79, 93, 96]

$$\left[\frac{}{}\left(- \quad \frac{}{}\right)\right] \tag{3.6}$$

where is the activation energy for the electrode reaction. The reversible cell potential under non-standard conditions is given by Equation 3.7

$$\frac{}{} \left(\frac{{}_2\sqrt{\quad {}_2}}{{}_2}\right) \tag{3.7}$$

In literature people have used different empirical formulae for the calculation of reversible cell potential. One such as formula is Equation 3.8. It was first used by Bernardi and Verbrugge in the early 90s to model fuel cell behaviour [97]. After a decade it was used by several authors for PEM electrolyser modelling [79–81, 87–89, 94, 98].

$$\tag{3.8}$$

Equation 3.9 represents another empirical relation that shows the reversible potential as a temperature dependent polynomial [82, 90, 93]

$$\tag{3.9}$$

Similarly, another such expression (Equation 3.10) was found from experimental data fitting by da Costa Lopes et al. [83]

$$\tag{3.10}$$

under standard temperature and pressure. Ohmic overvoltage is the sum of overvoltage due to membrane resistance and components' resistance. However, some authors consider only the membrane resistance [79–81, 83, 84]. In the simplest form, no effect of temperature and humidification is considered. Overvoltage due to membrane resistance can be expressed as

$$\frac{\quad}{\quad} \tag{3.11}$$

where and are membrane thickness and membrane ionic conductivity respectively. This is the most common expression, and can be found in literature referenced here [79, 81–84, 88, 95, 99]. According to Springer et al. [100], considering the thickness of the membrane and the variation in the degree of humidification, the local ionic conductivity can be written in the form shown in Equation 3.12. This has been used to model PEM behaviour in different subsequent models [80, 82, 85, 87–92, 94, 95, 99, 101].

$$\left[\quad\left(\frac{\quad}{\quad}\quad-\right)\right] \tag{3.12}$$

The local water content along the membrane thickness can be interpolated using the following equation

$$\frac{\qquad}{\qquad} \tag{3.13}$$

Here is the location, and the subscripts and refer to the interfaces on the anode and the cathode sides of the membrane, respectively. Then membrane resistance can be estimated as follows

$$\int\quad\frac{\qquad}{\qquad} \tag{3.14}$$

There exist other expressions for describing membrane conductivity. A diffusion-based expression is [85, 90])

$$\frac{\quad _{+}\quad _{+}}{\qquad} \tag{3.15}$$

where $_{+}$ and $_{+}$ refer to respective concentration and diffusion coefficients of protons. A temperature-dependent Arrhenius type equation is also used when the membrane is assumed to be fully hydrated [82, 93]

$$\left[\frac{\quad _{+}}{\quad}\left(\frac{\quad}{\quad}\quad-\right)\right] \tag{3.16}$$

where is conductivity at the reference temperature, $_{+}$ is temperature independent activation energy for proton transport.

One of the earliest modelling attempts of PEM lectrolysis cell can be traced back to 1991 [77]. Millet calculated the temperature profile across the thickness of the membrane. Subsequently, the complete cell behaviour modelling as a current-voltage relationship started in 2004 [79]. Choi et al. used Butler-Volmer equation for the activation overpotential, an empirical relationship for the reversible potential and a fixed membrane resistance for the ohmic overpotential. They also introduced a model for the exchange current density that depended on the catalyst layer's morphology and electrochemical behaviour. The same assumptions and relations were applied to an electrolyser stack of 20 series-connected cells to estimate exchange current densities and membrane conductivity by the authors Harrison et al. [81]. Based on the same approach, another group investigated the effects of exchange current density and temperature on cell performance [84]. A research paper by Ni et al. [80] used the same assumptions but defined membrane resistance as calculated by equations 3.12 and 3.14. They found that operating at higher temperatures with a thinner membrane was beneficial for system efficiency. A four degrees of freedom empirical model (Matlab based, non-linear least square parameter estimation) suitable for fuel cell or electrolyser or a regenerative fuel cell was reported by Busquet et al.[102]. The effect of current ripples on cell performance is also studied [83]. The researchers used the current interrupt method to determine the experimental cell's ohmic resistance, followed by the determination of the charge transfer coefficients and exchange current densities through parameter estimation. Linearized ohmic and activation potential relations are then used to investigate the effect of alternating current ripples on cell performance. The authors comment that the low-frequency ripples cause higher power loss which should be an essential factor for power converter design. Dedigama et al. [90] used activation overpotential as described by Equation 3.9 and 3.5. They considered the resistance due to the cathode, anode, and bipolar plates for the ohmic overpotential following an approach reported by Marr and Li [103]. This model was then compared with an experimental cell to fit the parameters for charge transfer coefficients, current densities and proton diffusion coefficient. Although the authors develop a discussion for the mass transfer phenomena, it is ignored in the implemented model. Rahim et al. [91] studied the effects of current density and temperature on cell performance using Butler-Volmer reaction kinetics.

Table 3.1: List of literature in different categories over the years

Year	General modelling	Mass Transfer	2D	3D, 2-phase	Ancillary based	Wind/PV combination	Membrane	Nano/Micros-scale	Pore Network	Other
1991	Millet P [77]									
1992	Goldberg AB [78]									
1994			Millet P [104]							
2002			Onda K [105]							
2004	Choi P, Bousket S [79, 102]									
2005						Kelouwani S, Khan MJ [106, 107]				
2006	Ni M, Harrison KW [80, 81]				Gorgun H [99]					
2007			Katukota SP [98]							
2008				Nie J [108, 109]		Nie, Garcia-Valverde [82, 110]				
2009	Lopes F [83]	Lebbal ME, Marangio F, Li X [85, 92, 111]		Kasukurthi SP, Nie J [112, 113]						
2010		Grigoriev SA, Medina P [114, 115]		Nie J [116]		Atlam O [117]				Becker S [118, 119]
2011					Awasthi A [95]					Agbli KS, Atlam O [120, 121]
2012		Garcia-Valverde R, Zhang H, Myles TD [93, 94, 122]						Oliveira LFL [123]		
2013		Schalenbach M [124]			Lee B [125]	Ahmadi P [126]		Oliveira LFL [127]		
2014	Dedigama I, Tijani AS [84, 90]	Fritz DL [86]				Aouali FZ, Tilli N [128, 129]				Beainy A [130]
2015	Rahim AHA [91]	Sauerman M, Han B, Guarnieri M [36, 87, 96]			Abdin Z [88]	Ozgirgin E, Devrim Y [131, 132]	Chandesris M [101]			
2016	Tijani AS [133]			Olesen AC [134]	Yigit T [135]	Laoun B, Mohammed B [136, 137]			Lee CH [26]	Olivier P [138]
2017		Han B [89]		Lafmejani SS [139]						
2018				Lafmejani SS [140]						

3.1.2 Analytical Models Considering Mass Transfer Effects

In the last section analytical modelling of PEM electrolyser without mass transfer effects was discussed. This section will deal with reports that have addressed the mass transfer effects like diffusion and gas bubble shielding in the analytical model. Mass transfer effects are included as a contribution to the cell potential in the form of an overvoltage. Thus, cell potential (Equation 3.1) becomes

$$\tag{3.17}$$

Nernst equation is used to estimate the diffusion overpotentials by comparing species concentration under certain operating condition( ) to species concentration ( ) under reference condition. This approach produces the following relationship [85–87, 89, 90]

$$\frac{\quad}{\quad}\left(\frac{\quad}{\quad}\right) \tag{3.18}$$

Another method to estimate diffusion overpotential is to define a limiting current density ( ). When the current density reaches this limit the rate at which reactants are consumed becomes equal to the rate at which the reactants reach the electrodes from the solution. Thus, diffusion overpotential can be expressed in the form

$$\frac{\quad}{\quad}\left(\quad\frac{\quad}{\quad}\right) \tag{3.19}$$

where is an empirical constant. This is adapted from the work of Fontès [141, P. 54] for PEM fuel cells. It becomes clear that when current density crosses the limiting value the reactant supply would be less than their rate of consumption. This method was used by Lebbal and Lecœuce for a steady-state electric and dynamic thermal model [92].

An alternative to this approach to modelling diffusion is to integrate a diffusion limiting current density in the the activation overpotential definition. Then the activation overpotential becomes [93]

$$\frac{\quad}{\quad}\left[\frac{\quad}{\quad}\left(\quad\frac{\quad}{\quad}\right)\right] \tag{3.20}$$

Another expression for the concentration overpotential is [94]

$$\left(\quad\frac{\quad}{\quad}\right)^{2} \tag{3.21}$$

where and are empirical constants.

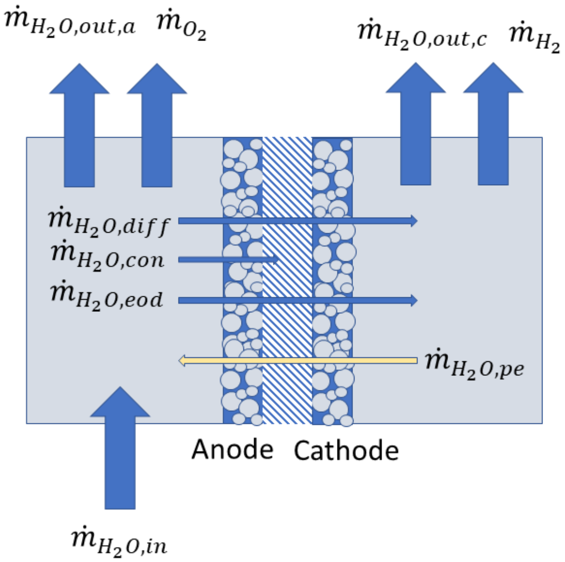

Figure 3.1: Different components of mass transfer inside PEM electrolyser

The mass transfer process in the electrolyser cell can be described as shown in Fig. 3.1. The subscripts , , , and refer to flow due to diffusion, consumption, electro-osmotic drag and pressure difference, respectively. Flow due to pressure difference happens when there exits differential pressure between the anode and the cathode. Some authors have considered detailed mass flow in their literature [85, 90, 114, 124]. A more detailed model would also consider the diffusion of oxygen from anode to cathode, the diffusion of hydrogen from cathode to anode due to concentration gradient, and a pressure-induced flow of water from cathode to anode in case of differential pressure operation. For the reactants and products as shown in Figure 3.1, based on the current and active area , the molar quantities can be calculated from the following set of equations

$$ {}_2 \qquad \frac{}{} \tag{3.22}$$

$$ {}_2 \quad \frac{}{} \tag{3.23}$$

$$ {}_2 \quad \frac{}{} \tag{3.24}$$

$$ {}_2 \qquad \frac{}{} \tag{3.25}$$

$$ {}_2 \qquad \frac{{}_2 \qquad {}_2}{} \tag{3.26}$$

$$ {}_2 \qquad \frac{{}_2}{{}_2 \qquad {}_2} \tag{3.27}$$

where is the electro-osmotic drag coefficient, is the diffusion coefficient of water through the PEM, $_2$ is the concentration of water on the anode side, and $_2$ is the concentration of water on the cathode side of the PEM. represents permeability. The terms $_2$, $_2$ and $_2$ represent density, viscosity and molar mass of water. is the pressure difference across the membrane.

Different researchers have used the mass transfer description described above to fulfil different modelling objectives. Apart from developing a better understanding of the mass transfer inside PEM water electrolysers and the effect of different parameters on performance, such models have focused on the improvement of efficiency, development of monitoring and control strategies [92], determination of electroosmotic drag coefficient [111], determination of optimum membrane thickness [114, 124] etc. Lebbal et al. [92]] developed a steady-state electric and dynamic thermal model for system monitoring and control. Marangio et al. [85] developed a model that considered PTL and bipolar plate geometry to calculate ohmic resistance. They observed that the polarization curve at lower current density has a better fit using Butler-Volmer kinetics for a high-pressure electrolyser . Still, at higher current densities Tafel equation provides a better fit. It was also noticed that for the same pressure, higher temperature operation leads to better performance. But Medina et al. have commented that for obtaining dry hydrogen at high cathode pressure, low current density operation is better. They carried out experiments using design of experiments technique. They found that electro-osmotic drag coefficient decreases with current density at every pressure and temperature, increases with pressure at every current density and temperature, and slightly increases with temperature at every current density and pressure [115]. Some researchers have also attempted to define the electro-osmotic drag coefficient as a function of temperature based on experimental data [111]. In an approach different from general modelling, Grigoriev et al. [114] developed a high pressure electrolyser model from first principles considering a detailed mass transfer process. They included the effects of gas bubbles and pore diameter on the cell performance and suggested method for finding optimum membrane thickness. A model for cell voltage prediction based on input current and stack temperature was reported by Garcia-Valverde et al. [93]. They observed that the assumption of a constant anode charge transfer coefficient is not valid. Zhang et al. [94] compared different configurations of a complete electrolyser system including heat exchangers, pumps and separators. A different approach to modelling mass transfer was employed by Myles et al. [122]. They used dusty fluid model based on the Stefan-Maxwell equation for multicomponent diffusion. They developed this model for an oxygen generating system and observed a strong influence of electro-osmotic drag on membrane dehydration. The investigation of the effects of anode and cathode pressure for various differential and balanced pressure operations on gas crossover by Schalenbach et al. [124] found that gas crossover losses dominate at partial loads and ohmic losses dominate at high current densities. However, in a following corrigendum, it was mentioned that hydrogen crossover was independent of anodic pressure [142]. Fritz et al. [86] suggested a model to optimize cell operation and cell geometry. Their work connected PTL pore diameter to the concentration overpotential in the cell. Suerman et al. [36] have reported that mass transfer effects are somewhat independent of pressure and contribute up to 25% of the total losses. In their model, similar to Marangio et al. [85], Han et al. [87] introduced interfacial resistance in calculating the cell ohmic resistance. In their model for a unitary cell (one system for electrolyser and fuel cell), Guarnieri et al. [96] used Carman-Kozeny permeability of the PTL corrected by relative permeability to find the concentration overpotential. Thus, the two-phase behaviour could be linked to cell polarization. Han et al. [87] studied the effect of PTL porosity, PTL contact angle and membrane thickness on cell performance. They developed a continuum based flow model that utilized Darcy equation and conservation equations to arrive at the capillary pressure, which was linked to the water saturation in the PTL through Leverett's function. It was observed that smaller contact angle, higher porosity and smaller membrane thickness improves cell performance.

3.1.3 2-Dimensional Models

It is observed that most of the PEM electrolyser models have been zero-dimensional, and few are three-dimensional. During our survey, we found only three reports dealing with the two-dimensional description of the PEM electrolyser cell. The earliest such model dates back to Millet [104] that calculated the potential distribution inside a Nafion membrane. Based on Butler-Volmer Kinetics and charge conservation, this model solved for the potential distribution at different temperatures for different anodic electrocatalysts using finite difference method. The next such model was reported by Onda et al. [105].

Here, a two-dimensional model validated for a small unit cell was used to predict a larger theoretical cell's performance by calculating temperature and current density profile for the system along the flow direction (from inlet to outlet) and across different components (perpendicular to the membrane). Katukota et al. [98] developed a two-dimensional, steady-state, isothermal model using Stefan-Maxwell equation for multicomponent diffusion, and Butler-Volmer kinetics. They observed current density spikes on the electrode corners. The three models discussed above used finite different method, control volume approach and finite element method (FEMLAB software) respectively.

3.1.4 3-Dimensional Two-phase Flow Models

In the field of PEM electrolyser modelling and simulation, only a handful of articles discuss three-dimensional two-phase flow. In the domain of PEM fuel cells, many researchers have worked in this area as reported in the review by Ferreira et al. [143]. The earliest 3D flow modelling of PEM electrolyser was reported in 2008 by Nie et al. [108, 109]. The same group published similar articles in the next few years that mostly focused on the bipolar plate of PEM electrolysis cell [112, 113, 116]. The first model considered single-phase flow in bipolar plate having straight flow channels with diagonal inlet and outlet assuming uniform heat transfer from the PTL side. The simulations and experimental validation commented that diagonal inlet and outlet with manifold header results in flow maldistribution and higher temperature at the exit header [108, 109]. This model was further extended to include the effects of oxygen generation. The oxygen generation from the PTL side is included as a mass flux condition corresponding to the current density. The model was simulated for a constant water flow rate with different gas flow rates and different bubble sizes. However, they found that for diameter within the range 0-100 µm the bubbles did not affect the flow behaviour. Due to the diagonally placed inlet and outlet of the bipolar plate, lower fluid velocity at the centre was observed. At higher oxygen flow rates (higher current densities), flow separation and reverse flow were observed [113, 116]. This bipolar plate design was modified to have straight channels and four inlets and four outlets in the manifold header in the next step. The modifications resulted in better flow distribution and better performance at higher current densities [112]. All these simulations were carried out in ANSYS Fluent. While SIMPLE solver was used to solve the problems, mostly simplifying assumptions were made to make the problems less computationally expensive. The mixture model was used for capturing the two-phase flow behaviour in the bipolar plate. Only Kasukurthi et al. [112] considered turbulence into their simulation model.

After nearly a decade, another investigation of a 3-D, two-phase flow in a high-pressure PEM electrolysis cell with circular-shaped interdigitated bipolar plate was reported by Olesen et al. [134] in 2016. Their model used experimental data for titanium felt of 350 µm thickness and 81 % porosity to define the porous media model for the PTL. Single-phase simulation was performed to study the effect of geometry on the flow behaviour. The two-phase flow simulation considered the two-fluid interpenetrating continua model where the gas flow was defined as a mass flux based on uniform current density at the PTL-microporous layer interface. For the two-phase flow in the PTL Van-Genuchten model was used to describe the relative permeability behaviour. The simulations were carried out using the ANSYS CFX solver. It was shown that improved mass flow distribution could be achieved by reducing the gap between the longer channels or increasing the gap between the shorter channels. It was also found that higher permeability of the PTL resulted in increased flow maldistribution. Moreover, the larger particle size for the oxygen bubbles resulted in maldistribution and gas hold-up. For the design under consideration, a stoichiometry greater than 350 was suggested. Based on the same design, a two-phase flow simulation using the VOF model of ANSYS Fluent was performed by Lafmejani et al. [139]. For this, two inlets and one outlet channel of the interdigitated bipolar plate were considered. The PTL was modelled according to the Ti-felt experimental data, capillary pressure was ignored, and the eddy-viscosity model was used to capture turbulence. The gas generation rate corresponded to a current density of 1 , and a stoichiometry value of 1000 was used. It was observed that uneven velocity distribution occurred along the second half of the outlet channel due to gas accumulation. The uneven gas distribution caused a build-up of uneven pressure resistance at inlet channels, resulting in water flow variation from the inlet channel to PTL. However, in their experimental work for a similar case, it was observed that gas bubbles occurred at preferred locations with larger pores on the PTL surface resulting in different flow-regimes [144].

We observe that, so far, all the reported articles have mostly considered the two-phase flow in the bipolar plate microchannels. The PTL is generally modelled using conventional porous media model of CFD. Only one report has considered the actual 3D structure of the PTL. Apart from titanium felt, or sintered titanium, which is typically used as PTL material, people have also considered expanded metal mesh for PTL. Lafmejani et al. have carried out experiments and simulations to study the flow in such expanded metal meshes [140]. The expanded metal mesh was tested in a transparent plexiglass cell (without any electrolysis activity) using different water and gas flow rates to determine the viscous and inertial properties. Flow development pattern was also studied by injecting ink into the flow. For the cell having two metal meshes of size 0.5 1.5 in the vertical direction, it was observed that the gas lifts the liquid along the path like an airlift pump at higher gas flow rates. From the experimental data, the whole metal mesh was first modelled using porous media model to simulate the flow of inkjet in the water. A tiny section (5 units and 2 half units) of the expanded metal mesh was modelled in three dimensions, and single-phase flow was simulated in the next phase. The simulation results showed agreement with the recirculation zones observed during the gas-liquid flow experiments. They commented that such meshes could be suitable for high current density operations.

3.1.5 Ancillary Based Models

Another approach to modelling PEM electrolyser is to divide the system into different ancillaries. This method involves creating cathode, anode, membrane, and voltage ancillaries with their respective details and interfaces by using a suitable tool. Görgün first introduced ancillary based modelling of PEM electrolyser in 2006 [99]. Other researchers later followed this approach. This approach's precursor can be found in earlier works related to systems connecting wind or PV sources with electrolyser and fuel cells in a complete setup. Such modelling activities can be found in the works of Kelouwani et al., and Khan and Iqbal [106, 107]. One standard tool used for ancillary based modelling is MATLAB Simulink.

Typically, the description of the anode and the cathode ancillaries are based upon each species' mass balance in a manner described in Section 3.1.2 and Fig. 3.1. Faraday's law determines the amount of substance produced or consumed. Sometimes Faradaic efficiency is also considered [99, 125]. The membrane ancillary deals with the species transfer between the cathode and the anode. The description typically considers diffusion and electro-osmotic drag. Sometimes the transfer of water from the cathode to the anode side due to pressure difference is also considered [88, 95]. The voltage ancillary sums up the reversible potential and all other overpotentials. The activation overpotential is calculated using either Tafel [99] or Butler-Volmer equation [88, 95, 125, 135]. Ohmic resistance usually includes the membrane resistance as a function dependent on the degree of hydration, and temperature described by Equation 3.12. Abdin et al. [88] also considered the ohmic resistance due to the electrodes and bipolar plates in a manner similar to Marr and Li [103]. They considered a storage ancillary assuming containers are slowly filled with hydrogen to the electrolyser pressure [99, 125]. In another work, Yigit et al. considered storage and took into account the balance of plant in their model [135].

Even though these models [95, 99, 125] claim to capture dynamic response, Abdin et al. rightly point out that these models are not dynamic in a real sense [88]. These models only changes current and produce an instantaneous response in their output, which is not actually transient in time and does not really mean a fast transient response. Any physical system like this has some delay no matter how quick its response is.

3.1.6 Models in Combination with Solar or Photo-voltaic Cells

Hydrogen production by electrolysis would be successful only when the energy required would be produced from renewable sources like wind power, solar power or ocean thermal energy conversion(OTEC) systems. Their intermittent nature poses as a bottleneck in their deployment as a direct energy source for practical purposes. There have been attempts to combine these sources with electrolysers, fuel cell, batteries and capacitors in different combinations, and various researchers have reported modelling approaches to the same.

In this approach, different methods to describe various components of the system can be observed. For the photovoltaic part, Kelouwani et al. have considered only the available power data [106], while others have considered time series for hourly or monthly power production data [82, 129, 131, 132, 136]. Aouali et al. have considered it as a power-voltage curve with maximum power point tracking (MPPT) [128]. Kelouwani et al. [106] only considered available data for wind power, but Khan et al. [107] modelled output power as a function of available wind power and time. The simplest model of an electrolyser is hydrogen production based on Faraday's law [107]. Other researchers have adopted similar technique [129, 131, 132]. Usually, the electrolyser cell voltage is modelled as the sum of the reversible cell potential, and activation overpotential (based on Butler-Volmer kinetics) [126, 128]. Sometimes it includes mass transer overpotential [82, 136]. Keluwani et al. have modelled the electrolyzer V-I curve in their dynamic model as a function of current, time and temperature [106]. In an interesting model of a solar photo-electrochemical electrolysis system, Nie et al. [110] included the photochemical reaction as an overvoltage term in the electrolyser V-I curve. Atlam et al. have described cell potential as a function of the current [117]. A fuel cell in the system is modelled using Faraday's law [131, 132] or a V-I curve based on Butler-Volmer equation [129]. Some dynamic models have utilized a V-I curve that is a function of both time and current [106, 107].

It is observed that some researchers have combined wind, photovoltaics, electrolyser, fuel cell and batteries in one dynamic system model [106]. Khan et al. have reported another dynamic model where ultracapacitors are used in place of batteries [107]. One group has also considered OTEC with solar power as well [126]. Thus, we can comment that there have been trials to combine different renewable sources to hydrogen energy systems. The researchers have focused on finding optimum operating conditions, control strategies of the devices or calculating scenarios for different locations based on their renewable energy availability.

3.1.7 Membrane Degradation Modelling

Membrane degradation has a significant impact on PEM electrolyser performance. However, modelling of this topic has received little attention. Only one report by Chandesris et al. [101] could be found in the literature. This 1-D model considers the membrane and two electrodes as a system where the catalyst layers are regarded as interfaces. From the cell V-I curve, the activation overpotentials are determined by subtracting the other overpotentials. Fitting this to the experimental data for a single cell gives the value of charge transfer coefficients. Membrane degradation phenomenon can be summarized as follows:

- Gas cross-over from anode to the cathode side through diffusion and electro-osmosis
- Oxygen reduction reaction leading to hydrogen peroxide formation
- Decomposition of hydrogen peroxide into hydroxyl and hydroperoxyl radical with or without the presence of ferrous ions
- The parasitic consumption of radicals and attack on the membrane by the hydroxyl radical leading to fluoride release and membrane thinning
- The whole process is defined as a 9-step reaction

The researchers found that at lower current densities the fluoride release rate increases with current density, which then reaches a peak, and goes down with further increase in current density. Membrane thinning is modelled as a rate equation that takes into account the changing membrane thickness and fluoride release rate. It was found that membrane thinning happens faster at higher temperatures. It is important to note that the process is nonlinear, and non-consideration of the coupling effect of changing membrane thickness may lead to overestimation of membrane life expectancy.

3.1.8 Multiscale Models

Most PEM electrolyser models have mainly focused on description derived from empirical relationships, general multi-phase behaviour, or effect of different variables on the cell performance. So far, only one group has reported research that resolves fundamental physicochemical phenomena resolved at nano and micro-scale. Oliveira et al. developed such first principle-based multiscale models for PEM electrolysis [123, 127]. This work was an adaptation of methods earlier developed for similar phenomena in PEMFCs [145–147]. In their PEMEC anode model, they modelled the catalyst-electrolyte interface at the nanoscale taking into account the non-equilibrium behaviour. DFT based calculations were used to analyze the stability and adsorption of OER intermediates on the catalyst surface. The nono-scale model consists of three parts— diffuse layer, compact layer and kinetic model, that took into account species transport, water adsorption and OER steps respectively. The microscale model took care of oxygen and proton transport. Appropriate boundary conditions connected these two scales. MEMEPhys software was used in combination with Matlab/Simulink to solve the equations. Finally, cell potential's temporal evolution, temperature effect on cell performance, and catalyst degradation were studied. The results showed that a greater number of water molecules got absorbed at the catalyst surface at higher temperatures, resulting in higher performance [123]. In the next step, the researchers extended this approach to the whole MEA. This included different behaviour at the cathode, HER and the addition of the membrane into the model. Coverage of different species at different temperatures on the catalyst surface, polarization curve for and , sensitivity with respect to temperature and catalyst loading were studied through simulations [127]. Both of these models described electrolysis behaviour without using the Butler-Volmer approach. However, bubble transport or membrane degradation was not considered.

3.1.9 Pore Network Models

Pore network models allow simulation of pore scale phenomena in complex pore geometry with relative computational ease. This method is used extensively in petroleum studies, and it has also been used in PEMFC simulations, mainly for the gas diffusion layers. Such activities are reported by the group of Gostick et al. [148–153]. Lee et al. have used pore network model combined with microfluidic experiment for the titanium felt PTL used in PEM electrolyser [26]. They extracted a three-dimensional pore network from a 3-D reconstructed µ-CT image of a PTL and then created a representative 2-D model using the relevant parameters from the 3-D network. A scaled version of this representation was then printed using microfabrication technology. This scaled 2-D network was then calibrated to the right height by computing the corresponding permeability. This PTL-on-chip was constructed using multi-layer photolithography. For the experiments, polydimethylsiloxane and ethanol mixture was used as the defending phase, and air was used as the invading phase. The results were observed using an optical microscope with a fluorescent light source. Different gas flow rates were used to simulate different current density situation. They observed that at lower gas injection rates, a pressurization penetration mode of gas transport occurred. This behaviour showed the dominance of throat capillary pressure on the gas flow. Very importantly a limiting throat was observed, the penetration of which is immediately followed by breakthrough and which acts as the location for gas snap-off. The distance of the limiting throat also determines the average gas saturation after snap-off. Extending observations made by Lettenmeier et al. [154] they have commented that by locating the limiting throat in the backing layer near PTL-CL interface performance of the cell can be improved. Competing pathways at higher gas flow rates similar to invasion percolation simulations were also observed in the experiments.

3.1.10 Miscellaneous Models

A PEM electrolyser is a complex system consisting of many different parts. Moreover, the processes in such a system involve multi-physics, multi-scale and dynamic behaviour. Analysis, control and monitoring of such a system are essential. Researchers have tried different methods to describe such a system. One research group has utilized neural network-based models for prediction and control of electrolyser performance. In two separate reports they have used Adaptive Neuro-Fuzzy Interference System(ANFIS) and Optimization Layer by Layer (OLL) neural networks to predict hydrogen production rate, stack and system efficiency based on input power production parameters acquired through data acquisition system [118, 119]. Such a method has the potential to offer the possibility of online monitoring and control of the system. Agbli et al. have utilized energetic macroscopic representation (EMR) approach to model stack and tank temperature evolution for an electrolyser system. This approach, mainly used in the domain of analysis and control of the electromechanical system, allows graphical representation of each component based on the causality principle. This graphical description offers more readability and flexibility due to its modular approach [120, 155]. Creating equivalent electric circuits is another method to describe an electrolyser system. It is a semi-empirical model where the expression for the system's voltage and current are defined from the polarization curve and this is utilized to create the equivalent circuit. These expressions can be further utilized to calculate the hydrogen production rate and efficiency [121, 130]. In another graphical method similar to EMR, Olivier et al. have used Bond Graph formalism to describe an electrolyser system. Modular approach in the bond graph method allows the simulation of dynamic and multi-physics phenomena and facilitates control system's integration into the model [138].

3.1.11 Discussion on PEM Electrolyser Modelling and Simulation

Even though the PEM electrolyser modelling and simulation started in the early 90s, it is visible that the systematic and incremental development happened only after 2000. The chronological study of modelling approaches described above shows that the semi-empirical analytical method has been the most prevalent approach. This approach represents the cell behaviour as a polarization curve by considering different overpotentials. The simple steady-state models further led towards models that studied temperature dependence, the effect of membrane hydration on cell performance, different flow processes occurring inside the cell and mass transfer effects at higher current densities. Some dynamic models were also developed; however, most of them were not truly dynamic. Some of these models were developed for system monitoring and control. Three-dimensional computational fluid dynamics-based models have mostly focused on the bipolar plate flow channels. The porous transport layers are generally modelled using the porous media model commonly used in general computational fluid dynamics analysis. A large part of the literature focuses on combining wind or solar power systems with PEM electrolysers without considering the electrolyser system in detail. So far, only one report has studied membrane degradation and reaction kinetics. Similarly, the catalyst layer or multi-scale modelling has received little attention. Except for one pore-network based model the porous transport layers have not received much attention regarding the effect of their microstructure on the cell performance. There have been attempts to incorporate different techniques into modelling and simulation such as density function theory, neural networks, bond graph models or energetic macroscopic representation, but so far these efforts have not been consistent.

3.2 Experimental Characterisation of PTLs

There exist different methods to characterise porous materials. Two critical parameters for porous materials are absolute and relative permeability. This thesis is mainly concerned with these two parameters, and this section will focus primarily on literature related to the characterisation of PTLs concerning the same. Since reports strictly related to PEM electrolyser PTLs are limited, reports pertaining to gas diffusion layers (GDL) of PEM fuel cells are also included.

The general measurement principle for absolute permeability is based directly on Darcy's law or its adaptation. For flow with inertial effects, Forchheimer's law is also used. One of the earliest measurements could be found in Dohle et al. [156]. They measured in-plane permeability for a single material with different microporous layers. They also reported a difference in measured permeability for air and water. Williams et al. [157] measured through-plane absolute permeability of the PEMFC gas diffusion media using nitrogen gas. They choose carbon materials from E-TEK, SGL and Toray. All the GDLs had macroporous carbon substrate and hydrophobic microporous layers. Ihonen et al. [158] and Prasanna et al. [159] have done measurements for similar materials. Gostick et al. [23] measured in-plane and through-plane permeability of pure GDL substrate without any microporous layer. They measured in-plane permeability for rectangular samples and through-plane permeability for circular samples of different carbon-based GDLs from SGL, E-TEK, Ballard, and Toray. They also measured GDL permeability as a function of compression. Feser et al. [24] measured in-plane permeability for different GDLs using a radial flow device and found nearly identical permeability values for both air and water. Gurau et al. [160] also measured in-plane and through-plane permeability for two carbon substrates with different microporous layers. Through-plane permeability of sintered titanium PTLs was measured by Hoeh [27, P. 63-64]. The sample thickness varied in the range 230-290 µm. They were sintered at temperatures between 750 °C and 950 °C with an increment of 50 °C. Their measured values were within 10-140 mD.

In the field of geology or petroleum engineering, there are many studies related to relative permeability measurement. Depending upon the measurement principles, there are two broadly divided methods — steady-state method and unsteady-state method. Among these are Penn-state method, stationary fluid method, Hassler method, Hafford method, and JBN method. One can find more details in Dullian [50], Honarpour et al. [161, P. 1-6], and Johnson et al.[162], or any other relevant literature. Based on the steady-state method, the first attempt at measuring relative permeability of GDL was reported by Nguyen et al. [163]. In this experiment, they utilised neutron radiography to determine water saturation.

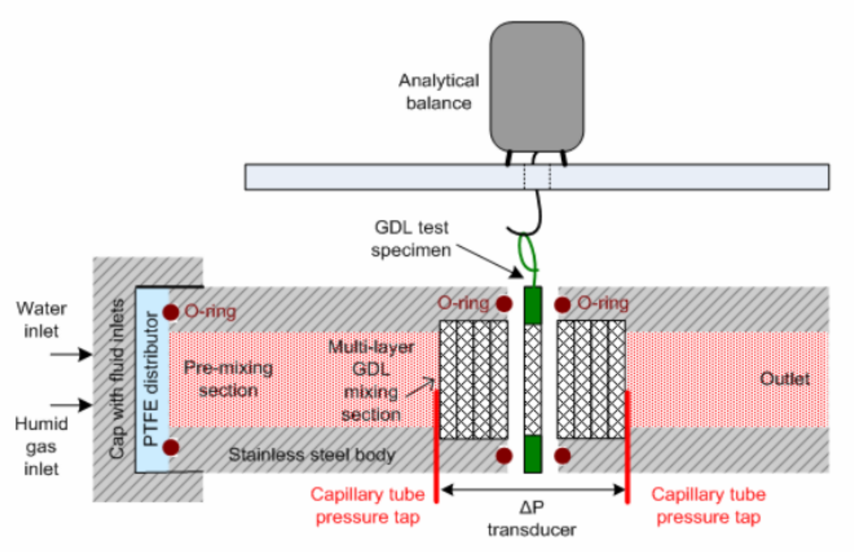

Figure 3.2: Relative permeability measurement cell used by Sole [20, p. 87]

Based on the Penn-state method, Sole [20] designed an innovative test cell to measure relative permeability of GDLs. Although it used a gravimetric method to measure water saturation, it had the provision for weighing the test sample immediately upon reaching the steady-state. This model also utilised a GDL mixing section on both sides of the sample to minimise end effects. Based on these experiments, it was found that hydrophobic treatment did not much alter the capillary pressure curves, but strongly influenced relative permeability behaviour. He measured both carbon cloth (BASF B-1A) and carbon paper (Toray TGPH-090) with (20 %) and without PTFE treatment. The treated samples were measured in both compressed and uncompressed state. The permeability of the samples varied approximately between 1-34D. In case of uncompressed GDLs, water relative permeability was measured for the PTFE treated samples. But the measured values were less than 0.01. For compressed carbon paper with PTFE treatment, water relative permeability was slightly higher at around 0.025. In the case of carbon cloth, compression decreased water relative permeability. Later, Ramos-Alvarado et al. [164] used the same design to study the effects of PTFE treatment on Toray TGP-90 gas diffusion media flow properties.

Hussaini and Wang [22] presented another design as the one discussed above to measure in-plane and through-plane permeability of Toray-060, -090, -120 carbon paper and E-TEK carbon cloth. The absolute permeability measurements are summarised in table 3.2. Their results showed that in-plane relative permeability was higher than that of through-plane relative permeability. Water relative permeability values were less than 0.01 within the measured range of saturation values (less than 80 %) when measured in the through-plane direction. Within a saturation value of less than 60 %, in-plane water relative permeability values were less than 0.03 for all the samples. Air relative permeability quickly dropped to a value less than 0.1 for approximately 10 % saturation in the through-plane direction. In the in-plane direction, the relative permeability values decreased slowly with increasing water saturation.

Table 3.2: Details of permeability measurement by Hussaini and Wang [22]

Material	Thickness ( )	Through-plane		In-plane	
		Compression (%)	K (D)	Compression (%)	K (D)
Toray-060	203	6	21.1	16	12.8
Toray-090	280	9	12.4	9	14.6
Toray-120	356	7	14.9	14	11.5
E-Tek cloth	280	16	64.6	9	37.2

From the two reports by Sole, and Hussaini and Wang, it was observed that Sole [20] used a linear fit to the relative permeability measurements, while Hussaini and Wang

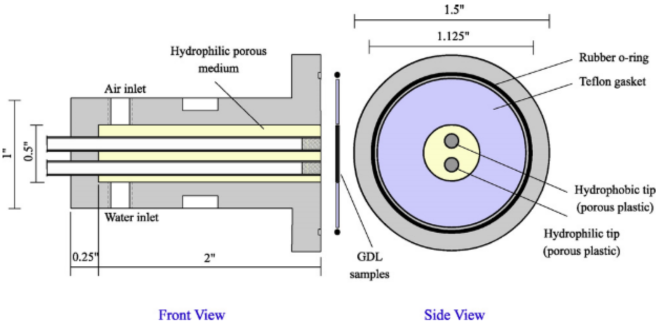

(a) Through-plane

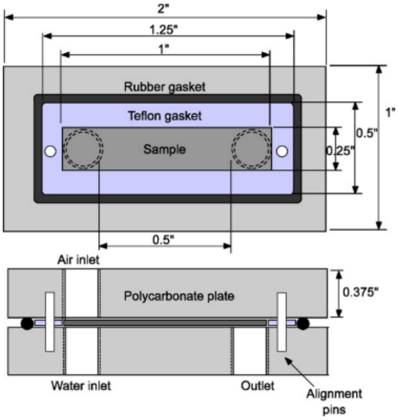

(b) In-plane

Figure 3.3: Relative permeability measurement cell used by Hussaini and Wang. Reproduced from ref [22] with permission from Elsevier

[22] applied a polynomial fit to the data. For both cases, water relative permeability curves differed from the commonly accepted function. Although these authors have successfully measured relative permeability of GDLs while using gravimetric method for saturation determination, another research by Dwenger [25] had difficulty measuring relative permeability using similar technique.

3.3 Summary

This chapter has reviewed the literature related to modelling and simulation of PEM electrolyser and experimental characterization of porous transport layers. This chapter has presented PEM electrolyser modelling and simulation from a chronological perspective. Rather than following a strict component-based classification or a phenomenon-based classification, this work has presented the reviewed reports based on approaches that can be understood and related to the existing body of literature. Although there has been incremental development in certain aspects of PEM electrolyser modelling and simulation, it has been critically observed that certain areas such as membrane, catalyst layer and porous transport layer need much more attention in future. Moreover, multiscale and multiphysics simulation can also be a possible future direction. A review of experimental characterization revealed that only a handful of papers have dealt with multi-phase flow. While early characterization attempts can be traced back to the early 2000s, no standard procedure for such characterization exists. It was also noted that these techniques stem from similar studies from the characterisation of rock samples, but specific correlations from those experiments may not be directly applied to PTLs.

Chapter 4

Computational and Experimental Methods

This thesis consists of simulation and experimental parts. This chapter will provide details on the relevant simulation and experimental methods. It is essential to prepare the porous media geometry in a suitable format for single and two-phase flow simulations. Thus, image processing takes an integral part of the process. This chapter will explain the image processing steps in detail. An overview of the tools, namely OpenPNM, ANSYS Fluent, GeoDict and Lattice Boltzmann Method (LBM), will also be provided. This chapter will also deal with the experimental methods, experimental setup design, and the testing procedure.

4.1 Sequence of Operations

The general outline of the methods is described in Figure 4.1. The titanium porous transport layers were manufactured in-house at Forschungszentrum Juelich. Once the samples were obtained, they were cut into a size suitable for permeability measurements. These samples were measured, and quantities of relevance like porosity, thickness etc. were noted. These samples were then used for both in-situ and ex-situ measurements. From the same materials, tiny portions of the size of 1 were cut for -CT imaging. These specimens were then photographed at IEK3, FZJ using a Zeiss Versa CT-imaging machine[1]. After capturing, the images were processed using ImageJ/Fiji software, which is a widely used scientific image processing tool. The commercial software GeoDict also

---

[1] Imaging of some earlier specimen were also carried out at Helmholtz-Zentrum, Berlin as part of a previous doctoral dissertation by Michael Hoeh

provides image processing options, but mostly ImageJ/Fiji was used for this thesis. The preliminary processing (refer Section 4.3) using ImageJ/Fiji and GeoDict is sufficient to produce inputs suitable for simulation in GeoDict or Lattice-Boltzmann method. For pore network modelling, the processed images were stacked to create a 3-D volume from where a network representation of the porous domain was extracted. On this extracted network pore network simulations were performed. For finite volume solver of ANSYS Fluent, a 3-D mesh of the porous domain needs to be generated from the processed images. A 3-D stack similar to the pore network extraction method was created. From this stack, 3-D pore volume was constructed. This volume was further processed for geometry clean up, simplification, or modification. In the next step, a 3-D mesh of the flow domain was created (refer Section 4.4) . On this mesh, single and two-phase flow simulations were performed.

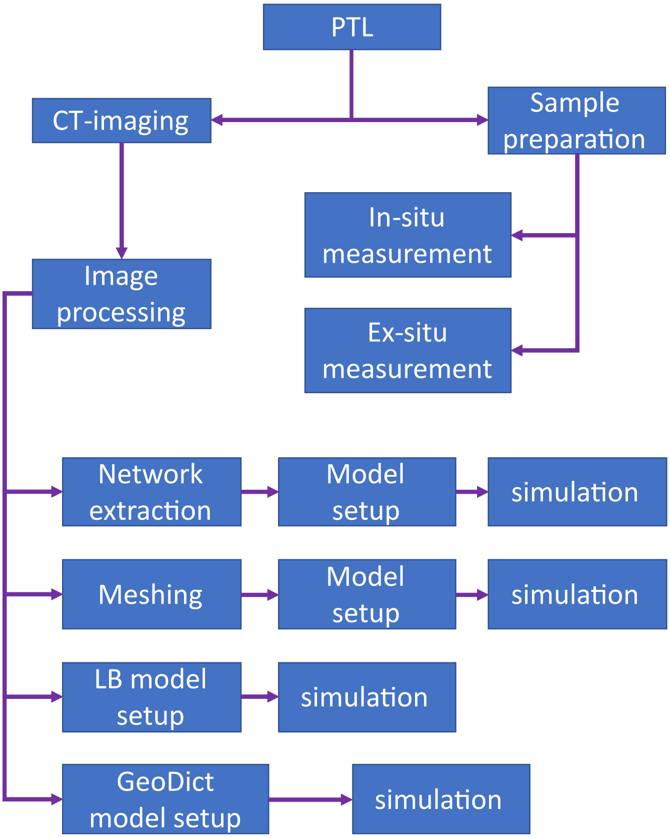

Figure 4.1: Process sequence for the experiments and the simulations

Different test cells were constructed for the experimental measurements. The test cells (refer Section 4.5) and the respective material samples are described in their relevant sections (refer Section 5.1).

4.2 Overview of Simulation Tools

This section provides an overview of the tools used for the flow simulation inside PTLs. The tools used in this work are OpenPNM, ANSYS Fluent, GeoDict, and Palabos. Below a brief description of each tool is provided.

4.2.1 OpenPNM

OpenPNM is an open-source Python-based package for pore network modelling. It was first introduced in 2013 [165]. The latest version used in this thesis is V2.0, and it is based on Python 3. The previous version of OpenPNM was based on Python 2. Both versions of OpenPNM were used in this thesis. There are some differences with respect to the structure of different packages between these two versions, but the basic principles remain the same. OpenPNM utilizes Numpy and SciPy Python packages, and this facilitates an optimized solution of numerical problems. It provides standard functionalities, and it can be freely customized to suit particular requirements. It includes different options like creating or importing a network, setting up geometry, phase definitions, physics definitions, various algorithms, and input and output processing. A detailed description of the structure, implementation and usage of the OpenPNM software is described in the relevant literature by Gostick et al. [72].

An outline of the simulation process in OpenPNM is shown in Figure 4.2. OpenPNM provides different algorithms for simulating porous media flow. These algorithms can be classified into two categories: percolation algorithms and transport algorithms.

4.2.2 ANSYS Fluent

ANSYS Fluent is a commercial fluid flow solver. Fluent is a part of ANSYS workbench. The Fluent solver was first released in 1983 by a collaboration between Creare Inc. and Sheffield University in the UK. It soon became prevalent in the industry, and after going through many changes, it was acquired by ANSYS Inc. The version used in the current work is ANSYS2019. The Fluent solver can be started as a standalone application or as a part of the ANSYS Workbench. On workbench, it provides options for complete workflow from geometry modelling to post-processing.

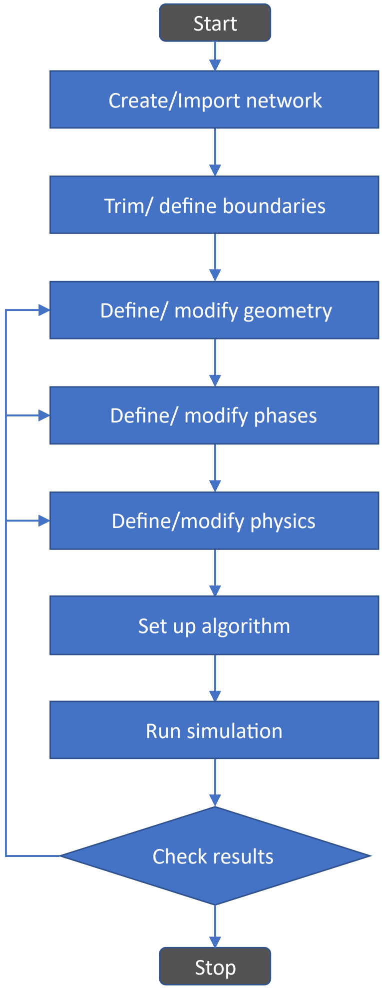

Figure 4.2: Process outline for simulations in OpenPNM

Fluid flow problems can be described using mass and momentum conservation equations. Energy conservation or some other forms of transport equations may also be required depending on a given situation. Discretized form of the conservation equations are solved for for the velocity field, but the momentum equation requires finding the pressure gradient. Thus, both pressure and velocity fields become coupled. ANSYS Fluent includes both density-based and pressure-based solvers for fluid flow problems. The pressure-based solver's pressure field is calculated by solving a pressure correction equation based on continuity and momentum equations. A density-based solver estimates the density field from the continuity equation, and the equation of state is utilized to calculate the pressure field.

There are two options for pressure-velocity coupling in a pressure-based solver, namely segregated solver and coupled solver. Mass conservation is obtained in a segregated solver using a pressure correction equation, followed by the pressure field calculation. A pressure field in the momentum equations is first assumed, and then the solution for the velocity field is computed. The pressure correction equation is used to update the pressure field; which is then applied to update the velocity field. This procedure is repeated until both momentum and continuity equations are satisfied. Because these processes happen separately, the solver is called a segregated solver. The segregated nature results in low memory requirement and computational resources. But the iterative nature may lead to slower convergence. ANSYS Fluent provides different options for segregated solver like SIMPLE (Semi Implicit Method for Pressure Linked Equations), PISO (Pressure-Implicit with Splitting of Operators), SIMPLEC (SIMPLE-Consistent) etc. A coupled solver solves both momentum and continuity equations simultaneously. This process demands that all the variables are stored and solved simultaneously. Thus, it becomes more memory intensive and computationally demanding for a given iteration than the segregated solver. But due to the couples nature of the equations, it can produce better convergence of the solution. Further details on different options can be found in the ANSYS Fluent theory guide [54].

4.2.3 Palabos: Parallel Lattice Boltzmann Solver

Palabos is a C++ based software library developed in 2010. It has its origin in the software OpenLB which was developed by the Palabos project's founders in 2007. Palabos does not share its code with OpenLB but follows a similar philosophy regarding data structure, model implementation and the coupling between different models. The University of Geneva and Flow Kit-Numeca Group Sàrl have been jointly developing it since 2011. There is a commercial version of Palabos called Omnis$^{\text{TM}}$/LB as well, but the open-source version is controlled by the University of Geneva [166]. It is natively written in C++ and offers an interface for Java and Python programming. Moreover, this software is suitable for operation in large supercomputers. Palabos has the preprocessor included, and different models like heat-transfer and multi-phase flow can be implemented with pore-scale accuracy without compromising on parallel efficiency. Palabos includes various functionalities for physics, fluid models, boundary conditions, particles, grid, and parallelism. It also allows pre and post-processing. The output can be saved as an ASCII or binary file, or directly as GIF images. It also supports output in VTK format for further post-processing. The work-flow for running simulations in Palabos is shown in Figure 4.3. The

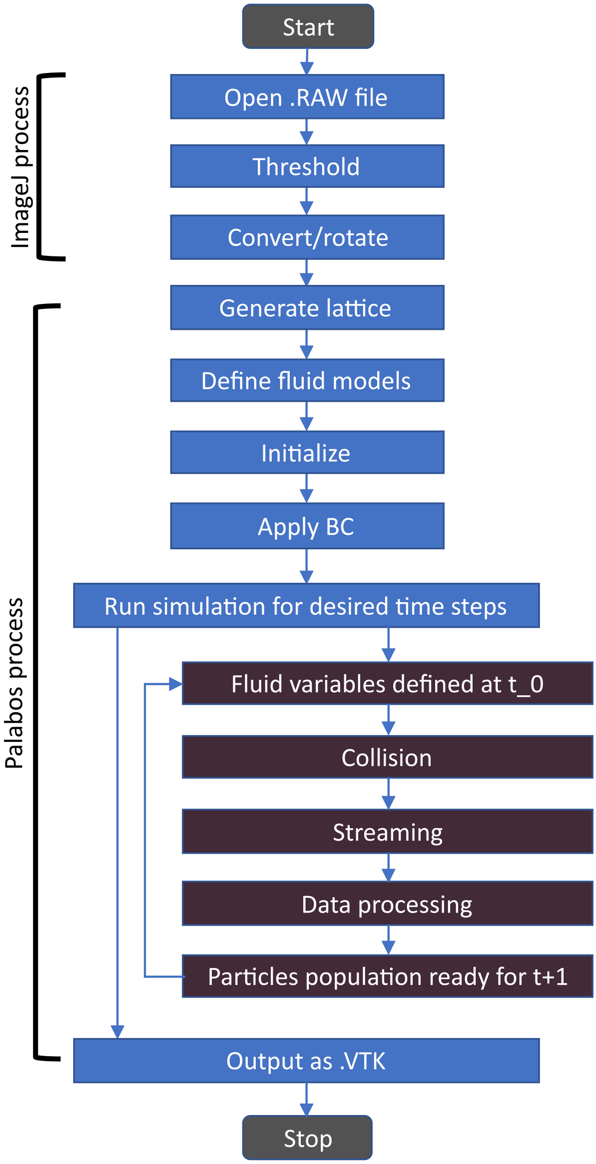

Figure 4.3: Flow-chart showing steps for running simulations in Palabos

application for simulating single-phase, single-component gas transport in the 3-D reconstructed porous media was developed at the IEK-3, Forschungszentrum Juelich [167–169]. The simulations were run on the JURECA cluster[2].

4.2.4 GeoDict

GeoDict is a digital material laboratory developed by Math2Market GmbH. It started in 2001 as a team at Fraunhofer Institute for Industrial Mathematics (ITWM) situated in Kaiserslautern. In 2011 the team formed Math2Market GmbH as a spin-off from the parent company. GeoDict offers different solutions for different industry sectors like digital material design, filtration, digital rock physics, batteries and fuel cells. GeoDict contains different modules for solving different types of problems. For example, FiberGeo module is suitable for working with fibrous materials. GrainGeo module can be used for creating

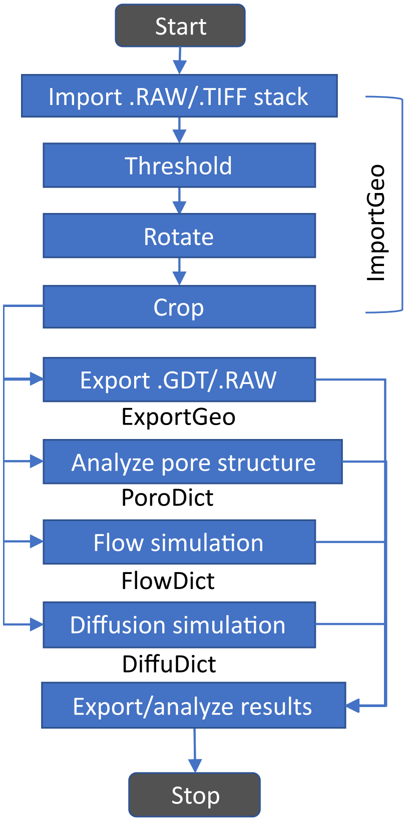

Figure 4.4: Process outline for simulations in GeoDict

---

[2] Simulations were performed by Dieter Froning at JURECA cluster, Forschungszentrum Juelich.

virtual materials from grains by way of piling, packing or sintering etc. For this thesis, only the modules relevant for the work were used, namely ImportGeo, ExportGeo, DiffuDict, FlowDict and PoroDict. The importGeo module allows importing its native files (*.gdt, *.gad) or any other supported file formats like *.RAW, *.TIFF, *.STL etc. After importing the files can be cropped, thresholded or rotated. There are different options to process the files according to requirements. The ExportGeo module allows the export of the geometry or results in the native (*.GDT or *.GAD) or one of the supported formats (*.MSH, *.RAW, *.STL etc.). PoroDict module is used to analyze different pore structure properties. FlowDict and DiffuDict modules are used for the computation of flow and diffusion properties of the materials. The PoroDict module has options for granulometry (pore structure analysis based on geometry), and porosimetry (similar to mercury intrusion porosimetry). The Stokes flow model of FlowDict is used for computing permeability. For solving the equations, there are three solver options in FlowDict: EJ (Explicit Jump), SimpleFFT (Simple Fast Fourier Transform) and LIR (Left Identity Right). For this thesis, EJ and LIR solvers were used. GeoDict employs an approach similar to the Lattice Boltzmann Method. Unlike conventional CFD tools, it does not require a mesh of the computational domain. The equations are solved on the binarized voxel space. More information can be found in the relevant publications [170–172]. The work flow for running simulations in GeoDict is shown in Figure 4.4.

4.3 Image Processing

Image processing forms an essential part of this work. The inputs for simulations were prepared from 3-D reconstructed porous media. 2-D images of different cross-sections of the PTLs were acquired using either synchrotron radiography or µ-CT machines for this purpose. This produced a large number of 32-bit greyscale images having pixel values between 0 and . Such images may also contain some noise that needs to be filtered in the next steps. Usually, a 3-D volume of pixels would require a considerable amount of computer memory and demand long computational time for methods like Lattice Boltzmann or CFD. Thus, it was necessary to process the images to eliminate the noise and reduce the file size without compromising on the details and image quality. This was done using ImageJ, a tool widely used by the scientific community for image processing. The image processing work-flow is shown in Figure 4.5. All the images were processed on a workstation with 16 cores @2.2 GHz (32 with hyperthreading) and 128 GB of RAM. For each sample, the memory requirement was in the range of 30-100 GB.

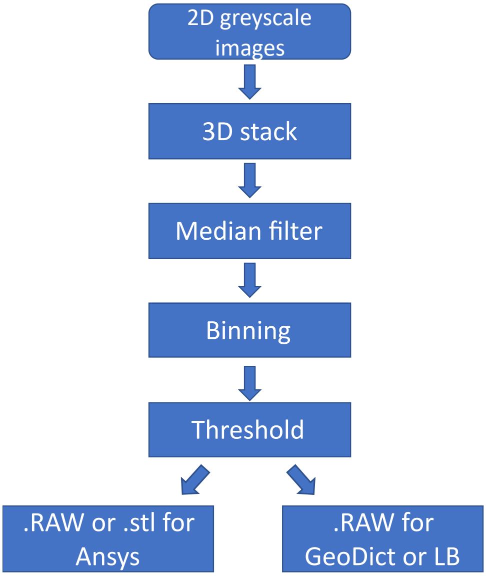

Figure 4.5: Image processing work-flow

4.3.1 Median Filter

The original greyscale images had some noise. As it can be seen from Figure 4.6 the images contained some circular lines, and salt and pepper noise. The median filter helps to remove such noise. It smooths the data while preserving the edges, and it is a non-error propagating method. The median filter works by replacing pixels values with the median value of all the pixels within a specified radius, which can be expressed as

$$\begin{aligned}&\text{Median filter}\\&=[\text{Replace pixels with the median value within the given radius}\\&\text{in dimension}\quad]\end{aligned}$$

The median filter removes both noise and fine details in an image. Any small area having different pixel values compared to a bigger neighbourhood would be filtered out. Thus, careful selection of the radius is necessary.

4.3.2 Binning Operation

Binning operation is required to reduce the file size without compromising on the details. This facilitates easier file handling and faster computation. Binning achieves a reduction

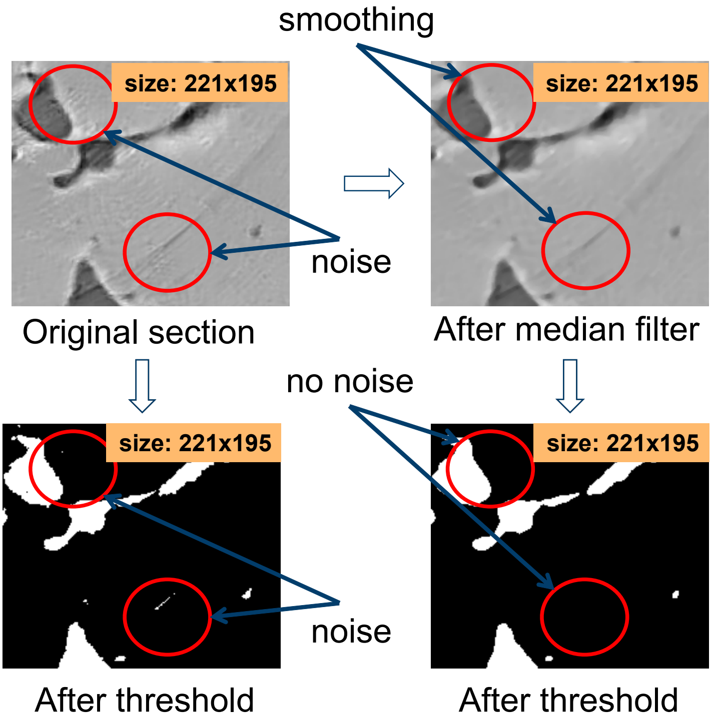

Figure 4.6: Top left: original section, Top right: median filter removes noise, Bottom left: Threshold applied without median filter contains noise, Bottom right: threshold applied after median filter produces a better-segmented image

in file size by replacing a given set of pixels or voxels with one pixel or voxel having the value equivalent to their 'sum', 'average', 'max', 'min', or 'median'. In this work, only average was used for binning to keep the image details useful for subsequent computation. A typical image stack of size 2GB to 10GB becomes within the range 200MB to 1GB after binning. How the file size is reduced can be understood from Figure 4.7. However, care should be taken as it will also cause some loss of details. If subsequent computation demands better spatial resolution binning may cause problems as original precision of the -CT images is reduced by the binning factor. For example, if some material features are smaller than the voxel resolution, those details would no longer be preserved after binning.

4.3.3 Threshold Operation

It is difficult to directly differentiate the pore space from the solid phase in the greyscale image. Sometimes it is also necessary to distinguish between multiple constituents of one material from its greyscale image. Segmentation or threshold operation makes it possible.

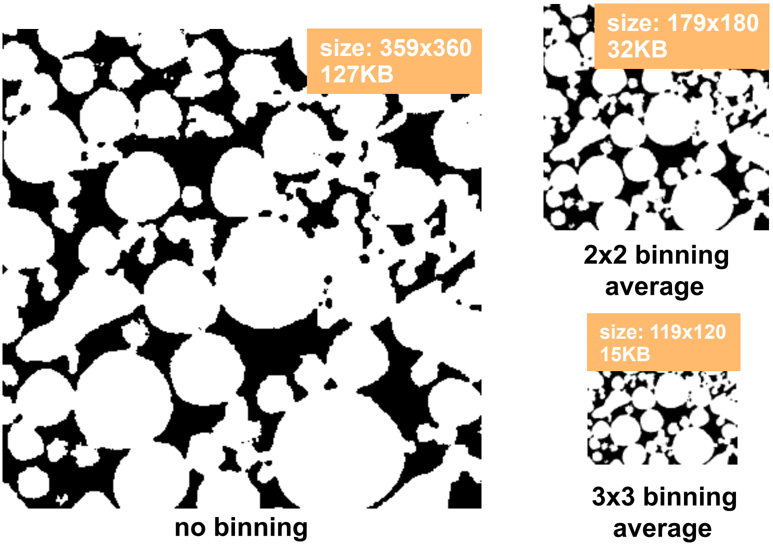

Figure 4.7: Binning reduces the size of the image by a factor of 4 (2x2 binning) or 9 (3x3 binning). In the figure the original image of size 127kB becomes 32kB and 15kB after 2x2 and 3x3 binning, respectively

For this thesis, only solid and void space separation is necessary, and hence only binary images are required. Based on a given threshold, each pixel in an image is either assigned a value 0 or 255 (for 8-bit binary-image) if the pixel intensity is lower or higher than the threshold. The choice of the threshold value can significantly influence how the solid and void phases are differentiated. The software ImageJ offers different algorithms to facilitate this. The isodata algorithm [173] was used in this work.

The idea of thresholding is briefly described here. To start the thresholding process, the image is first divided into object and background by assuming an initial threshold value. Following this, the averages of the pixels at or below the given threshold, and pixels above are taken. In the next step, an average of these two values are computed, and the threshold is incremented. The process is repeated until the threshold is larger than the composite average. Upon completion, the image is correctly segmented according to

4.3.4 Input Preprocessing

The images need to be saved in a format suitable for the simulation tools after segmentation. The procedure is described below:

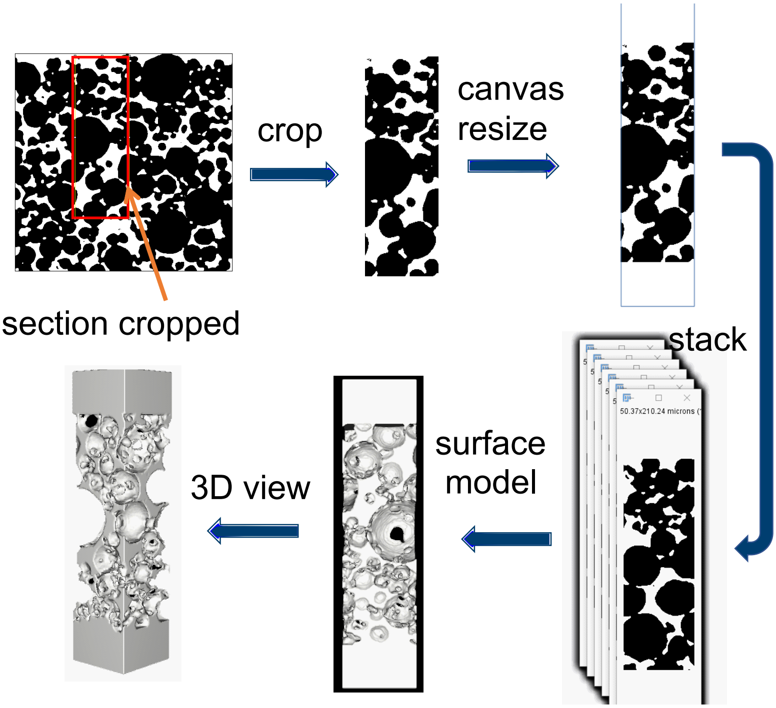

Figure 4.8: surface rendering of the 3-D volume is created from a stack of images after cropping, and canvas resize

- After segmentation, it should be ensured that the pore space is 0 and solid space is 1 for the maximal ball network extraction algorithm [71]. For the SNOW algorithm, the pore space should be marked as 1, and the solid space should be 0 [72].

- If the voxels are marked as 0s and 255s, the image stack should be divided by 255 to get 0s and 1s as values.

- The images need to be cropped so that the boundary surfaces are appropriately represented. This task was a bit tricky, but in general, an intuition-based method was employed here.

- If the image stack orientation is not aligned to the plane of the screen, a reorientation operation should be performed. The GeoDict preprocessor offers a built-in tool for this purpose.

- After realignment and cropping the stack was saved as a '.RAW' file. For this, a naming convention was followed. The file is saved as 'Samplename_lengthxheightxslices', e.g. Ti45C8 would be saved as Ti45C8_600x500x200. This information helps in future processing, and ImageJ detects the data from the filename. This data is further useful for Maximal Ball algorithm and SNOW algorithm.

- The above steps were sufficient for further working with OpenPNM or LB method. However, for GeoDict, the computational demand could be further reduced. A representative element volume (REV) was used. This REV was determined by gradually reducing (cropping) the volume of the 3-D stack while keeping the change in porosity within 3 %. The volume was not cropped in the thickness direction, as it might cause unwanted changes. As the cross-section is much larger than the thickness, only the cross-section should be cropped. After defining the REV, the file was saved in the same format as mentioned above.

- For running CFD simulation in ANSYS Fluent, the computational domain needed to be further reduced. A part having end-to-end pore connectivity with size less than 200x200x200 microns was selected for each sample based on trial and error method. The outlet and inlet portions were then extended using the ImageJ resize canvas option to avoid numerical instabilities or unnatural boundary conditions. This volume was then exported as a '.stl' file using the 3D viewer plugin in ImageJ. This plugin uses the marching cube algorithm to generate surfaces for volumetric data. The process flow is shown in Fig.4.8.

4.3.5 Network Extraction

The 3-D stack (.RAW file) produced after image processing is used for extracting pore network. There are many publications that have used pore network model. However, the source-codes are not publicly available for all of them. For flow simulation, some of the available tools are: pnflow [174, 175], OpenPNM [73], numSCAL_basic [176], starfish [177] etc. For extracting networks from 3-D reconstructed images, only two open-source tools are available to the best of our knowledge: Maximal Ball (MB) algorithm developed by Hu Dong [71, 178] and SNOW algorithm developed by Jeff Gostick [72]. These tools are regularly updated and maintained as repositories on GitHub. These two tools were used in this thesis. A brief description of how both these tools work is provided below. For more details, one should refer to the primary sources.

The MB network extraction code is written in C++ and is based on the concept of finding the maximal ball in a 3-D voxel space consisting of 0s and 1s, where 0s represent the void space and 1s represent the solid space. With respect to Figure 4.9, the process of finding pores and throats can be broken down to the following steps:

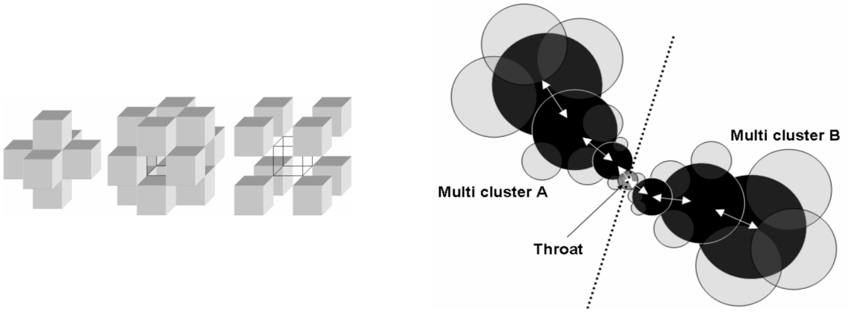

(a) **(b)**

Figure 4.9: Working of the maximal ball algorithm is shown in the figure. Reprinted figure with permission from Dong and Blunt, Phys.Rev.E 80, 036307, 2009, Copyright (2009) by the American Physical Society. https://dx.doi.org/10.1103/PhysRevE.80.036307. See [71, 178] a) Nearest neighbours are found in 26 directions b) Clustering of maximal balls to form pore-throat chains

i) In the void space, nearest neighbours are found in 6 lateral, 12 diagonal and 8 diametric directions. The MBs are the voxels that contain the largest sphere touching the solid surface so that no MB is a subset of another MB, i.e., each of the MBs has at least one voxel that is not part of another MB.

ii) In the next step, the MBs are clustered. Within a sphere having twice the MB radius, all other smaller balls touching the given ball are clustered as children that can have their own children.

iii) After the clustering, an MB with parents from different common ancestors is defined as throats while the ancestors are defined as pores. The inscribed radius of the ancestor MB is defined as pore radius, and the inscribed radius of the biggest throat MB in the pore-throat chain is defined as throat radius.

iv) The extracted pores and throats are defined as cylindrical capillaries based on a dimensionless shape factor G defined as

$$\frac{\quad}{\quad} \tag{4.1}$$

V is the volume of the pore or throat block based on the number of voxels. A is the surface area calculated from the number of surface voxels, and L is the length defined as twice the Euclidean distance from an ancestor ball's centre to the farthest voxel in that block.

The SNOW (subnet of the over segmented watershed) algorithm is a part of the porespy module written in python. This module can be imported to OpenPNM and applied to the 3-D image stack to extract network information. The porespy package is based on the image analysis packages scipy.ndimage and scikit-image. It provides a range of tools for extracting information from 3-D porous media. The SNOW algorithm is based on marker-based watershed segmentation. This procedure is based on the idea that the catchment basin represents a pore in a 3-D image on a contour map. The basic steps are summarised below:

i) A distance map is produced from the image. A Gaussian filter is applied to smooth the distance map and remove certain artefacts.

ii) The distance map of the void space produces peaks in locations that are furthest from the solid space. These peaks can be identified by applying a maximum filter with a given radius and finding the locations where the values in the filtered image are the same as the distance map.

iii) Some spurious peaks lying on the saddles and plateaus of distance maps are eliminated.

iv) Some peaks which are too close are also merged.

v) These peaks are supplied as markers to a marker-based watershed algorithm.

vi) Finally, relevant pore network details are extracted in a form suitable for OpenPNM.

vii) Upon identification of pore and throat regions, inscribed diameter of the pores and throats are described as the diameter of the pore body or throat that can be inscribed within that region. This is used as the default in the SNOW extraction algorithm. Another term equivalent diameter is also used. Equivalent diameter is the diameter of a circle having the same area as the pore or throat cross-section.

4.4 Mesh Generation

Constructing a good quality mesh is an essential part of running CFD simulation in any CFD software. This involves multiple steps in different tools and demands a fair amount of time. Figure 4.10 shows a detailed outline of the process employed for generating the meshes used in this work[3]. shows a detailed outline of the process employed for generating the meshes used in this work. The 3-D image stack is exported as a surface mesh using the 3-D viewer plugin in ImageJ. The surface mesh requires further simplification and

---

[3] This procedure was developed and refined by Deepjyoti Borah, Abhinav Hazarika [179], and Simson Rodrigues [180] for two master theses supervised under the PhD project

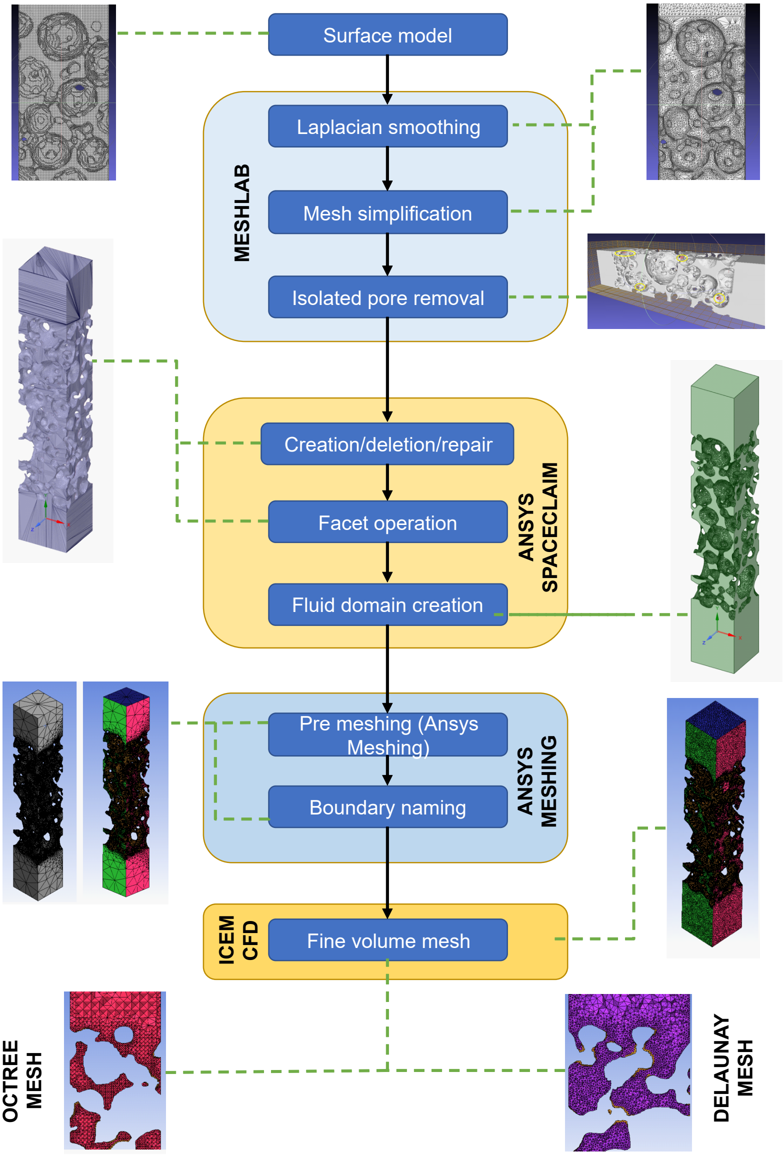

Figure 4.10: Sequence of processes in different tools for constructing CFD mesh on 3-D reconstructed PTL

smoothing to eliminate redundant details or noise that are not relevant to the physics of the problem. This step is carried out in Meshlab, an open-source software. It provides tools to simplify the surfaces by reducing the number of triangular surfaces while preserving the shape. Laplacian smoothing is used to smooth the surface mesh, and quadratic edge collapse decimation is used to reduce the number of faces while preserving the boundary and the normal. Since isolated pores do not contribute to the actual flow and may cause numerical problems, they are removed or converted to solid.

After processing in Meshlab, the surface mesh is opened in ANSYS Spaceclaim. ANSYS SpaceClaim offers different options for creation, deletion and repair of 3-D geometry. It also provides tools to work with surface models. In Spaceclaim intersecting faces, non-manifold edges and holes are repaired. Flat surfaces are created where necessary using facet operation, the surface model is converted to fluid domain, and inlet and outlet regions are extruded if required.

ANSYS meshing tool is employed to create a pre-mesh in the fluid domain. Due to the complicated structure of the porous medium, only unstructured mesh is created. The boundary surfaces are labelled, and a coarse volumetric mesh is created. This volumetric mesh is then imported to ICEM CFD to produce the final mesh suitable for running simulations. ICEM CFD is an industry-standard, versatile mesh generation and manipulation software.

Meshing process involves topology generation, global and part mesh setup. Topology generation displays a set of colour-coded curves that show how many surfaces they are connected to. Based on an analysis of this data, unwanted surfaces can be removed, or holes can be filled. Global mesh setup allows setting up general meshing parameters for the whole domain according to various meshers. Part mesh setup is utilized for defining part-specific meshing parameters like refinement for critical regions. For this work, all tri cells with patch independent method was used to create the surface mesh as it is suitable for low-quality geometry with poor connectivity [181]. After the surface mesh the volume mesh was created in two steps: Octree pre-mesh was followed by Quick Delaunay mesh. ICEM CFD provides different tools for checking mesh quality once the meshing process is complete. For this work, the orthogonal quality, skewness, aspect ratio, and volume change for the generated mesh were checked to ensure that they were within the acceptable range. Sometimes, few cells deviated from their ideal range, but it was ensured that they had no significant effect on the simulation.

4.5 Design of Test Cells

For this thesis, permeability was measured in two directions: through-plane and in-plane. For this purpose, two experimental cells were designed. The cells are described in the following two sections[4].

4.5.1 Through-plane Measurement Cell

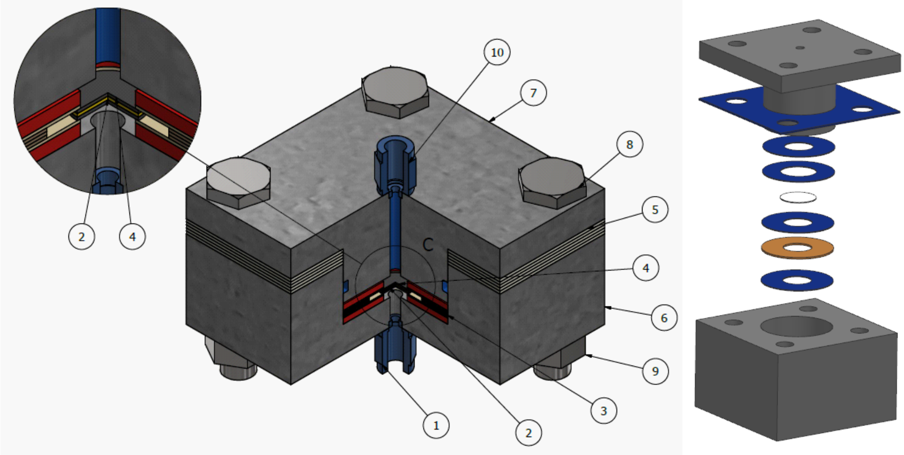

Figure 4.11: Test cell diagram for through-plane measurements [182]

Based on the Penn-state method, a test cell is constructed for circular PTL samples of size 20 mm in diameter. The cell design is depicted in Figure 4.11. It consists of an inlet ①, a pre-mixing section ②, a mixing section ③, and an end section ④. The PTL is placed between the mixing section and the end section. Gaskets ⑤ are used to prevent leakage. The bottom part ⑥ and the top part ⑦ are tightly fastened with the help of bolts ⑧ and nuts ⑨. The fluids enter through the inlet and moves out through the outlet ⑩. While measuring single-phase flow, only nitrogen is used as the working fluid. For two-phase flow, nitrogen and water are mixed at different ratios, and the mixing section is lined with rolled porous hydrophilic cloth to facilitate homogenous media distribution.

4.5.2 In-plane Measurement Cell

The test cell used for the measurement of in-plane permeability is shown in Figure 4.12. The construction of the cell is similar to the through-plane design (refer to Figure 4.11).

---

[4] The cells were designed by Nagadatta Madhu for a master thesis as a part of the PhD project

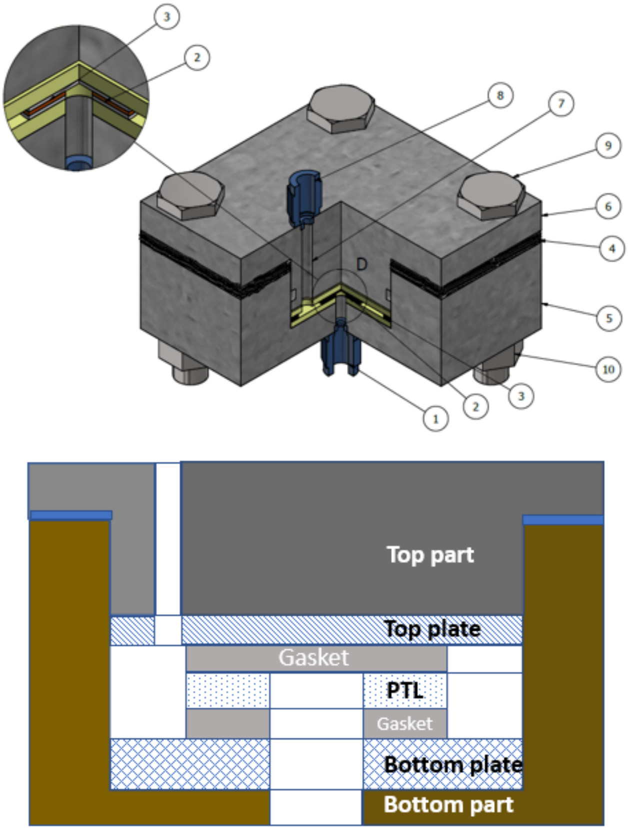

Figure 4.12: Test Cell diagram for in-plane measurements [182]

The difference exists in the way the flow outlet is constructed. As shown in the figure, the sample is placed between two gaskets with the same diameter as the test sample. The bottom gasket has a central hole with the same diameter as the test sample's inner diameter. The top gasket completely blocks the flow from going through the top surface of the cell. These three parts are held between two metallic plates. The bottom plate has a central hole with an inner diameter equal to that of the sample. The top plate has a hole outside the PTL's circumference aligned with another hole at the top part. This setup ensures that the incoming fluid moves radially outward in the in-plane direction. Gaskets can be used between the top and bottom parts to adjust the height.

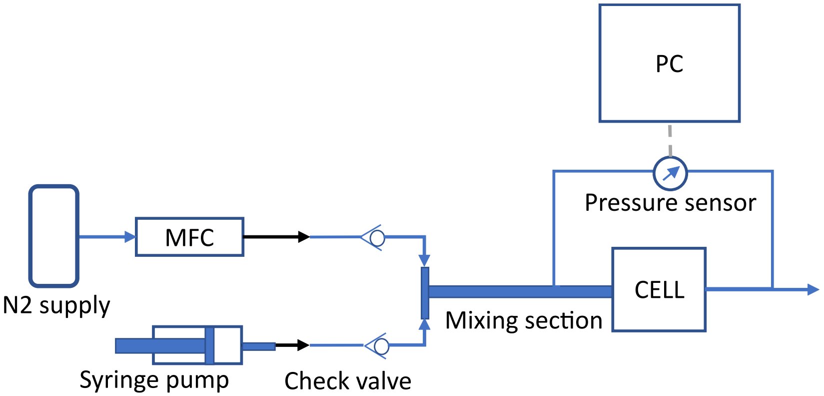

Figure 4.13: A schematic diagram of the experimental setup

4.5.3 Experimental Setup

The schematic diagram of the experimental system is shown in Fig. 4.13. Although the cell designs are different, the general system layout is the same. Nitrogen gas is supplied from the lab supply lines through a Brooks Instruments Mass Flow Controller (MFC type 5850 E Series). Depending upon the requirement, an MFC with different capacity can also be used. The MFC is controlled by Brooks Instruments readout and control electronics which has input supply voltage of 0-5 V and output supply voltage set to ±15 V. The water is supplied using a KD Scientific multi-syringe pump. The pump can deliver from nanoliter range to 120 ml/min. When a continuous low volume supply of water is required, this is replaced by a membrane pump. The output from both pumps go through two non-return valves and enters a T-joint. There a premixing section is created to facilitate a homogeneous gas-water mixture. A given length of the plastic inlet tube is lined with porous hydrophilic cloth to achieve this. Inside the cell, two small porous plastic layers are placed before and after the PTL to minimize end-effect hysteresis [22, 25, 164]. Pressure transducers from WIKA are used for the measurements of pressure difference across the PTL. Transducers having a range from 500 mbar to 2500 mbar are used for this work. Voltacraft PPS DC power supply is used for supplying power to the transducers. The transducers have non-linearity in the range of 0.2 % of the displayed reading and non-repeatability of 0.1 % of the displayed reading. For the experimental setup, a National Instruments USB-6008/6009 device is used as the data acquisition device. A USB interface (3.4 and 3.5) connects the device to the PC, where the LabView software is configured for pressure measurement. When a new pressure transducer is used, this needs to be reconfigured.

The ex-situ measurement of relative permeability depends on the gravimetric method for saturation determination. For measuring the weight of the PTLs, a scientific analytical balance from Sartorius GmbH (Model LP-220S, 220 g, readability 0.1 mg, deviation 0.1 mg) is used.

It should be noted that only one supply line for gas or water is used for single-phase flow measurement, and no premixing or mixing section is necessary. Single-phase flow measurement is straight forward and less time-consuming. But the attainment of steady-state in two-phase flow is a time-consuming process. Moreover, the gravimetric determination of water saturation involves potential errors.

4.6 Permeability Measurement

Absolute and relative permeability are two essential parameters for the characterization of the PTLs. For the calculation of relative permeability, the absolute permeability must be measured correctly. In the next sections, the procedure for the same is described.

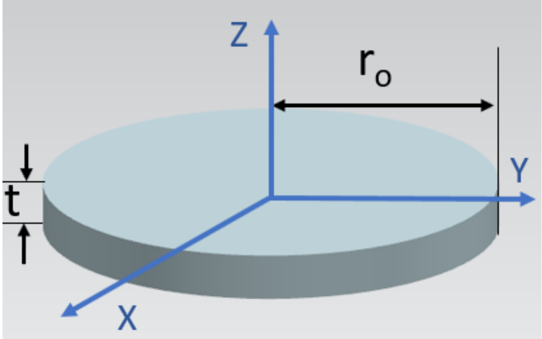

(a) Through-plane Sample

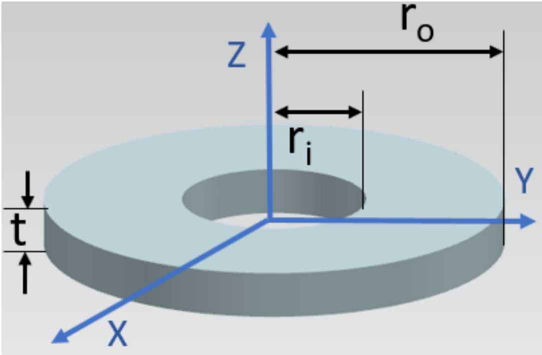

(b) In-plane Sample

Figure 4.14: Description of the test samples

4.6.1 Absolute Permeability Measurement

The method of absolute permeability measurement is derived from Darcy's law. If a fluid having dynamic viscosity with a flow rate produces a pressure drop for a PTL having a flow cross-section and thickness , then absolute permeability can be calculated from the following equation

$$\frac{\quad}{\quad} \tag{4.2}$$

However, it is important to note that this law is valid only for laminar flow with very small velocity. The flow in porous media can be divided into two zones, namely Darcy and non-Darcy flow. Until a specific limit, the flow rate and pressure relationship would be linear for the porous material. This zone is the Darcy flow zone. Beyond this, the flow behaviour changes, the stokes flow assumption of Navier-Stokes equations will no longer hold, and turbulence effects may become visible. This happens when Reynold's number is Re > 10. For this work, the experiments are carried out within the limits of the Darcy zone. For non-Darcy flow, it is necessary to add inertial coefficient or Forchheimer term into the calculation.

4.6.1.1 Expression for Through-plane Permeability

While measuring the absolute permeability of the PTL samples using nitrogen, the gas compressibility can be incorporated into the calculation following a simple modification. This method is adopted from Gostick et al., [23] and Geertsma [183]. The derivation of the modified form of Equation 4.2 is outlined in the following steps:

With reference to the left diagram of Figure 4.14 and assuming that the flow is happening along the z-direction, Darcy equation can be written as,

$$\frac{\quad}{\quad} \quad \frac{\quad}{\quad} \tag{4.3}$$

where represents the superficial velocity. For a given mass flow rate , the following equation holds

$$\tag{4.4}$$

where is the area of the sample. From the ideal gas equation, the expression for the density of nitrogen can be written as

$$_{2} \quad \frac{\quad_{2}}{\quad} \tag{4.5}$$

Using Equation 4.3 and Equation 4.5 continuity equation can be reformulated as

$$\left(\frac{\qquad}{\qquad}^{2}\right)\left(\frac{}{}\frac{}{}\right) \tag{4.6}$$

Now, this equation can be rearranged and integrated along the flow direction

$$\frac{\qquad}{\qquad}^{2}\int \qquad\qquad \int \tag{4.7}$$

where and are the pressure values at the inlet and the outlet respectively. The integration yields

$$\frac{\qquad}{\qquad}^{2}\frac{\quad}{\quad}\frac{\qquad\qquad}{\qquad\qquad} \tag{4.8}$$

The expression for can be evaluated for the outlet conditions. Then the resultant equation can be rearranged to derive the expression for through-plane permeability

$$\frac{\qquad\qquad}{\qquad\qquad} \tag{4.9}$$

4.6.1.2 Expression for In-plane Permeability

The samples' in-plane permeability is measured by allowing the fluid to enter the sample at the centre and then forcing the flow to go in the radially outward direction. Thus, the conventional flow cross-section cannot be used to calculate the permeability directly from Darcy's equation. This method is borrowed from Feser et al. [24] and Dwenger [25]. With reference to the right diagram of Figure 4.14, for the flow in a radially outward direction, Darcy's equation can be written as

$$-\frac{\quad}{\quad} \tag{4.10}$$

Using equations 4.5 and 4.10, continuity equation can be written as

$$\frac{\qquad}{\qquad}^{2}\frac{}{}\frac{\quad}{\quad} \tag{4.11}$$

which can be further simplified as

$$\frac{\quad}{\quad} \tag{4.12}$$

Upon integration and application of pressure boundary condition, the following can be derived

$$(\qquad\qquad)\left(\quad -\right) \tag{4.13}$$

Now, it is possible to write

(4.14)

Considering the flow at the outlet to be and using Equation 4.14 to compute permeability the following equation can be obtained

(4.15)

4.6.1.3 Absolute Permeability Measurement Procedure

The following steps are performed for the measurement of absolute permeability:

1. Effective flow cross-section is determined by measuring the sample dimension and the gasket dimensions.
2. The cell is checked for leakage.
3. When no leakage is detected, the reference pressure is noted.
4. The PTL sample is placed inside the cell and checked for leakage
5. Nitrogen gas is allowed to flow through the sample, and pressure drop is recorded at steady state.
6. The above process is repeated until a sufficient number of data points are obtained for different flow rates.
7. From the measured data points, absolute permeability is then calculated.

4.6.2 Measurement of Relative Permeability

When more than one fluids are present, the effective permeability of an individual phase changes. The concept of relative permeability helps to determine the effective permeability of the given phase as a function of the saturation of another phase present in the system. Typically, the wetting phase is considered as the reference whose saturation is used for deriving relative permeability. Application of Darcy's law to a gas-liquid two-phase system results in the following equations for relative permeability

(4.16)

(4.17)

where the subscripts and refer to the liquid phase and the gas phase, respectively. Since the porous medium's absolute permeability is theoretically independent of the fluid, it stays the same for both the equations.

4.6.2.1 Measurement Methods

The experimental methods for the determination of relative permeability are classified into two categories

(i) steady-state method

(ii) unsteady-state method.

In the steady-state method, both the fluids are simultaneously injected to the test sample at constant flow rates. This process is carried out until a steady-state is reached. A constant pressure drop indicates attainment of steady-state over time. The flow rate into and out of the sample also remains the same. When a steady state is reached, the flow rates are changed, and the process is continued until the next steady state is reached. For each steady-state, the flow rates and pressure drop are recorded, and the saturation inside the sample is measured.

The unsteady method is based on the drainage of one fluid by the other fluid in the porous material. Here, the relative permeability is measured as a function of the ratio of the fluids going out of the system. This method is quicker and allows for choosing flow conditions similar to actual real-time data. There are different ways to calculate relative permeability by the unsteady method like Buckley-Leverett frontal advance equation [184] or Johnson, Bossler and Neumann (JBN) method [161, 162, 185] or variations of the same. Different researchers have also found good agreement between steady and unsteady methods [186]. The unsteady method's difficulty lies in the fact that the pressure difference between the phases must be maintained for finding precise flow rate at the outlets. Moreover, this involves uncertainties, and the computation process is complicated. Although unsteady method takes less time, typically steady-state method is preferred due to its higher accuracy [185].

An important factor in the measurement of relative permeability is determining the fluid's saturation in the porous material. There are two ways to resolve this. One is the ex-situ method, where the sample needs to be taken out of the test cell to perform the measurement. In the in-situ method, the saturation is determined while the cell is in operation. Ex-situ method would employ gravimetric measurement of the saturation. There are different ways to determine saturation in the in-situ method. When the material properties permit the electric resistivity method can be used to do this. Nuclear magnetic resonance or CT-imaging using X-ray or neutron beam can also be used to determine saturation. These methods provide better accuracy, but they require dedicated experimental facilities, require more time and economic resources. The porous titanium samples used in this thesis are not suitable for electric resistivity based measurements. Therefore, the gravimetric method was chosen for the measurements even though it is prone to errors.

When the JBN method or any modified version of the JBN method is used, it is assumed that the flow occurs at sufficiently high velocities to rule out any capillary effects. The flow is also incompressible and immiscible. The overall operating pressure must be much larger than the pressure difference across the sample; the driving force and the fluid properties are unchanged during the test. Flow velocity is assumed constant across the whole area of the sample. The JBN equation defines individual phase permeabilities as follows [162]:

$$\left[\left(\frac{\quad}{\quad} \right) \left(\frac{}{} \right) \right] \tag{4.18}$$

$$\frac{\quad}{\quad} \tag{4.19}$$

In the equation and are the relative permeabilities [%] of the liquid and the gas respectively; is the dynamic viscosity of the liquid, is the dynamic viscosity of the gas, is the liquid fraction [%] at the outlet, is the gas fraction [%] at the outlet, is the cumulative injection to the pore volume, and is the relative injectivity. Relative injectivity is defined as the ratio of injectivity to the initial injectivity, i.e.

$$\frac{\qquad}{\qquad} \tag{4.20}$$

where is the liquid injection rate, and is the pressure drop across the sample.

4.6.2.2 Relative Permeability Measurement Procedure

This thesis employs the steady-state method for the experimental determination of relative permeability. The steady-state method assumes that both the phases have the same pressure drop, and there is no saturation gradient across the sample [186, 187].

The following steps are performed for the ex-situ measurement of relative permeability of the PTL samples:

1. The effective flow-cross-section ( ) and thickness ( ) are determined from the PTL and cell dimensions. Dry weight ( ) and porosity ( )of the sample are measured and recorded.
2. The cell is checked for leakage, and reference pressure is recorded for dry nitrogen gas. This needs to be subtracted from the measured pressure later to determine the pressure drop due to the PTL alone.
3. Now the PTL sample is placed in the cell and ensured that no leakage exists.
4. A given gas-water ratio is selected and allowed to pass through the sample.
5. The pressure drop across the cell is carefully observed. When it remains unchanged or changes very little over a time period, the pressure value is recorded, and the sample is taken out of the cell.
6. The sample is carefully taken out of the cell. The weight due to liquid saturation ( ) is measured by using a precision balance. The saturation is determined by using the following equation
   $$\frac{\qquad}{\quad_{2}} \tag{4.21}$$
7. The sample is put back into the test cell. The gas-water ratio is now changed, and the process is repeated until a sufficient number of data points are obtained.
8. The data points are used to calculate saturation and effective permeability of the phases.

4.7 Summary

In this chapter, different computational and experimental methods relevant to this thesis are described. The necessary preprocessing steps to prepare inputs for different computational methods are explained. Image processing plays an essential role in the preprocessing part, and all the steps involved are shown with flow-charts. An overview of the computational tools and different available options therein are also given. The details of the experimental test cells are provided. After describing the test cells, the relevant expressions for calculating absolute and relative permeability are derived, and the measurement procedure is described in detail.

Chapter 5

Experimental Characterization of Porous Transport Layers

5.1 Description of Test Samples

Absolute and relative permeabilities of six different PTLs fabricated in FZJ were measured. The test samples were made from sintered titanium powder. The samples were sintered from spherical particles of diameter 45 microns (Ti45) and formless particles (HDH) respectively. The samples were classified as given below

- 20 mm through-plane samples
- 20 mm in-plane samples
- 5 mm through-plane samples

The sample details can be understood from the name of the samples. For example, sample Ti45-500-800-IEK-07 can be understood as follows:

Ti45 - Particle type
500 - Nominal thickness in micron
800 - Sinter temperature in °C
IEK-07 - Sample lot

The porosities of the samples were measured using two methods. The first method relied on sample volume and dry weight.The second method utilises pascals law to find the solid matrix volume by determining the weight loss inside a fluid of known density. The sample volume is known from the dimensions. When the sample has volume and dry weight

, then based on density of titanium , the first method gives porosity

$$\frac{}{} \tag{5.1}$$

In the second method, if the density of isopropyl alcohol (IPA) is and the weight of the sample inside IPA is , then porosity from the second method is given by

$$\frac{}{} \tag{5.2}$$

Table 5.1: Details of 20 mm diameter through-plane samples

Sample Name	Code	Diameter (mm)	Thickness (mm)	Porosity (%)
Ti45-500-800-IEK-07	IEK07A	20.00	0.567	34.4 (35.1)
Ti45-500-800-IEK-08	IEK08A	20.00	0.507	28.6 (29.4)
Ti45-500-850-IEK-90	IEK90A	20.00	0.499	26.6 (27.1)
Ti45-500-850-IEK-91	IEK91A	20.01	0.499	26.1 (25.6)
HDH-150-1000-IEK-41	IEK41A	19.91	0.153	36.0 (38.8)
HDH-400-1000-IEK-44	IEK44A	20.00	0.387	33.5 (34.8)

Table 5.2: Details of 20 mm diameter in-plane samples

Sample Name	Code	Outer Diameter (mm)	Inner Diameter (mm)	Thickness (mm)	Porosity (%)
Ti45-500-800-IEK-07	IEK07B	20.02	4.94	0.560	34.2 (35.2)
Ti45-500-800-IEK-08	IEK08B	19.99	4.94	0.507	28.5 (28.6)
Ti45-500-850-IEK-90	IEK90B	20.00	4.97	0.505	28.0 (28.9)
Ti45-500-850-IEK-91	IEK91B	20.02	4.96	0.507	27.4 (27.2)
HDH-150-1000-IEK-41	IEK41B	19.96	4.84	0.170	34.9 (38.2)
HDH-400-1000-IEK-44	IEK44B	19.96	4.94	0.390	33.9 (33.7)

The geometric dimension and porosity of the samples are described in tables 5.1, 5.2 and 5.3. The values inside small brackets indicate porosity determined by the second method. Precision machining was used to cut the samples to their desired dimensions. Each sample's diameter was measured using a digital vernier, and the thickness was measured using a micrometer. However, it should be noted that the machining process left slightly rougher edges of the samples. For the 20 mm diameter through-plane samples, measuring thickness

Table 5.3: Detail of 5 mm diameter through-plane samples

Sample Name	Sample Code	Outer Diameter (mm)	Thickness (mm)	Porosity (%)
Ti45-500-800-IEK-07	IEK07C1	5.04	0.560	34.6 (31.5)
Ti45-500-800-IEK-07	IEK07C2	5.04	0.560	34.9 (31.4)
Ti45-500-800-IEK-08	IEK08C1	5.00	0.507	28.5 (22.9)
Ti45-500-800-IEK-08	IEK08C2	5.03	0.507	29.4 (23.8)
Ti45-500-850-IEK-90	IEK90C1	5.04	0.499	27.2 (22.9)
Ti45-500-850-IEK-90	IEK90C2	5.03	0.499	27.4 (22.8)
Ti45-500-850-IEK-91	IEK91C1	5.04	0.499	26.4 (10.1)
Ti45-500-850-IEK-91	IEK91C2	5.04	0.499	26.5 (16.7)
HDH-150-1000-IEK-41	IEK41C1	4.95	0.154	32.7 (35.3)
HDH-150-1000-IEK-41	IEK41C2	4.98	0.154	33.4 (35.6)
HDH-400-1000-IEK-44	IEK44C1	5.01	0.387	33.0 (32.9)
HDH-400-1000-IEK-44	IEK44C2	5.02	0.387	33.4 (33.4)

was not a problem as enough flat surfaces were available. While measuring the thickness of 20 mm in-plane and 5 mm through-plane samples, the rough edges made it difficult to place the micrometer surfaces. This influence was particularly evident for the 5 mm diameter samples. Therefore, the thickness values from the through-plane 20 mm diameter sample were used to calculate these samples' porosity.

In Figure 5.1 porosity values of different samples are shown. It is observed that for the dry-weight based porosity determination, the samples from the lot IEK41 differ the most. For the buoyancy based method, the samples from the lot IEK91 differ the most. This discrepancy can be explained by taking a look at Table 5.3. It shows that very low porosity was recorded for the 5mm samples. One can infer that either these samples had a higher percentage of closed pores or water could not fully saturate the material. One possible cause could be surface contamination during the handling of the samples.

Figure 5.2 shows the average porosities of the samples from each lot and their corresponding standard deviations. The porosity values obtained from the dry weight method for the lots IEK07, IEK08, IEK90, IEK91, IEK41 and IEK44 are 0.345, 0.288, 0.273, 0.266, 0.343 and 0.334 respectively. Among these, the lot IEK41 has the highest standard deviation of ±0.015. The standard deviations for the other samples are negligible. Similarly the porosity values from the buoyancy based method are 0.333, 0.262, 0.254, 0.199, 0.356 and 0.334 respectively. The two lots IEK91 and IEK08 have the highest standard deviations of

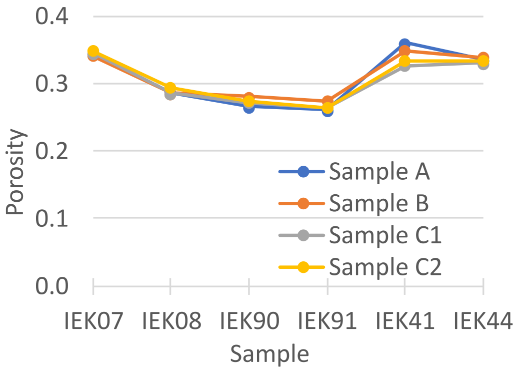

(a) Dry weight-based

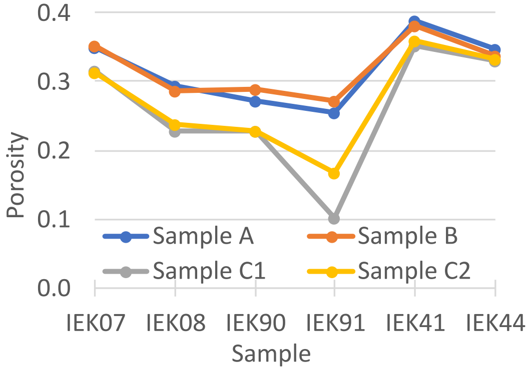

(b) Buoyancy-based

Figure 5.1: Porosities of the samples based on dry weight and buoyancy method

and respectively. The deviation of the sample IEK91 occurs due to the very low porosity determined by the buoyancy based method for the 5 mm diameter samples, as shown in Table 5.3.

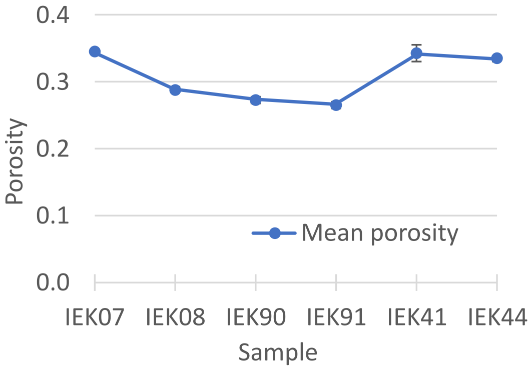

(a) Dry weight-based

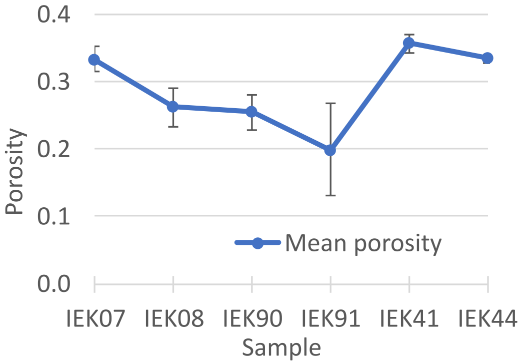

(b) Buoyancy-based

Figure 5.2: Average porosity of the test samples and their standard deviation

5.2 Absolute Permeability of the Porous Transport Layers

The absolute permeability of the samples described above was measured using cell designs as discussed in the previous chapter (refer Section 4.5) using the methods in Section 4.6. The measurements were carried out for both through-plane and in-plane permeability of the PTL samples. [1]

5.2.1 Through-plane Permeability

In the through-plane configuration, the test cell was supplied with nitrogen gas from 50 ml/min to 500 ml/min in steps of 50 ml and pressure drop was measured. It was ensured

---

[1] Preliminary measurements for absolute and relative permeability of the 20 mm diamter samples were carried out by Nagadatta Madhu for a master thesis as part of the PhD project [182].

that the pressure for a given flow rate stays stable. Then the permeability is calculated by two methods. The first is based on a simple Darcy equation, without taking gas compression into account given by Equation 4.2. The second method takes into account the effect of gas compression as shown by Equation 4.9, which upon modification becomes

$$\frac{\qquad}{\qquad} \tag{5.3}$$

Both equations can be plotted in a velocity-viscosity term versus pressure gradient plot, the slope of which provides the value of absolute permeability. The uncertainty in the slope can be calculated using the LINEST function in MS Excel.

The permeability values measured using the through-plane experimental cell design are listed in Table 5.4. The curves for the measurement are shown in Figure 5.3. It can be seen that the lines corresponding to the samples IEK08A, IEK90A, IEK91A, IEK44 have the y-intercept value one order of magnitude smaller than one unit of the y-axis. These lines show minimal deviation from the origin. Ideally all curves would pass through the origin, but IEK41 and IEK07 show large deviations. The pressure-time data for these two samples show that significant pressure drop was not achieved to distinguish different experimental points (refer Section B.1). The plots also show that the gas compressibility effects within the experimental range are negligible as demonstrated by the measured values using both Equation 4.2 and Equation 5.3. The permeability values measured using Equation 5.3 are displayed in Table 5.5.

Table 5.4: Through-plane permeability of PTL samples using equation 4.2

Sample Code	Permeability (mD)	Permeability repeated (mD)	Deviation (%)
IEK07A	280.00 3.54	–	–
IEK08A	72.12 0.69	78.25 0.53	+8.50
IEK90A	77.03 0.37	84.90 0.72	+10.21
IEK91A	72.31 0.65	77.42 0.47	+7.01
IEK41A	163.45 5.59	–	–
IEK44A	119.83 2.16	101.27 0.83	-15.49

5.2.2 Repeatability of Through-plane measurement

For the experimental results, it is also vital that the results are repeatable. Therefore, the permeability tests were repeated for four samples out of the six mentioned in the previous section. The samples IEK07 and IEK41 were not repeated due to specific reasons

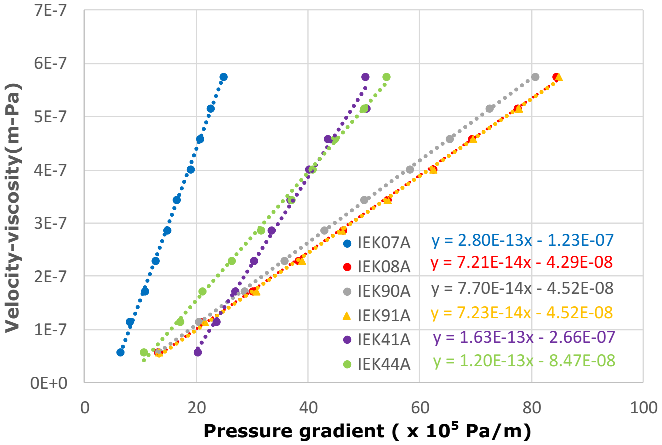

(a) Using equation 4.2

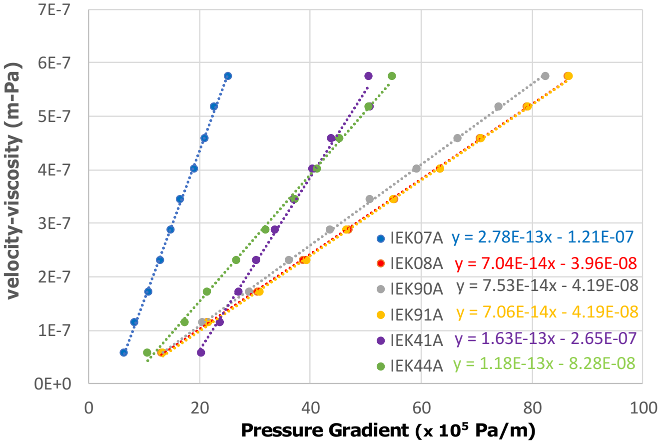

(b) Using equation 5.3

Figure 5.3: Through-plane permeability determination by velocity-viscosity versus pressure gradient plot using two different equations. The curves show that both equations produce nearly identical values. That means gas compressibility effects are negligible

Table 5.5: Through-plane permeability of PTL samples using equation 5.3

Sample Code	Permeability (mD)		Permeability repeated (mD)		Deviation (%)
IEK07A	277.6	3.47	–		–
IEK08A	70.40	0.56	76.51	0.44	+8.68
IEK90A	75.29	0.41	83.17	0.63	+10.47
IEK91A	70.60	0.54	75.68	0.47	+7.20
IEK41A	162.56	5.58	–		–
IEK44A	118.36	2.06	99.83	0.84	-15.66

that would be discussed in the next section. In Figure 5.4 the curves for the repeated experiments are shown next to the first measurements' curves for each of the samples. The figure shows that that results do not differ much, which is also visible from the data presented in Table 5.5.

5.2.3 Analysis of Through-plane Measurement Data

The plots for permeability and pressure against Reynold's number are shown in Figure 5.5a and Figure 5.5b respectively, and pressure versus flow rate plots are shown in Figure 5.5c. It should be noted that for the calculation of Reynold's number two methods were considered, one based on median pores diameter of the samples and the other based on the specific surface area. For this purpose, 3-dimensional computer tomography data was used. However, both the methods yielded similar range of Reynold's numbers. The equations for both the methods are mentioned below [40, 188]

$$\frac{\quad}{\quad} \tag{5.4}$$

$$\frac{\quad}{\quad} \tag{5.5}$$

where is the median pore diameter, and is the characteristic length equivalent to the reciprocal of specific surface area, all other notations have their usual meanings. In this thesis, the second equation is used to plot the experimental data.

The plots for pressure display linear change in pressure with respect to flow rate, which means that Darcy law should be valid and inertial effects are negligible. However, a closer inspection of permeability values for the samples IEK07 and IEK41 reveals that the permeability values increase with increasing Reynold's number for all the experimental points. For the other samples, permeability values show significantly less deviation with respect to Reynold's number. A look at the pressure-time plots for the samples IEK07 and IEK41 in Appendix B reveals that the pressure drops for these two samples were very small, and very close to the experimental error. Thus errors in the results for those two samples can be suspected. These two samples, being highly permeable, were beyond the limits of the experimental setup. Some authors have mentioned, low permeability porous media and highly viscous fluid, about pre-Darcy flow characterized by 'greater than proportional increase' in the velocity of the fluid for a given pressure gradient [189]. But our experimental data rule out such a possibility.

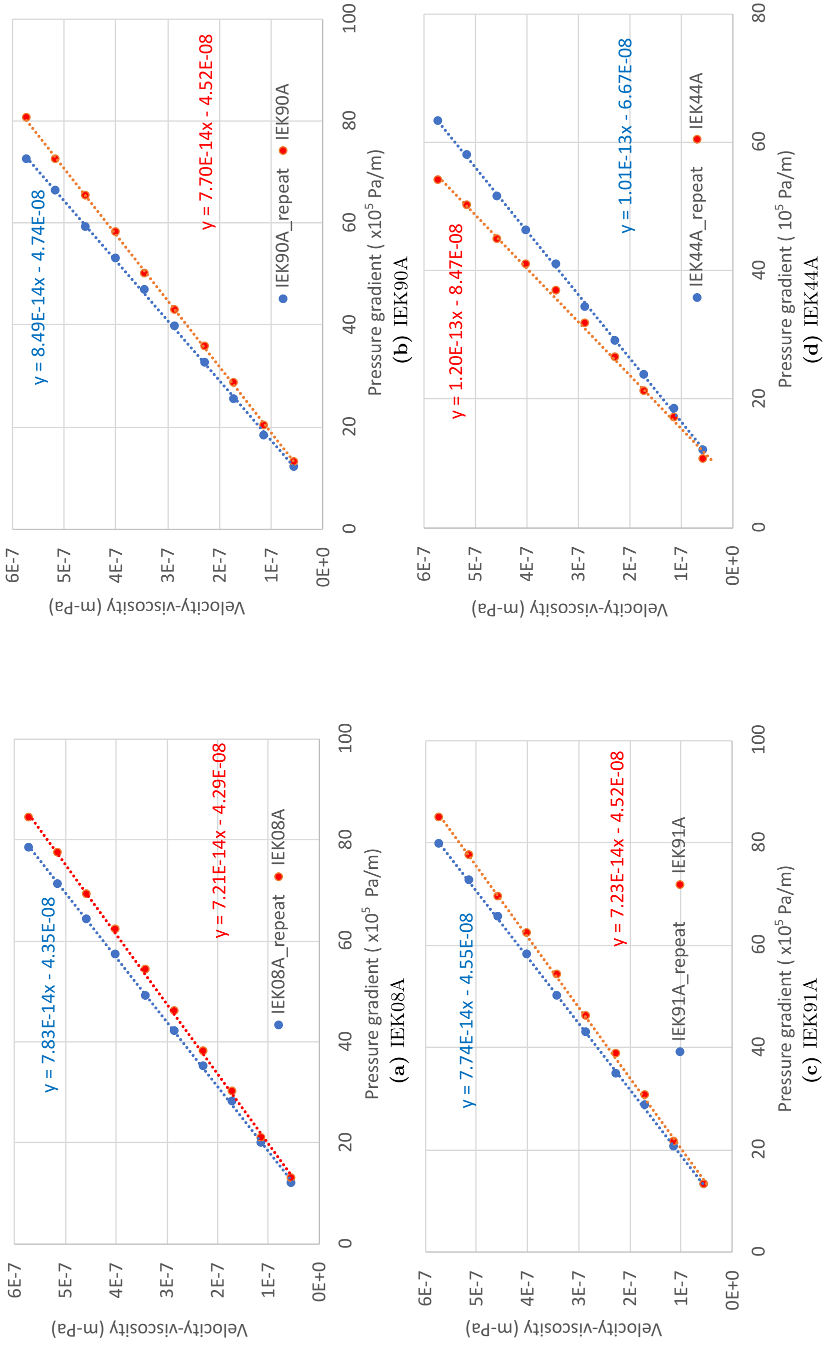

(a) IEK08A

(b) IEK90A

(c) IEK91A

(d) IEK44A

Figure 5.4: Repeatability of through-plane permeability measurement

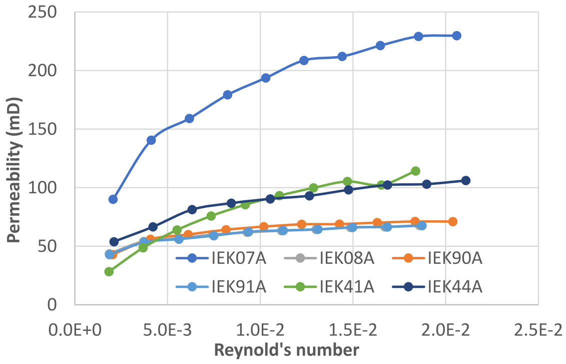

(a) K-Re plot

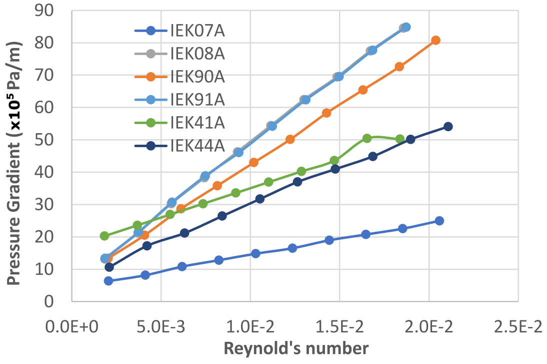

(b) Pressure-Re plot

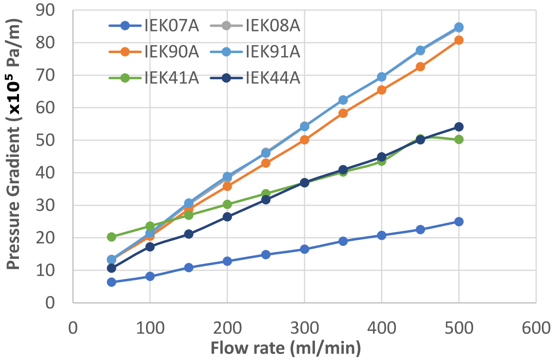

(c) Pressure-flow rate plot

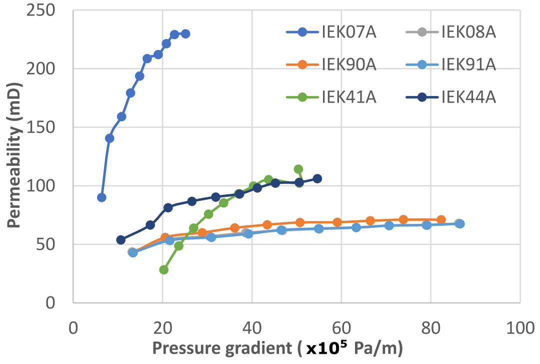

(d) Permeability-pressure gradient plot

Figure 5.5: Analysis of permeability data for through-plane samples

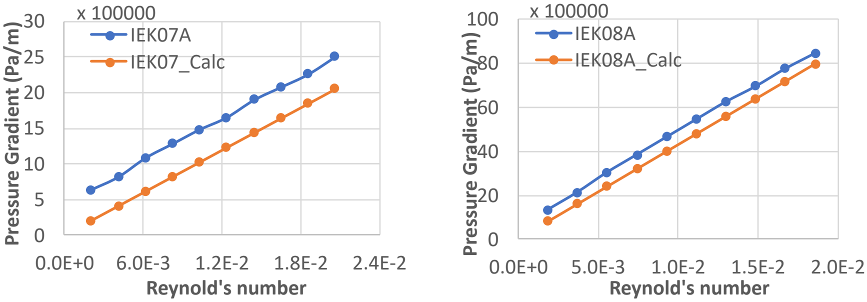

(a) IEK07A **(b)** IEK08A

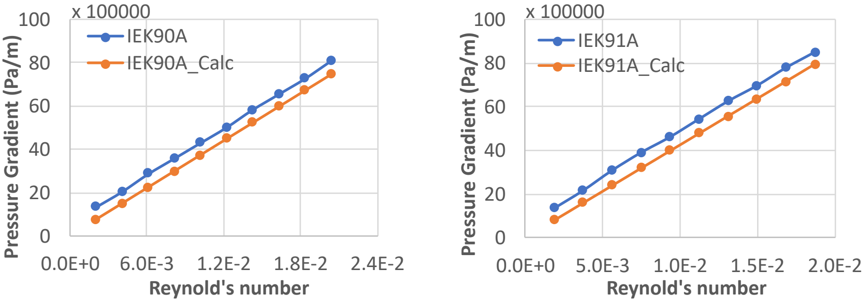

(c) IEK90A **(d)** IEK91A

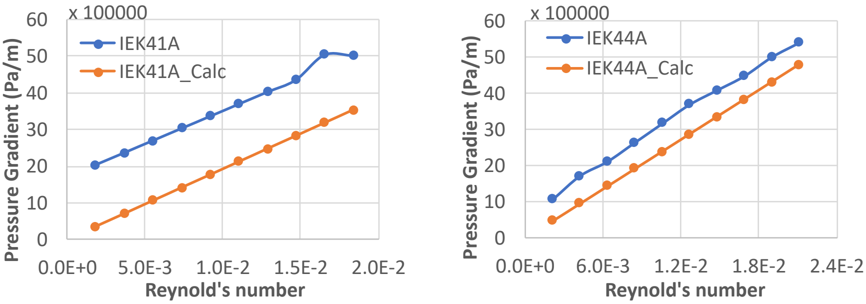

(e) IEK41A **(f)** IEK44A

Figure 5.6: Comparison between experimentally measured pressure gradient and pressure gradient back calculated from permeability values

In Figure 5.6, the pressure gradients back-calculated (using simple Darcy equation) from the measured permeability values are compared against experimentally measured values. The gap between the two lines for each sample represents the deviation of the velocity-viscosity vs pressure gradient plots from the origin. Also, from these plots, it can be confirmed that the two samples IEK07 and IEK41 have larger errors.

5.2.4 In-plane Permeability Measurement

In-plane permeability values of the samples were measured using the in-plane test cell described in Section 4.5 in Figure 4.12. The tests were performed for flow rates varying between 0-50 ml/min. For each flow configuration, stable pressure was recorded, which was then used as input to calculate in-plane permeability using Equation 4.15. This equation was modified to a form such that the slope of a straight line fitted through the measurement points will yield a given sample's permeability. The rearranged equation takes the following form:

$$\frac{\quad}{\quad} \quad \frac{\qquad\qquad}{\left(-\right)} \tag{5.6}$$

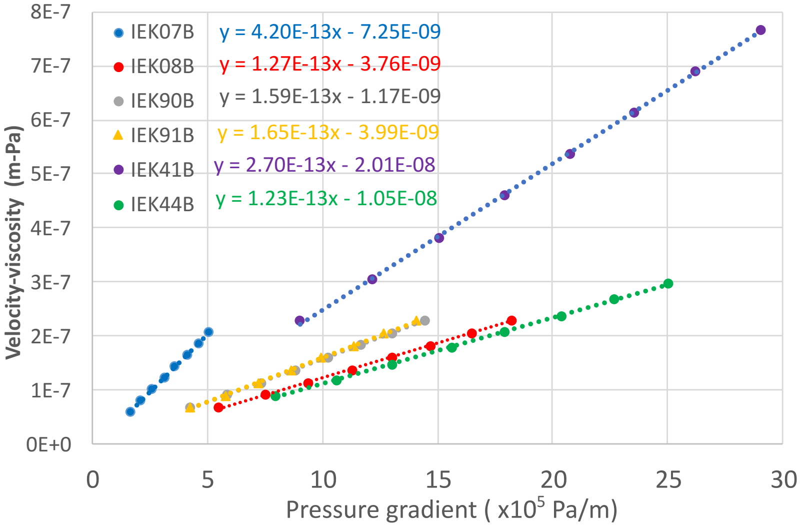

Figure 5.7: In-plane permeability measurement of 20 mm diameter samples

The permeability values for the samples IEK07B, IEK08B, IEK90B, IEK91B, IEK41B, and IEK44B are tabulated in Table 5.6, and the respective curves are shown in Figure 5.7. The curves are linear, and the intercepts do not deviate much from the origin.

Table 5.6: In-plane permeability of PTL samples

Sample Code	Permeability (mD)	Permeability repeated (mD)	Deviation (%)
IEK07B	419.91 3.32	–	–
IEK08B	127.22 1.50	113.35 0.75	-10.90
IEK90B	159.43 1.36	129.29 0.80	-18.90
IEK91B	165.16 0.87	130.82 1.19	-20.79
IEK41B	269.91 2.44	–	–
IEK44B	122.94 1.01	142.12 1.15	+15.60

5.2.5 Repeatability of In-plane Permeability

In-plane permeability measurements were repeated for four of the six samples, and the plots for each of them are shown in Figure 5.8. The data on Table 5.6 shows that the deviation between the measurements is within 20%.

5.2.6 Analysis of In-plane Permeability Data

Permeability v/s Reynold's number, pressure v/s Reynold's number, pressure v/s flow, and permeability v/s pressure gradient relationships are analysed for the in-plane samples like Section 5.2.3. The corresponding plots are displayed in Figure 5.9. The sample IEK07B shows that the permeability value keeps increasing with Reynold's number, while for the other samples, it becomes almost constant (even though there is some small increase). This behaviour is also evident from the analysis of the permeability-pressure gradient relationship. The curves also confirm that the flow occurs within the Darcy zone, and inertial effects can be neglected. The pressure-time data in Appendix B shows that the measurement error is negligible as all the samples show distinguishable pressure gap between measurement points.

5.2.7 Uncertainty of Absolute Permeability Measurement

Method of propagation of uncertainty was applied to calculate the uncertainties associated with the individual measurements. When is a function of variables with individual uncertainties, then the uncertainty of can be approximated as [22]

$$\left[\frac{}{}\ {}_1\right] \quad \left[\frac{}{}\ {}_2\right] \quad \left[\frac{}{}\right] \tag{5.7}$$

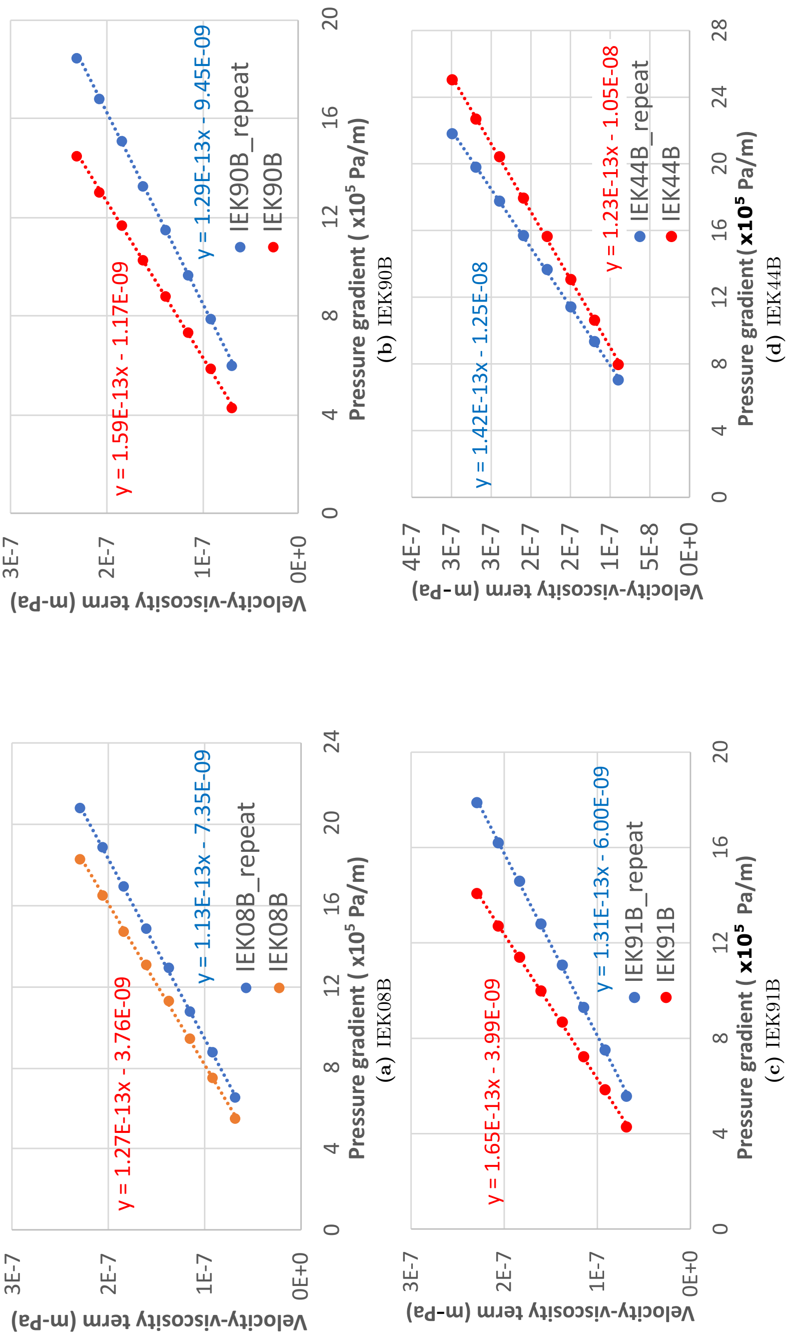

(a) IEK08B

(b) IEK90B

(c) IEK91B

(d) IEK44B

Figure 5.8: Repeatability of in-plane absolute permeability

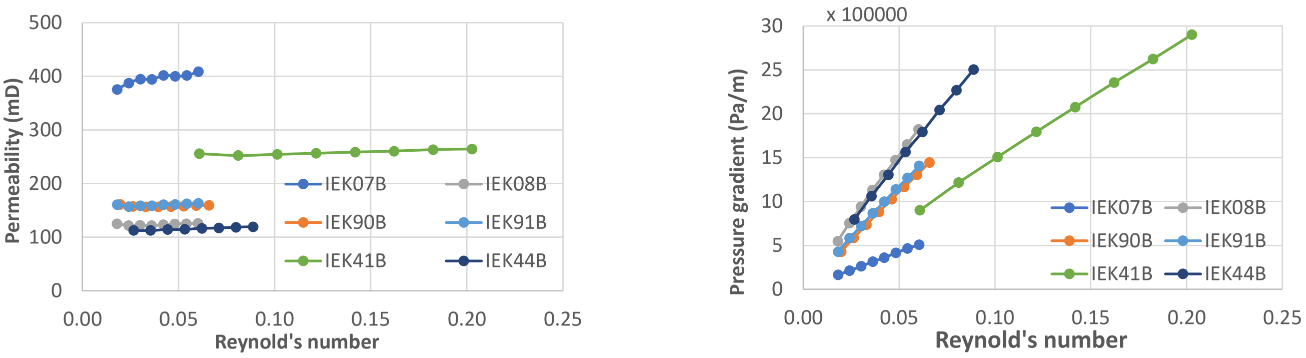

(a) K-Re plot

(b) Pressure-Re plot

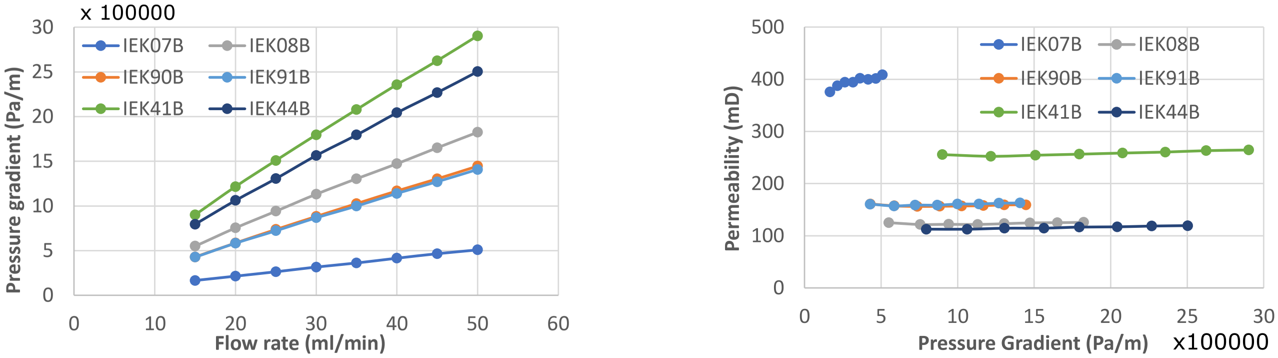

(c) Pressure-flow rate plot

(d) Permeability-pressure gradient plot

Figure 5.9: Analysis of permeability data for in-plane samples

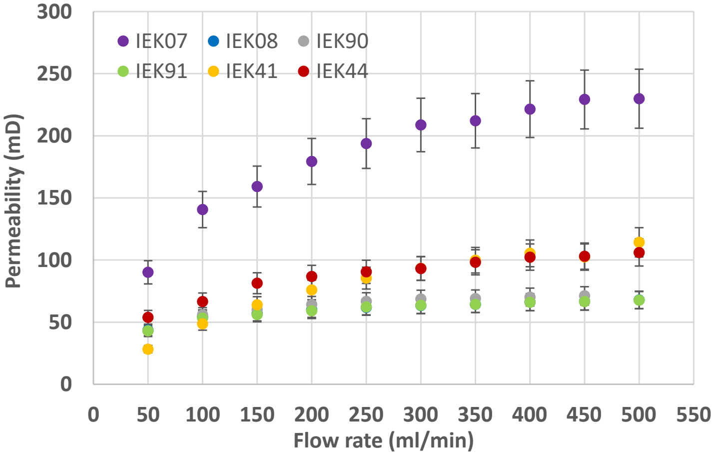

(a) Throuh-plane measurement

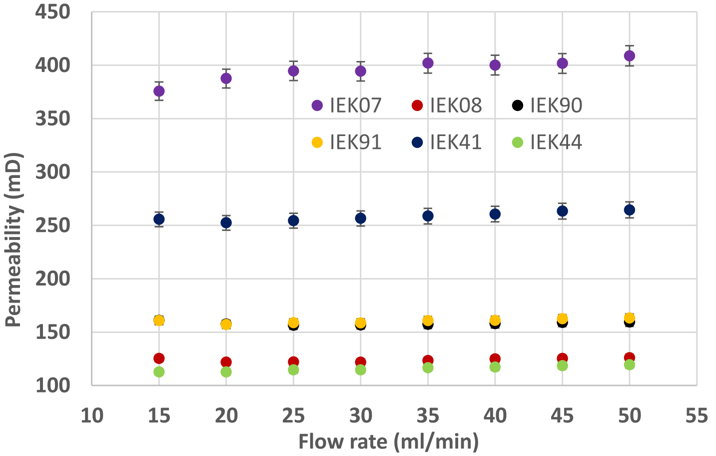

(b) In-plane measurement

Figure 5.10: Uncertainty of through-plane and in-plane absolute permeability measurements. Uncertainty of individual data points are shown in figure. Through-plane measurements show higher uncertainty than in-plane measurements

Table 5.7: Uncertainties associated with absolute permeability measurement

Quantity	Units	Value	Remark
	ml	1 % I.V.	specification
	mm	0.01	measured
	mm	5 %	assumed
	mbar	1 % I.V.	specification
	mm	0.01	measured
	mm	0.04	measured

This procedure was applied to Equation 4.2 to obtain the following expression for the uncertainty of thorugh-plane permeability

$$\begin{gathered}\left[\frac{}{}\right] \quad \left[\frac{}{}\right] \\ \left[\frac{}{}\right] \quad \left[\frac{}{} \quad \right]\end{gathered} \tag{5.8}$$

Similarly, from Equation 4.15, the following expression for uncertainty associated with in-plane permeability can be obtained

$$\begin{gathered}\left[\frac{}{}\frac{}{} \quad \right] \quad \left[\frac{}{}\frac{}{(\quad)} \quad \right] \\ \left[\frac{}{}\frac{}{} \quad \right] \quad \left[\frac{}{}\frac{}{} \quad \right] \\ \left[\frac{}{}\frac{}{(\quad)} \quad \right]\end{gathered} \tag{5.9}$$

In the above equations , , , refer to the uncertainties associated with the mass flow rate, sample thickness, gasket diameter, and pressure transducer measurement respectively. Similarly and refer to uncertainty in the measurement of inner and outer diameter of the in-plane samples. Uncertainty of inlet pressure measurement for the in-plane samples is represented by . The uncertainty values are shown in Table 5.7. In the table, the gasket diameter change with respect to the fastening torque of the through-plane cell is assumed to be 5 %.

Figure 5.10 shows uncertainty associated with each measurement point of both in-plane and through-plane permeability measurement. From the analysis it was found that the gasket diameter was the most significant factor in through-plane measurement, and all the samples had uncertainty within 10-11 %. In the in-plane measurement none of the factors were predominant and all the samples had uncertainty less than 3 %.

5.3 Relative Permeability of Porous Transport Layers

Relative permeability of the 20 mm diameter PTL samples were measured following the procedure described in Section 4.6.2.2. The same cell as that for the measurement of absolute permeability was used. Each sample was measured multiple times. Some measurements were discarded as no definite pattern could be observed. The rest are presented in Figure 5.11, Figure 5.12, and Figure 5.13. Exponential trendlines were plotted for all the measurement sets.

5.3.1 Analysis of Relative Permeability Measurement

The plots in Figure 5.11, Figure 5.12, and Figure 5.13 show that different sets of measurements for the same material differ from one another. Only two samples, namely IEK90 and IEK44, show close clustering of measurement points from the trendline for different runs. However, the general trend looks similar to typical relative permeability curves. There exists no benchmark data to compare these results. Similar measurements for gas diffusion layer of PEM fuel cells have been reported by Nguyen et al., Sole, Hussaini and Wang, and Ramos-alvarado et al. [20–22, 163, 164]. These authors have measured two-phase flow properties for different GDL materials produced from carbon with and without hydrophobic treatment (refer to Section 3.2). Their results would not be directly comparable to PEM electrolyser PTL measurements. However, they can offer a general reference for the measured values. On comparison, it was found that our measurements conform to those in literature [20]. It should be noted that the handling of the sample for each measurement point involves a certain amount of error that cannot be quantified. Lack of statistical significance in the measurement of relative permeability using the gravimetric method to determine liquid saturation has been mentioned in the literature [25].

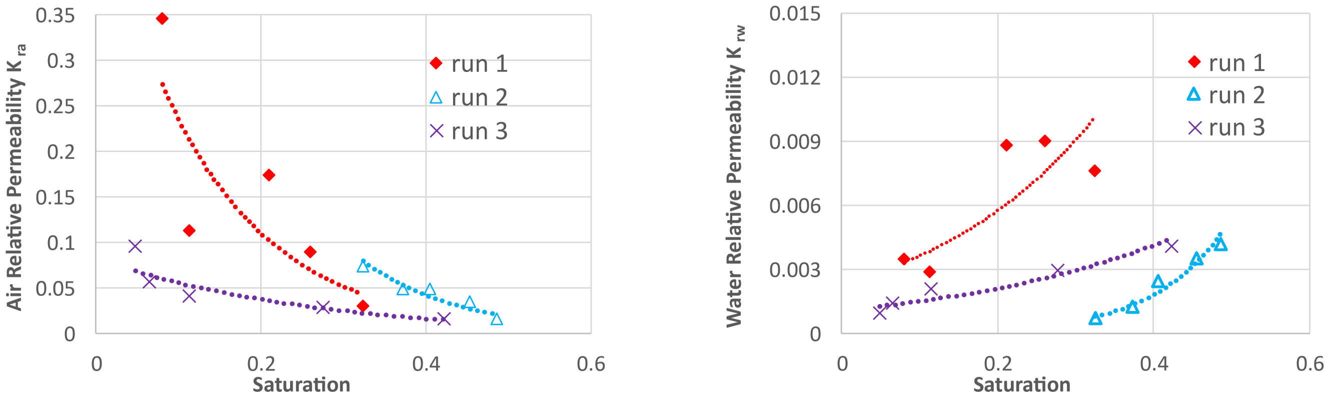

(a) IEK07

(b) IEK07

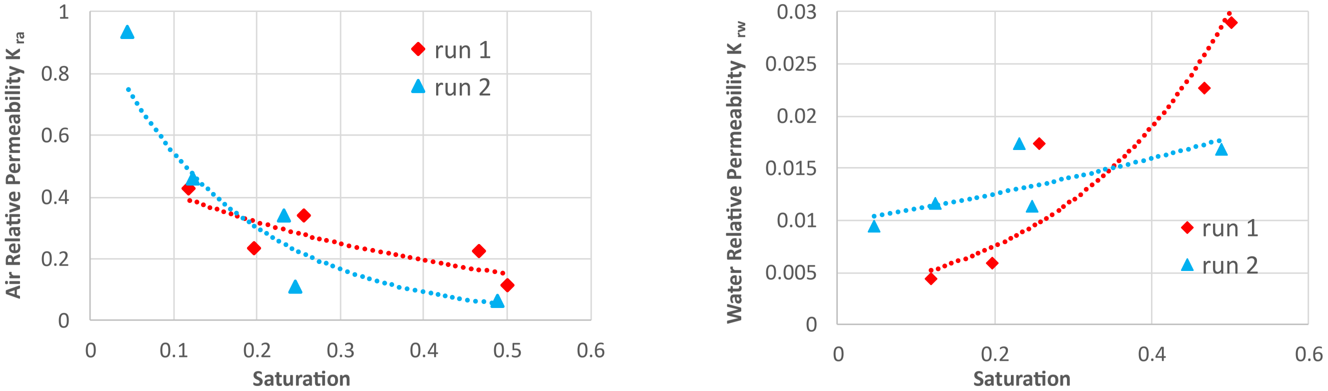

(c) IEK08

(d) IEK08

Figure 5.11: Relative permeability of IEK07 and IEK08

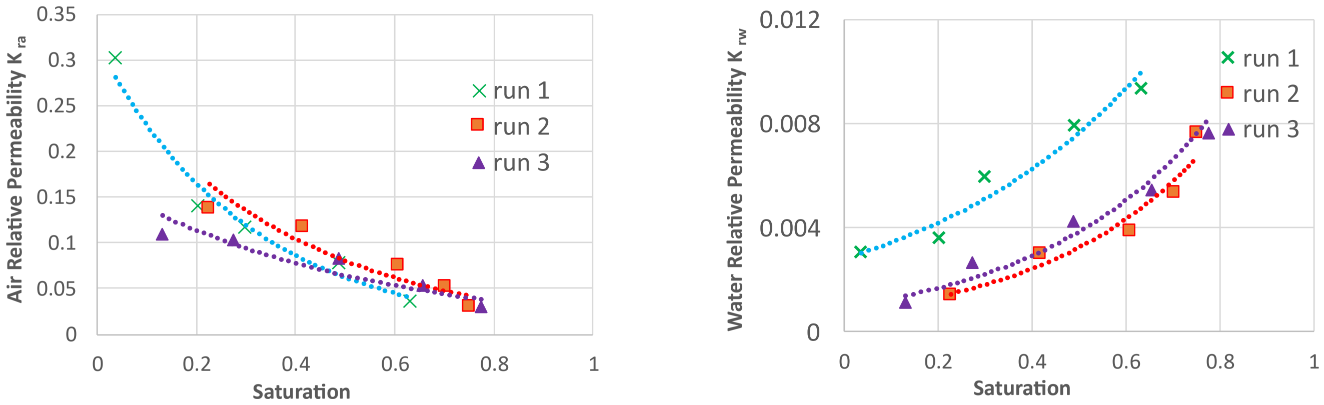

(a) IEK90 **(b)** IEK90

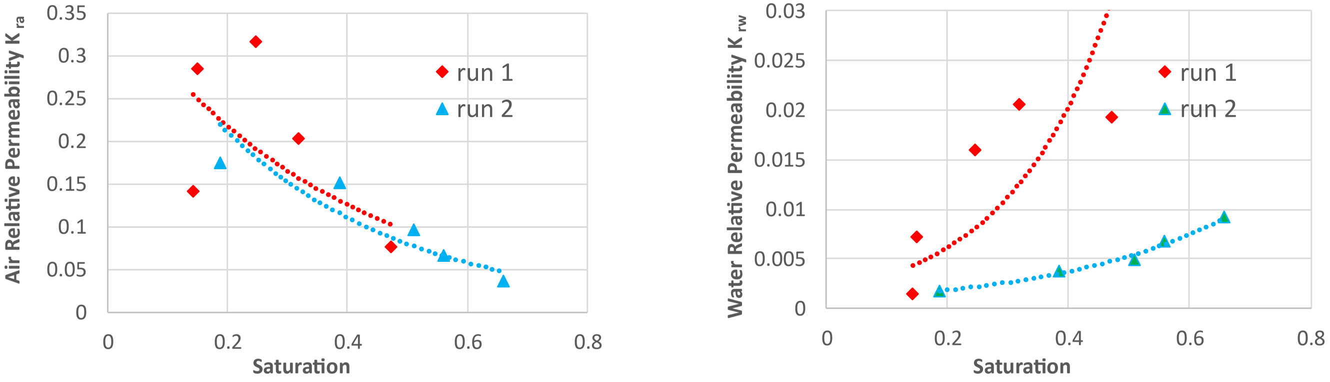

(c) IEK91 **(d)** IEK91

Figure 5.12: Relative permeability of IEK90 and IEK91

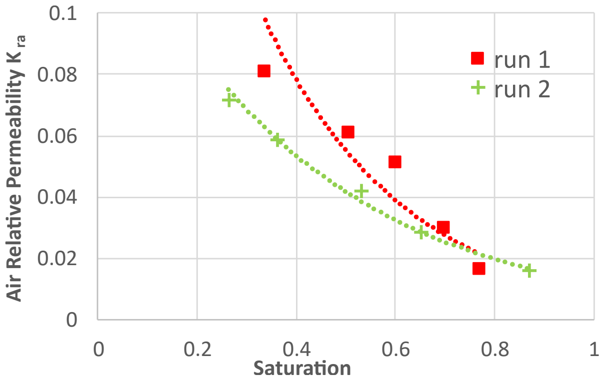

(a) IEK44

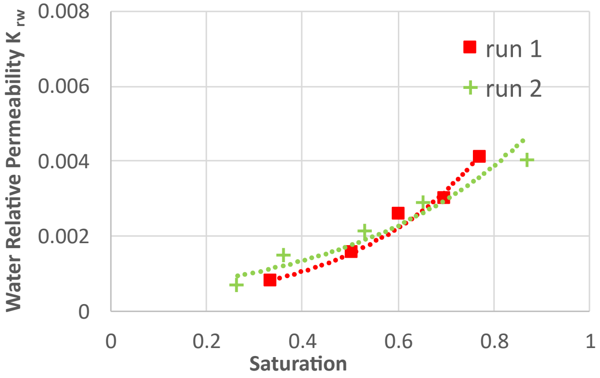

(b) IEK44

Figure 5.13: Relative permeability of IEK44

5.4 Summary

In this chapter, the experimental measurement of the PTLs was discussed. First, the dimensions and physical parameters of the test samples were measured. After that, for the 20 mm diameter PTL samples, both through-plane and in-plane permeabilities were determined. For both cases, repeatability of the measurements was checked. In the through-plane measurements, the samples IEK07 and IEK41 showed larger error as the pressure drop was not significant enough for the calculations. Relative permeability could be measured only in the through-plane direction. In-plane relative permeability could not be determined as proper equilibrium could not be achieved due to a design flaw and handling error. Accumulation of bubbles in the annular space between the PTL and cell body prevented proper control of the test setting. The relative permeability measurements showed agreement with similar results in literature.

Chapter 6

Numerical Characterization of Porous Transport Layers

The last chapter discussed experimental characterization of PTLs. Experimental characterization is important for proper understanding of material behaviour. However, it poses challenges in terms of resources and time required. Therefore, computational methods play an important role as an additional tool in the process. As part of this thesis, different computational methods were considered to determine their agreement or disagreement with the experimental results. These methods are discussed in detail in chapter 2 and chapter 4.

6.1 Flow Simulation with Pore Network Model

Pore network model is widely used in the petroleum industry for modelling flow processes inside of rocks. This work attempts to use the same methods for studying the flow inside the sintered titanium PTLs used in PEM electrolysers. The pore structure influences the flow behaviour. The pore structure is dependent on the material and the processes involved during the manufacturing of the PTLs. Therefore, some simplified model must be used to identify the effect of different structural parameters which can then be applied to more general PTL materials. For this purpose, first, artificial networks are created based on parameters from actual material upon which single and two-phase flow simulations are subsequently performed. Sensitivity to different structural parameters is also studied. After that, the same simulations are performed on networks extracted from actual materials to see if the same correlations hold.

6.1.1 Flow Simulation on Artificial Pore Networks

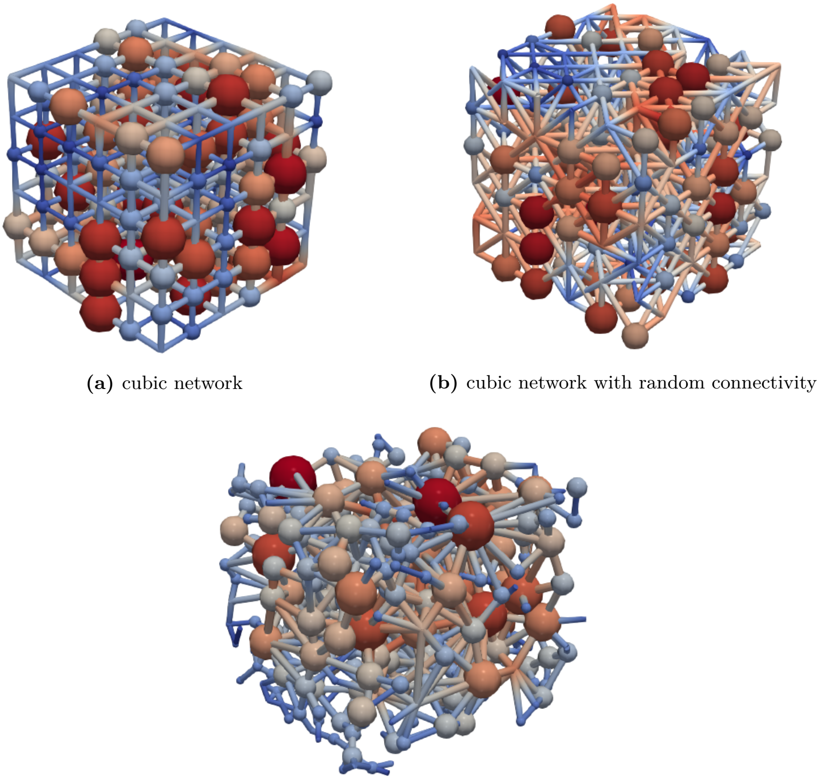

(a) cubic network **(b)** cubic network with random connectivity

(c) extracted network

Figure 6.1: Different pore networks are shown: a) regular cubic network with connectivity 6 b) a cubic network with a random connectivity 7.5 c) network extracted from CT-images using the maximal ball algorithm

There exist different methods to construct artificial pore networks. Some common methods are cubic lattice, Voronoi tessellation, and Delaunay tessellation. A simple cubic lattice is easy to construct and allows reasonable control over the parameters for a sensitivity study. In a simple cubic lattice, the pores are placed at the corners of a rectangular grid, and each internal pore has six neighbours. Thus, the default connectivity is six. The throats lie along the edges of the rectangular lattice units. This simple cubic lattice can be modified such that each pore has random connectivity, and the network has a desired average connectivity. For this purpose, a cubic network can be constructed such that each internal pore can have a maximum of 26 throats (considering all the edges and diagonals connecting the immediate neighbours). After that, some of the throats can be randomly removed to obtain a desired average connectivity. In Figure 6.1, three different networks

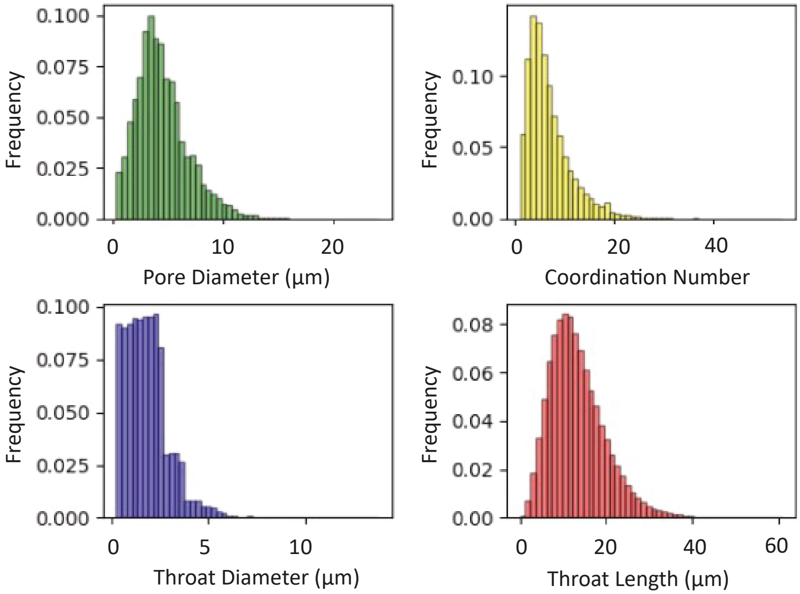

Figure 6.2: Size distribution of the network extracted from Ti45C8 using the maximal ball algorithm shown as a fraction of the total in each category.

are shown. The first one is a simple cubic, the second one is a cubic network with random connectivity of 7.5, and the third one is a network extracted from the 3-D stack of a real material using the maximal ball algorithm. It is visible that the network extracted from a real material has pores and throats organized in a more haphazard manner than a regular lattice.

Table 6.1: Reference dimensions of Ti45C8 network extracted using the maximal ball algorithm

Material	Ti45C8
Average coordination number	7
Average pore diameter (µm)	4.11E-6
Average throat diameter (µm)	1.76E-6
Average throat length (µm)	3.65E-6
Thickness (µm)	250

For constructing a simple artificial network, reference dimensions are chosen from one of the in-house materials. The material Ti45C8 is sintered from titanium powder of size 45 µm. The histograms corresponding to pore diameter, throat diameter, throat length and coordination number of the same material extracted by the maximal ball algorithm [71] is shown in Figure 6.2. The relevant information for this material are listed in Table 6.1.

6.1.1.1 Effect of Network Size on Computed Quantities

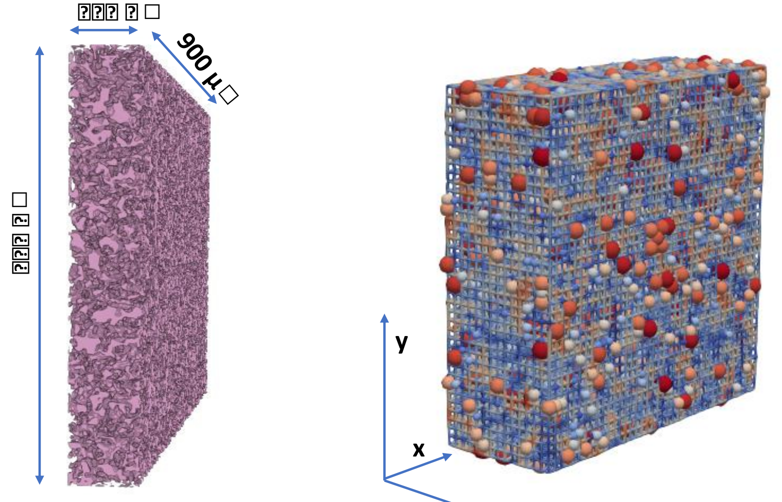

(a) PTL section

(b) a cubic network

Figure 6.3: Typical dimensions of a PTL section used for network extraction and a cubic network are shown. a) The thickness of the material is the limiting dimension here b) A cubic network with 15 layers along the thickness (z) direction and 100 layers along the cross-section. The thickness can be controlled by the lattice spacing

Natural rocks or porous materials typically have dimensions ranging from a few centimetres to meters. But PTLs used in PEM electrolysis generally are less than a millimetre in thickness. Therefore, the effect of domain size on the computed or measured values cannot be ignored. When one uses an artificial or extracted network, such effects also need to be studied. For this purpose cubic networks were created using dimensions mentioned above as reference. The details of the created networks are mentioned in Table 6.2. On these networks permeability was calculated using stokes flow simulation based on Hagen-Poiseuille equation for modelling flow through porous media. To investigate the effect of network size on the computed parameters, a square PTL cross-section is considered. A ‘layer’ in a given direction means the number of lattice points along that direction. The thickness of the material being the limiting factor, only up to 25 layers have been considered in that direction. For the simulations, two types of cubic networks were used:

Table 6.2: Details of the cubic network used to study the effects of domain size on computed parameters

Network	Cubic
Lattice spacing (mm)	0.000015
Pore and throat size distribution	Stick-n-Ball Weibull/Normal distribution
No. of layers along the thickness	10, 20, 25
Cros-section	Square
Layers along cross-section	10, 20, 40, 60, 80, 100, 140, 200

- For the first kind, a **stick-n-ball** model was used. This in-built model in OpenPNM assumes spherical pores and cylindrical throats. This model assigns the pore diameters from a normal distribution such that the mean value is equal to half of the lattice spacing. The throat-diameter between two pores is set to half the diameter of the smaller pore.

- For the second type of network, the pore structure is defined using Weibull distribution. The boundary pores and throats are defined using a normal distribution having a relatively smaller size. The resultant distribution is shown in Figure 6.4. A comparison with Figure 6.2 reveals that this is closer to the pore size distribution in an actual material.

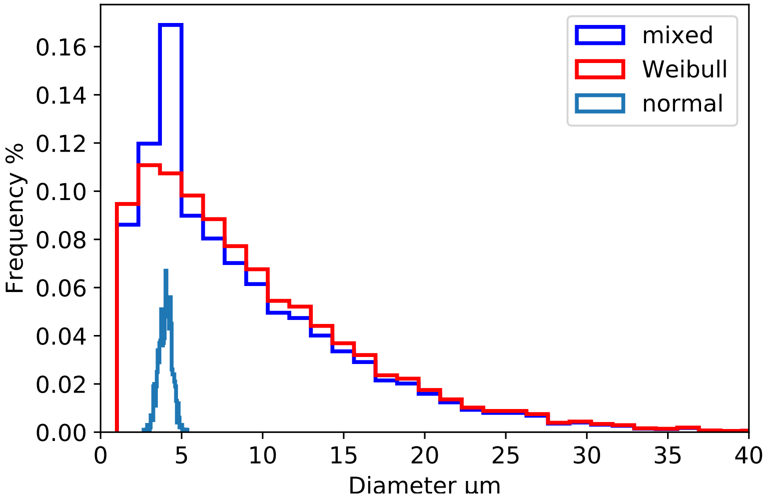

Figure 6.4: Pore size distribution of a typical cubic network with both Weibull and normal distribution. Parameters used for the normal distribution: mean=0.000004, scale=0.0000004; parameters used for the Weibull distribution: shape=1.2, scale=.000009

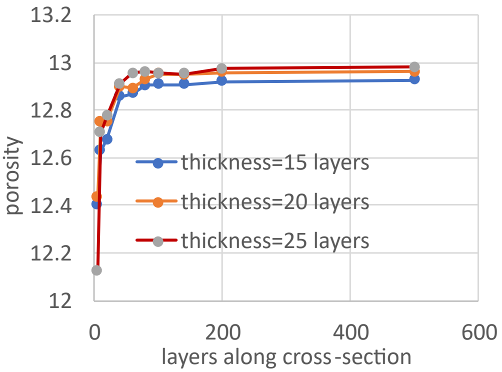

(a) Normal distribution

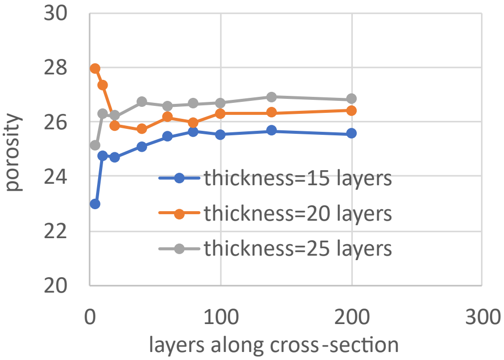

(b) Weibull distribution

Figure 6.5: Porosity variation with respect to domain size for networks with two different size distributions shown in figures above. For both distributions, results do not change beyond 100 layers along cross-section. Porosity changes more with thickness with Weibull distribution than normal distribution

The dependence of porosity and permeability on the domain's size is shown in Figure 6.5 and Figure 6.6. From the curves, it is distinctly visible that there should be at least 100 layers of pores and throats for the estimated porosity and permeability to become independent of size for a given thickness of the porous domain. This fact will also be important while considering networks extracted from actual PTLs. On the other hand, the curves show that for a normally distributed porous domain porosity or permeability does not change too much with respect to the number of layers along the flow direction. However, the same is not valid for the material constructed using both Weibull and normal distribution. This material is closer to real PTLs. Therefore, we can see that the thickness of the domain is likely to affect the computed parameters.

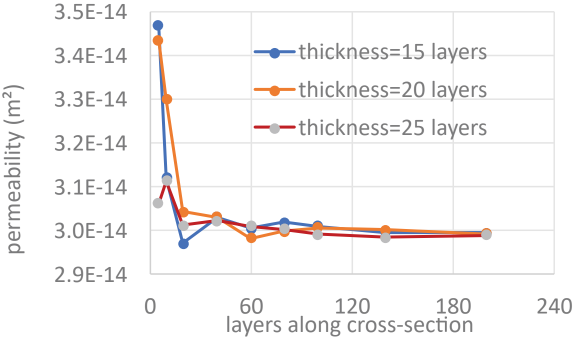

(a) Normal distribution

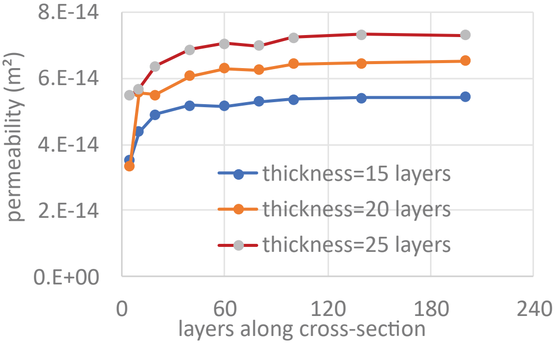

(b) Weibull distribution

Figure 6.6: Permeability variation with respect to domain size for networks with different size distributions shown in figure. For both distributions, results do not change beyond 100 layers along cross-section. Permeability changes more with thickness with Weibull distribution than normal distribution

Since the simulations were carried out on randomly generated cubic networks, these experiments' repeatability was also tested. For this purpose, networks with 20 layers along the flow direction were constructed with 80 and 140 layers perpendicular to the flow direction. Then ten different numerical experiments were repeated for each of these configurations. The result is shown in Figure 6.7. It is observed that for a domain of 140 layers, the results do not deviate much from the mean.

6.1.1.2 Correlation with Extracted Network

The previous section discussed the effect of network size on porosity and permeability. Natural materials like rocks are larger by few orders of magnitude than PTLs at least in one direction. In Figure 6.8 the results of how the extraction and preprocessing affect

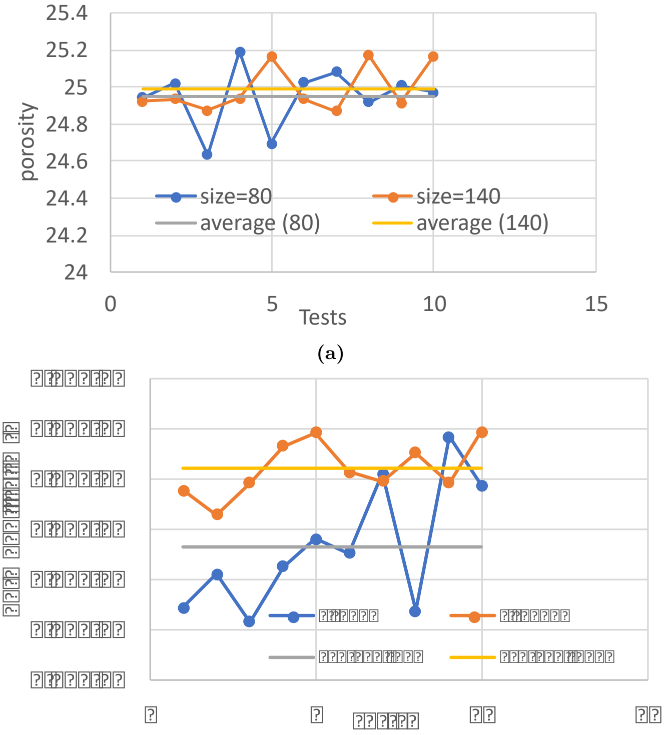

(a)

(b)

Figure 6.7: Repeatability of porosity and permeability for different network sizes is shown in the above figures. Two networks with 80 and 140 layers along cross-section were used. Along thickness directions 20 layers were used. For size=140 the computed porosity and permeability values show less variance.

the final outcome are shown. It usually happens that during the CT-image acquisition process, the object is not correctly aligned. Therefore, it becomes necessary to rotate or trim the 3-D stack before or after the extraction process. The top-most image in the figure shows a section from a sample of 250 µm thickness. If such a piece was cut from a rock or sandstone part, the trimming process would not influence the top or bottom surface as seen on the top-most image in Figure 6.8. However, due to the minimal thickness of the PTL sample, the actual surface of the material itself is visible here. From this sample three samples are prepared where different amount of background pixels are cropped, as shown in the second row of the images. Sample 1 was not processed (segmented) to distinguish the pore-solid interfaces clearly. Sample 2 and 3 were identically processed with only difference in the amount of background cropping. The third row of the images shows the networks as extracted directly from the maximal ball network extraction software. The fourth row of images shows the networks after rotating them by 1 °around X-axis and then

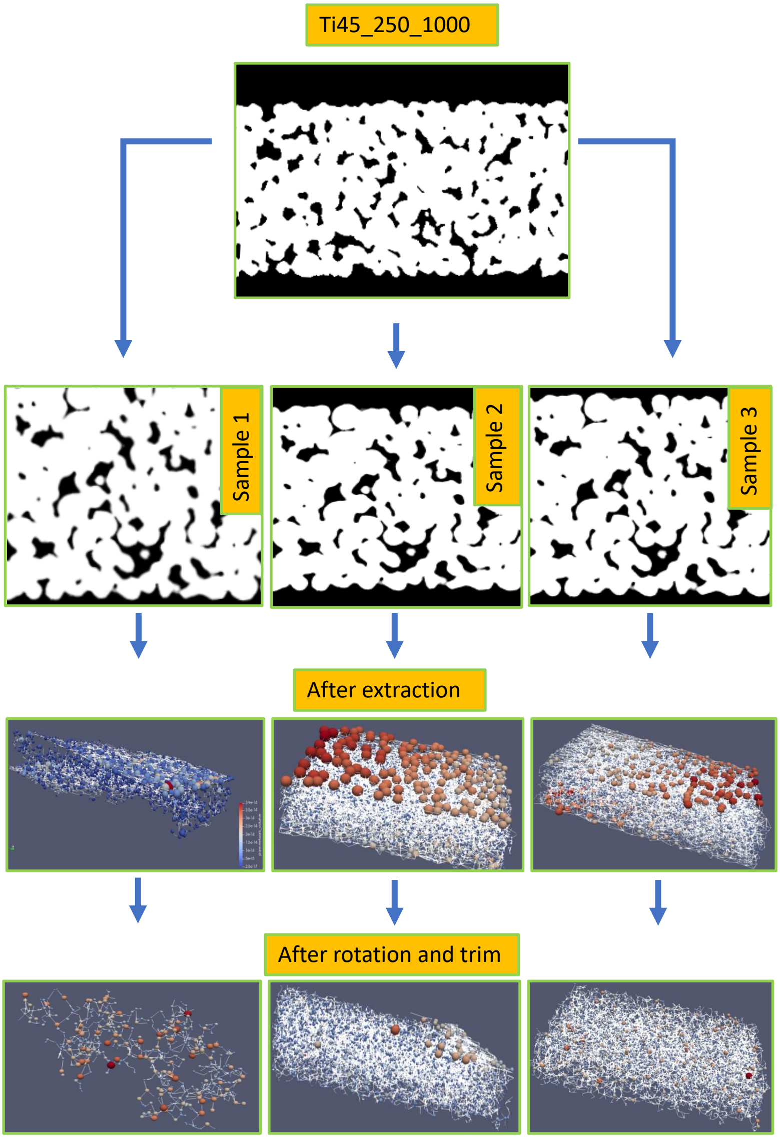

Figure 6.8: Effect of extraction process and image processing on the outcome of the network extraction process. The top image is a slice of the original stack. Sample 1 is not properly segmented. Sample 2 and 3 have different amount of background pixels. All networks are rotated by 1° around X-axis and trimmed by (5 %, 5 %), (8 %, 5 %) and (5 %, 5 %) of X, Y and Z dimensions respectively

trimming the surface pores with a given crop-factor (in these images y-direction is along the thickness of the material).

Table 6.3: Effect of network size and boundary cropping on permeability computed from simulation shown in the table. Removing the pixels in the thickness direction changes permeability value significantly [1]

Material			Ti45_250_1000	
Porosity (weight based)			0.193	
Porosity (Hg)			0.162	
Permeability (experimental)			8.19 E-13	
Sample	Size	y-crop factor	porosity	K ( )
1	734x185x888	0.05, 0.05	0.013	xxx
2	724x220x888	0.05, 0.05	0.204	1.02 E-11
2	724x220x888	0.08, 0.05	0.079	6.21 E-14
3	689x209x888	0.05, 0.05	0.075	2.18 E-15
3	689x209x888	0.08, 0.05	0.075	2.18 E-15

When the values presented in Table 6.3 and the images in Figure 6.8 are compared, it becomes visible that the network's thickness plays an important role. In all the cases, only thickness direction was considered. In the images, it aligns with the y-axis of the network. Sample 1 shows that when the images are not correctly segmented, extracted networks are not useful. It introduces a lot of errors or artefacts. Sample 2 and sample 3 show that depending on the amount of background pixels present, the network extraction can create many pores with a larger diameter on the surfaces. This effect, in turn, can have a significant impact on the flow simulations. Moreover, it also becomes clear that the small piece of PTL that was used for CT-imaging was different from the actual sample used for experimental measurement of porosity or permeability. Thus, this should be an important consideration while judging results from such numerical simulations.

6.1.1.3 Effect of Network Manipulation on Computed Quantities

After the initial numerical experiment on the artificially created networks, it was interesting to study some idealized scenarios that can represent some aspects of practical PTLs. For example, material compression, change of pore structure due to the manufacturing process etc. Hence four distinct situations were imagined:

- scaling the pore sizes by a factor
- scaling the pore-to-pore distance
- scaling the whole domain

---

[1] Experimental values measured by Olha Panchenko, Forschungszentrum Juelich

- changing the connectivity of the domain

Table 6.4: Details of reference cubic network to study the effects of scaling different network parameters

Network	Cubic
Lattice spacing (mm)	0.000020
Pore and throat size distribution	Weibull/Normal distribution
No. of layers along the flow direction	20
Cros-section	Square
Layers along cross-section	140
Scaling factor	0.90, 0.95, 1.00, 1.05, 1.10
Connectivity	5, 5.5, 6, 6.5, 7, 7.5, 8, 8.5, 9

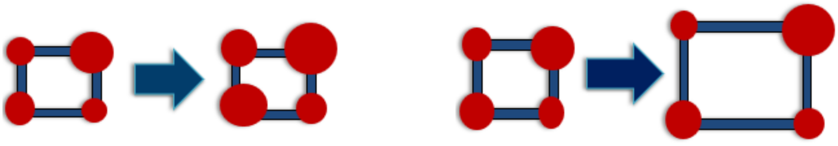

(a) Pore size scaling **(b)** Throat length scaling

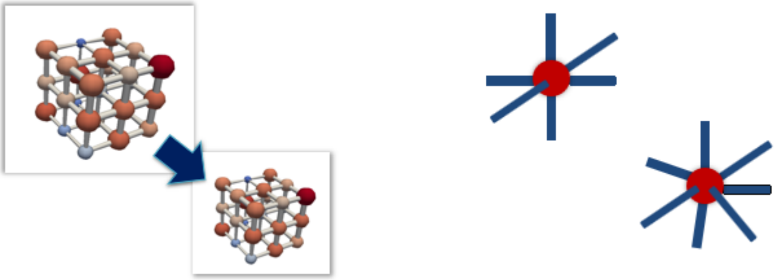

(c) Domain scaling **(d)** Connectivity variation

Figure 6.9: Network manipulation by changing different parameters is shown. For a network with given size, a) only pore size is changed by a factor b) Only throat length is changed by a factor c) everything is changed by a factor d) only connectivity is changed

It should be noted that the definition of a pore, throat, and connectivity may seem to be arbitrary. The definition of a pore and throat in the pore network model may differ from pore size in mercury porosimetry. Depending on the network extraction algorithm, the same material would produce different pore and throat sizes and different connectivity values. However, if one definition or method is consistently applied, it is still possible to gain meaningful insight.

To carry out simulations related to the scenarios above, cubic networks were constructed so that either the pore sizes, pore-to-pore distance, or the whole domain may be scaled from a reference dimension. Pore sizes were defined using a Weibull distribution in combination with a normal distribution. Except for the last scenario, for other tests, the networks had connectivity of 6 as defined by a cubic lattice. The details are shown in Table 6.4.

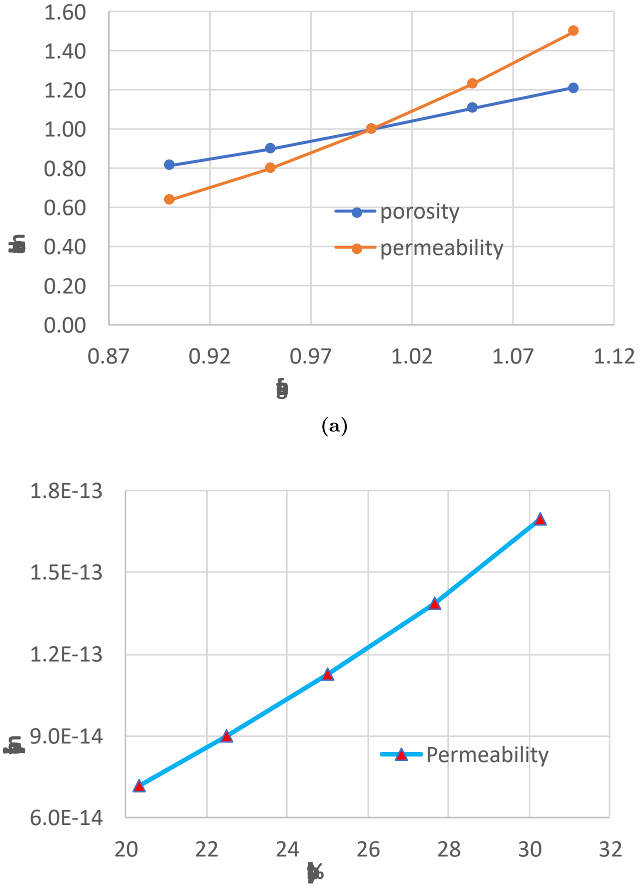

(a)

(b)

Figure 6.10: Porosity and permeability change as a result of pore size scaling is shown in the figures. a) Values are normalized with respect to a reference dimension (scale factor=1) b) Permeability is shown as a function of porosity. The middle point corresponds to the reference dimension (scale factor=1)

Figure 6.10 shows the result of scaling the pore size on the computed parameters. For this cubic network, the increase in pore sizes leads to higher porosity and larger throat diameters with shorter throat lengths. Thus, the throats' hydraulic conductance increases, which results in increased permeability as seen from the respective curves.

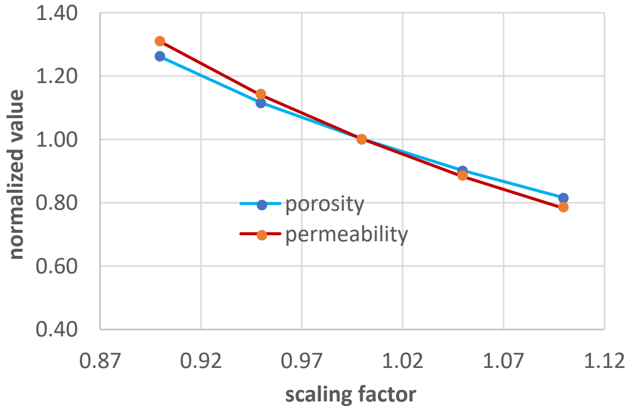

(a)

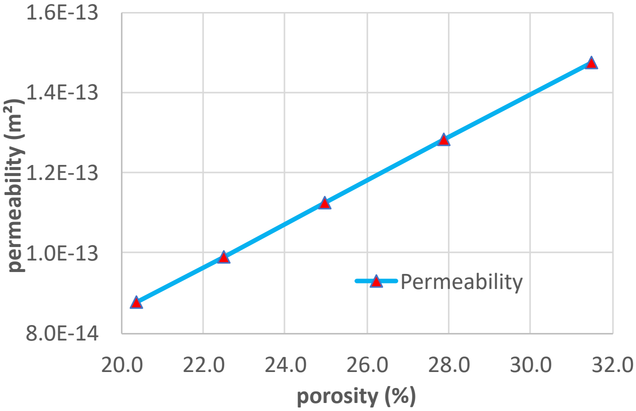

(b)

Figure 6.11: Porosity and permeability change as a result of pore to pore distance scaling is shown in the above figures. a) Values are normalized with respect to a reference dimension (scale factor=1) b) Permeability is shown as a function of porosity. The middle point corresponds to the reference dimension (scale factor=1)

Figure 6.11 shows the effect of scaling pore-to-pore distance while keeping everything else constant. It is observed that when the pore-to-pore distance is increased, porosity and permeability decrease as hydraulic conductivity of the throats decrease. However, porosity and permeability remain directly proportional.

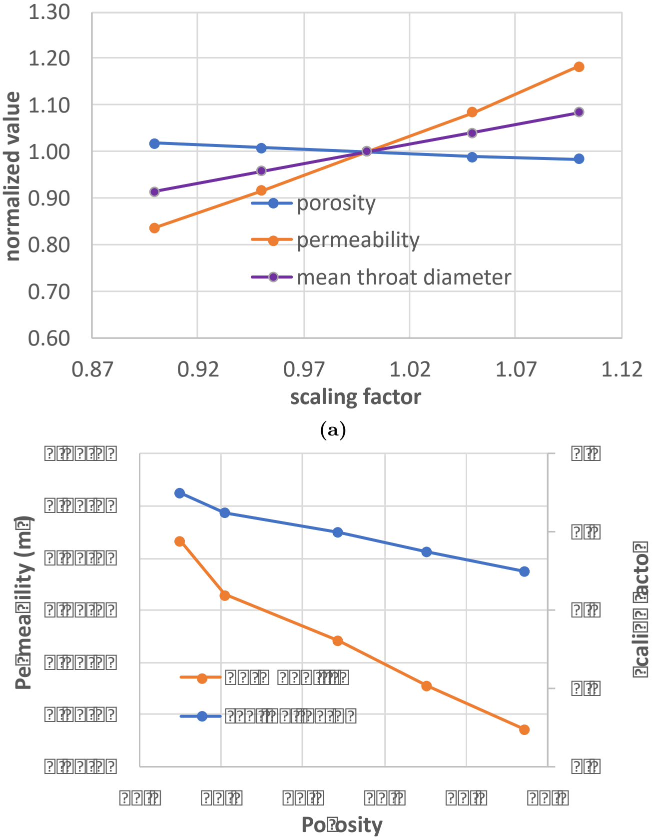

(a)

(b)

Figure 6.12: Porosity and permeability change as a result of scaling the whole domain in 3 directions is shown in figures. a) Values are normalized with respect to a reference dimension (scale factor=1). Porosity remains almost constant, but throat diameter increases resulting in increased permeability b) Permeability is shown as a function of porosity. The middle point corresponds to the reference dimension (scale factor=1).

Figure 6.12 shows the impact of scaling the complete domain on the measured quantities. When the domain is expanded, the porous material's permeability increases due increased pores and throat sizes. Although porosity of the domain should remain constant, the small variation visible in Figure 6.12a can be attributed to the smaller pores defined at the boundary surfaces.

In Figure 6.13 the comparison between networks having fixed connectivity of 6 (as shown in the right part of Figure 6.10 and Figure 6.11) and having given average connectivity from a randomly connected set of pores and throats are shown. The two lines on the left of

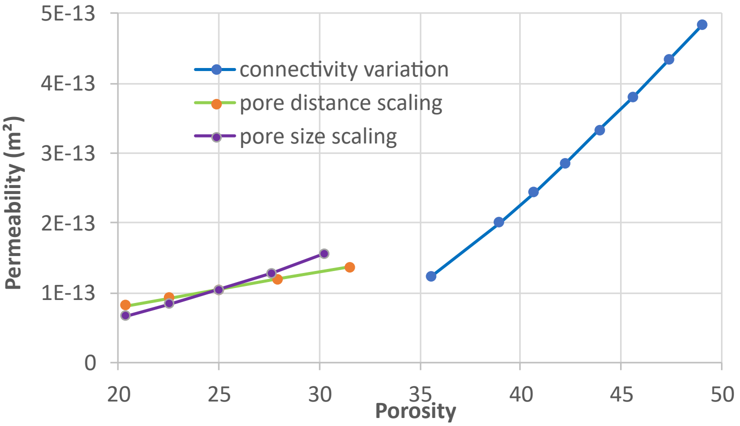

Figure 6.13: Permeability and porosity comparison for different network manipulation is shown in the figure. The lattice spacing is fixed, and same reference dimensions used for all cases. The curve on the right shows values for a network with random connectivity instead of default 6 where throats lie along the edges. Changing connectivity from the default value of 6 drastically alters permeability and porosity for the same lattice structure.

this diagram show the effect of scaling while the right curve shows the impact of changing connectivity for the same reference dimension as the mid-point of the left two lines. The connectivity value is varied between 5, 6, 6.5, 7, 7.5, 8, 8.5 and 9. The average connectivity values are obtained by first creating a network with redundant connectivity and then trimming some throats at random locations. It is observed that randomly changing the connectivity affects the porosity and permeability considerably for the same pore and throat size distribution. Till now only the edges of a cube were considered as connecting throats, but in the randomly connected network, a pore can connect in the diagonal directions as well, and the connectivity number is not fixed.

It was also important to study how the network connectivity influences network properties compared to a cubic network of fixed connectivity when porosity remains the same. Therefore, networks were constructed with random connectivity within the same porosity range as the reference cubic network when scaled. The result of this is shown in Figure 6.14a. On the other hand, Figure 6.14b shows when there is different average connectivity of the porous material for almost the same porosity value. From these figures, it is evident that connectivity has a far more significant influence than the increase in pore or throat sizes. While some numerical artefacts may be assumed due to spherical pores and cylindrical throats where multiple throats are connected to one single pore, the results can still indicate a general effect of connectivity on the network's permeability.

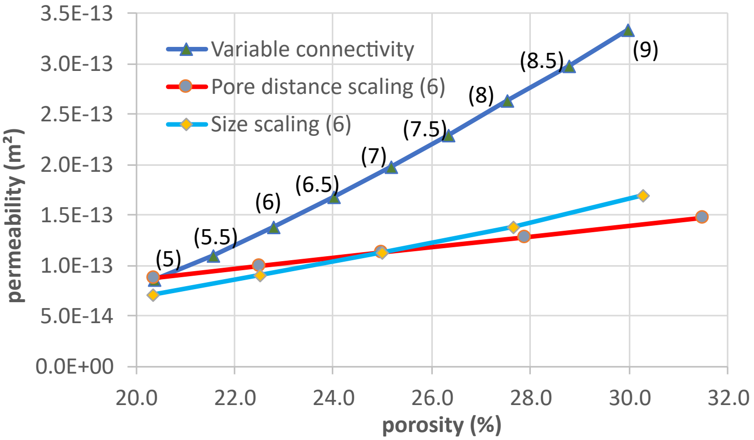

(a) Connectivity versus pore and throat size scaling

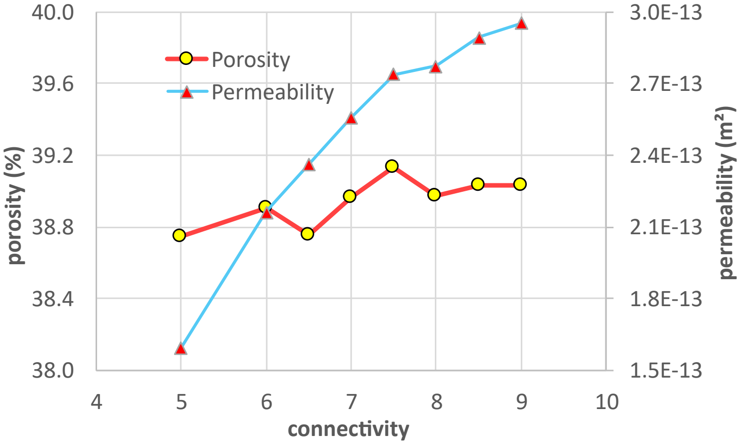

(b) Connectivity variation for same porosity

Figure 6.14: Effect of connectivity on permeability within same porosity range is shown in the figures. a) The light blue line corresponds to scaling pore size with respect to reference dimension with a regular cubic network with default connectivity 6. The orange line corresponds to pore-to-pore distance scaling for the same. The blue line corresponds to cubic networks with different average random connectivity. The network parameters are varied such that the resultant porosity values are comparable to the other two lines. b) Networks with random connectivity are created in such a way that the porosity remains nearly constant.

6.1.1.4 Correlation with Experimental and Numerical Results

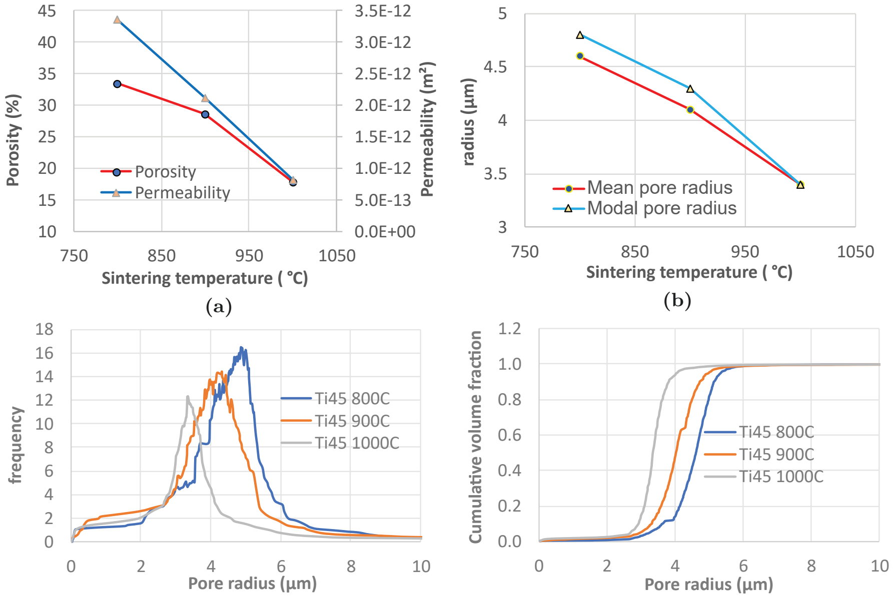

(a) (b)

(c) (d)

Figure 6.15: The impact of sintering temperature on PTL characteristic for the same material sintered at three different temperatures is shown.[2]

The effect of network manipulation under different conditions described above can also be correlated from experiments. Experimental data related to three PTL samples sintered at 800, 900 and 1000 °C are shown in Figure 6.15. The plots in the figure correlate well with the plots in the previous section. Further results pertaining to these samples can be found here [190]. These PTLs were sintered from particles of size 45 µm to a thickness within the range of 250 µm. The plots show the decrease in permeability and the decrease in mean and modal pore radius (as determined by Hg-porosimetry) with the increase of sintering temperature. CT-images were not available for all three samples to compare with simulations. However, both simulation and experimental data were available for three similar materials in the dissertation of Hoeh [27, p. 63-64, 123]. From these images, networks were extracted using the maximal ball algorithm; simulations were performed to compute permeability. Resulting network parameters and their correspondence to the measured values are presented in Table 6.5.

---

[2] Experimental data from Ulla Panchenko, see [190, P. 40-43]

[3] Experimental permeability data from M Hoeh [27, P. 123]

Table 6.5: Influence of network parameters on computed permeability and comparison with experimental results [3]

Material	Ti45C8	Ti45D	Ti45Cx
Sinter Temperature °C	750	850	950
Porosity %	29.8	23.6	12.9
Mean throat diameter	1.77	1.72	2.10
Mean throat length	3.65	3.73	4.17
Mean pore diameter	4.14	3.85	4.81
Connectivity	7.2	5.6	2.9
Permeability (experimental)	1.18	7.25	1.49
Permeability (simulation)	1.60	8.91	7.11

This table shows that the network parameters correlate well with the behaviour described in the previous section. Thus, there is a possibility of finding a relationship between the sintering process and PTL mass transport behaviour. However, further study would be required to understand this fully.

6.1.2 Flow Simulation on Extracted Networks

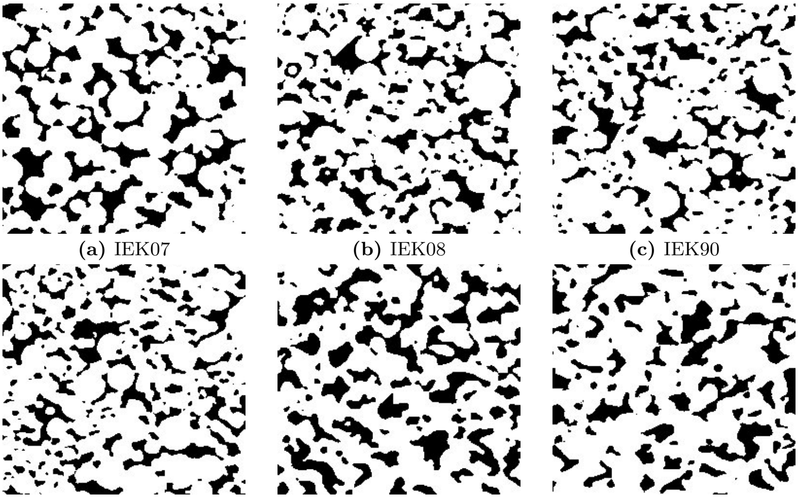
(a) IEK07 **(b)** IEK08 **(c)** IEK90
(d) IEK91 **(e)** IEK41 **(f)** IEK44

Figure 6.16: Images of 250 pixel x 250 pixel cross-section of the PTLs

After the simulations described above, simulations were carried out on networks extracted from the samples described in Section 5.1. From the CT-images of these samples, regions having a cross-section of 600x600 pixels (resolution = 1.02 µm) were chosen for network extraction. Figure 6.16 shows slices of these materials. Network extraction employed two

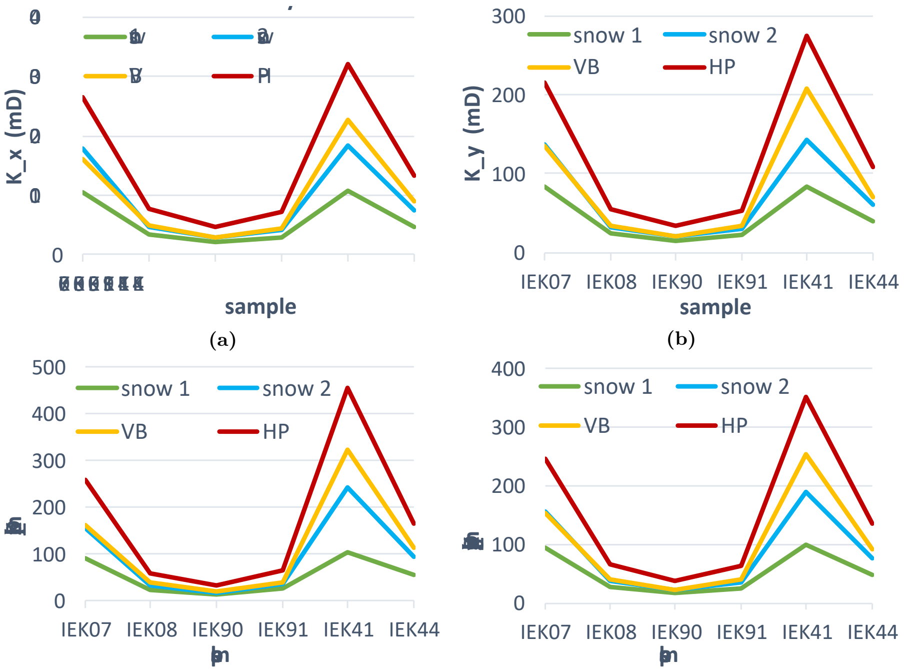

(a)

(b)

(c)

(d)

Figure 6.17: Permeability along different directions as computed from pore network simulations for different network extraction methods and conductance models

different methods, namely SNOW algorithm developed by Gostick [72] and Maximal Ball (MB) algorithm by Dong and Blunt [71]. Subsequently the permeability of the extracted networks were computed in three directions using four different models for hydraulic conductance. The permeability values of the extracted networks were computed in three directions using four different models for hydraulic conductance. The SNOW algorithm defines two diameters: inscribed diameter and equivalent diameter. Details can be found in the corresponding literature. The following terminologies are used to present the results of the simulations:

- **snow 1** refers to SNOW network extraction followed by hydraulic conductance estimation based on inscribed diameter.
- **snow 2** refers to SNOW network extraction followed by hydraulic conductance estimation based on equivalent diameter (refer to Section 4.3.5).
- **MB+VB** refers to MB network extraction followed by hydraulic conductance estimation based on the works of Valvatne and Blunt [174]. The VB model is a part of OpenPNM package.

- **MB+HP** refers to MB network extraction followed by hydraulic conductance estimation based on classic Hagen-Poiseuille (HP) model.

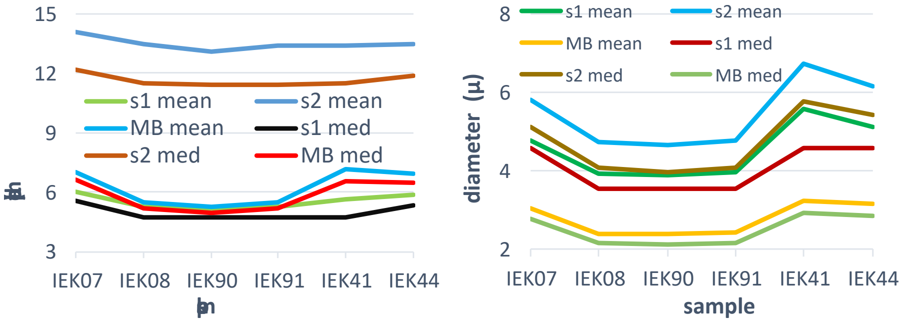

(a) pore diameter **(b)** throat diameter

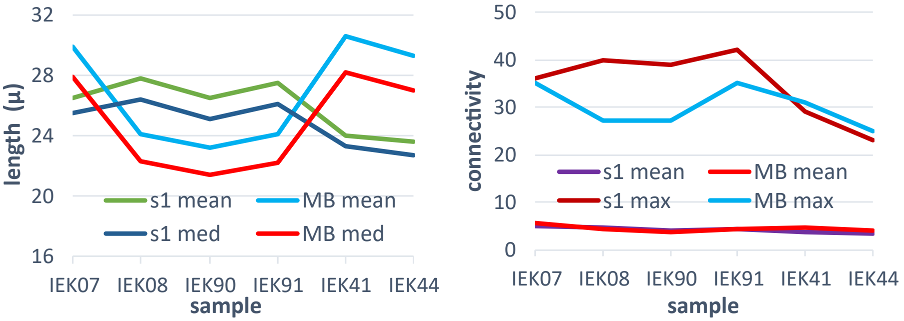

(c) throat length **(d)** connectivity

Figure 6.18: Pore and throat diameter, throat length and connectivity details of extracted networks. s1, s2 and MB refers to snow 1, snow 2, and maximal ball respectively. Mean, med, and max refers to the mean, median, and the maximum value in each category

The computed permeability values are plotted in the graphs in Figure 6.17. These values, in contrast with the experimentally measured values, are shown in Table 6.6. From the table, it becomes clear that using inscribed pore diameter (‘snow 1’) leads to an underestimation of permeability values compared to other simulation methods and experimental results. So it can be understood that it is not a reliable method for the estimation of permeability. SNOW network extraction combined with equivalent diameter for hydraulic conductance calculation (‘snow 2’) matches closely with the MB network extraction and VB model for hydraulic conductance. For the samples IEK41 and IEK44, which are sintered from irregularly shaped particles, the MB+VB method leads to a higher degree of overestimation than snow 2. The other samples were sintered from spherical particles. This means that the resulting structures from two different materials have an impact on the network extraction

Table 6.6: Permeability calculated from pore network simulations. All values in mD. Experimental data shown for reference

Sample	IEK07	IEK08	IEK90	IEK91	IEK41	IEK44
snow 1	106	33	21	30	108	48
	83	24	15	22	84	39
	91	23	12	25	104	54
	93	27	16	26	99	47
snow 2	179	47	29	42	183	76
	137	33	20	30	142	61
	155	32	16	35	241	95
	157	37	22	36	189	77
MB+VB	162	49	29	44	228	89
	136	35	20	34	207	70
	162	38	19	40	324	112
	153	41	23	39	253	90
MB+HP	264	78	48	73	321	132
	215	56	35	54	275	108
	258	60	33	66	456	166
	246	65	39	64	351	135
Experimental	280	72	77	72	163	120
Experimental	420	127	159	165	270	123
Thickness	504	468	473	463	136	297
Porosity % (pixel)	27.8	24.1	21.3	24	33.1	26.4
Porosity % (measured)	34.4	28.6	26.6	26.1	36.0	33.5

process. Out of the four methods, the fourth one produces the highest permeability for the networks. These values are close to the measured through-plane permeability. The fourth method estimates approximately twice that of the measured value for only one sample, i.e. IEK41. This behaviour could be an outcome of the size effect in the network extraction process. The results also show that computed permeability along any of the three directions is much smaller as compared to the measured in-plane permeability values. Thus, strong anisotropy is not visible from the simulations.

The details of the extracted networks are presented in Table 6.7 and Table 6.8. Corresponding plots are shown in Fig. 6.18. The distributions for pore diameter, throat diameter, throat length and connectivity for both extraction methods are plotted side-by-side in Figure 6.19. These distributions are shown as the percentage of the total number corresponding to one parameter. The size distribution plots show that IEK08, IEK90 and IEK91 have identical pore and throat size distributions, while IEK07, IEK41 and IEK44 another identical distribution. The sample IEK08, IEK90 and IEK91, have approximately the same thickness (500) and similar pore details as visible from Figure 6.16. The

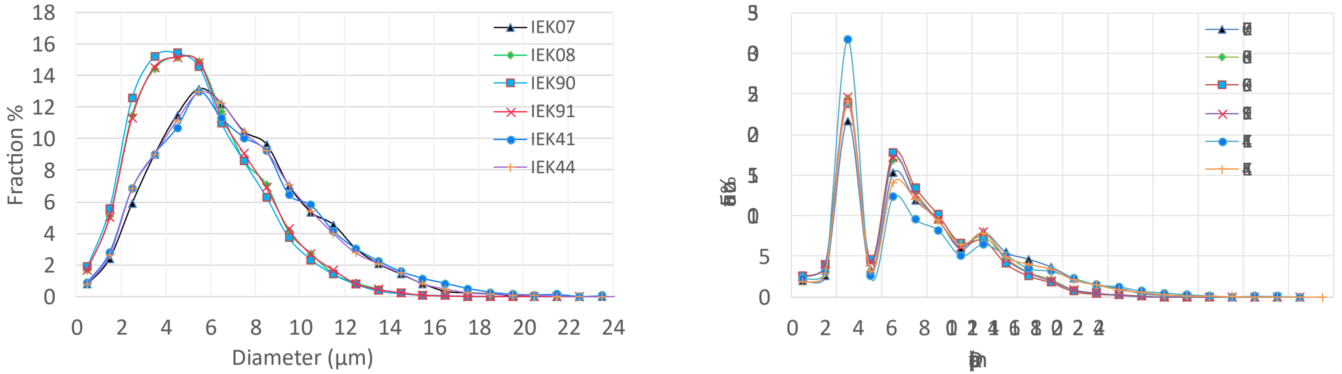

(a) Pore diameter MB

(b) Pore diameter SNOW

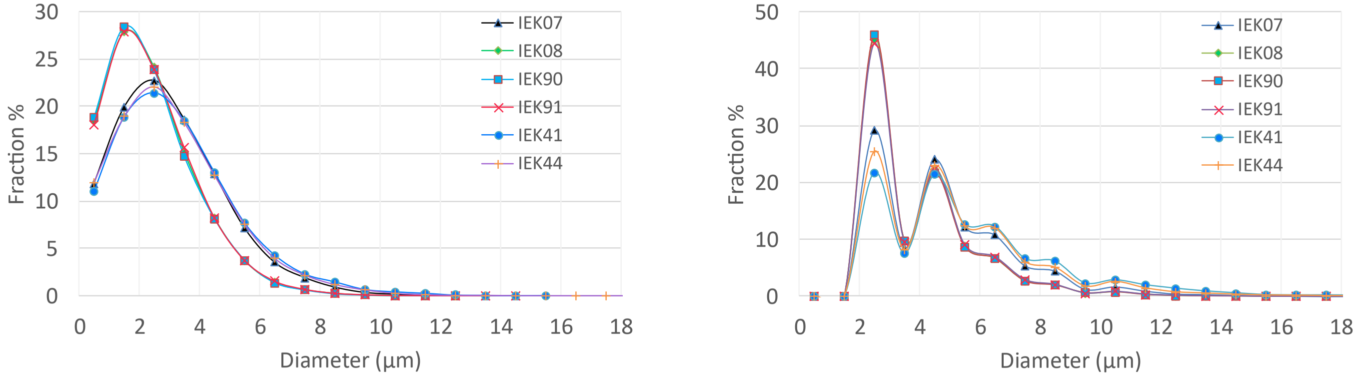

(c) Throat diameter MB

(d) Throat diameter SNOW

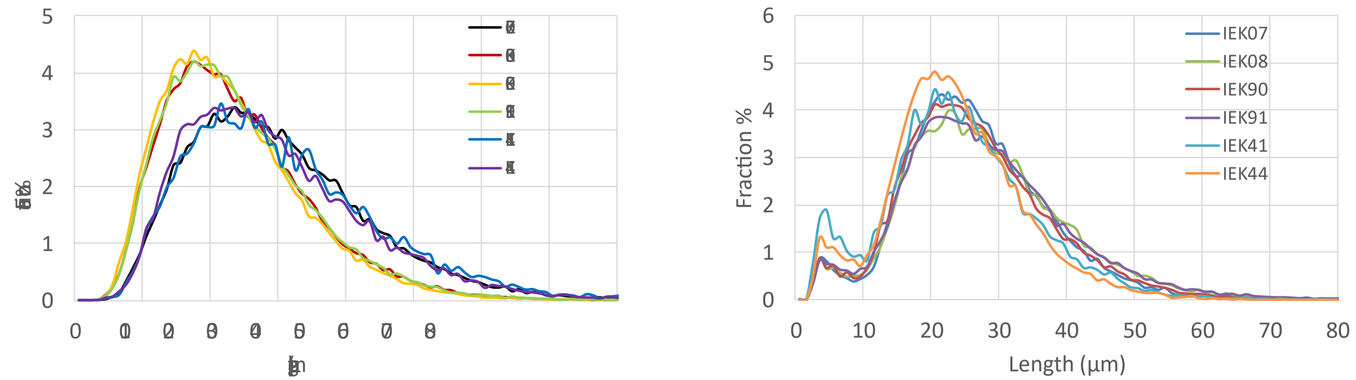

(e) throat length MB

(f) throat length SNOW

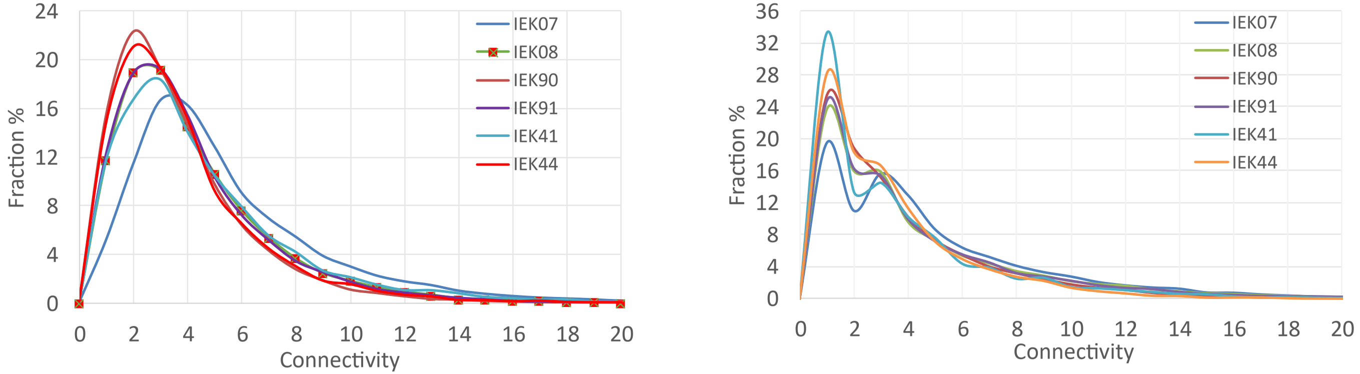

(g) connectivity MB

(h) connectivity SNOW

Figure 6.19: Pore and throat diameter, throat length and connectivity distribution of extracted networks. The x-axes are trimmed so that the distributions are clearly visible

Table 6.7: Details of the extracted networks, Part-I: pore and throat size details

Throat diameter ( )

Sample	geodict		snow 1		snow 2		MB	
IEK07	6.4	6.1	4.8	4.6	5.9	5.1	3.1	2.8
IEK08	4.9	4.8	4.0	3.5	4.8	4.1	2.4	2.1
IEK90	4.7	4.6	3.9	3.5	4.6	4.0	2.4	2.1
IEK91	4.9	4.7	4.0	3.5	4.8	4.1	2.4	2.2
IEK41	7.6	7.3	5.6	4.6	6.7	5.8	3.2	2.9
IEK44	6.6	6.0	5.1	4.6	6.2	5.4	3.2	2.8

Pore diameter ( )

Sample	snow 1		snow 2		MB	
IEK07	6.0	5.6	14.1	12.2	7.0	6.6
IEK08	5.2	4.7	13.5	11.5	5.5	5.2
IEK90	5.2	4.7	13.1	11.4	5.3	5.0
IEK91	5.2	4.7	13.4	11.4	5.5	5.2
IEK41	5.6	4.7	13.4	11.5	7.1	6.6
IEK44	5.9	5.3	13.5	11.9	7.0	6.5

Throat length ( )

Sample	snow		MB	
IEK07	26.5	25.5	29.9	27.9
IEK08	27.8	26.4	24.1	22.3
IEK90	26.5	25.1	23.2	21.4
IEK91	27.5	26.1	24.1	22.2
IEK41	24.0	23.3	30.6	28.2
IEK44	23.6	22.7	29.3	27.0

high permeability of the IEK07 sample can be understood from the fact that it has the highest connectivity of all the samples and larger pore and throat diameters. Table 6.7 and Table 6.8 show that the MB algorithm, in general, produces a larger number of pore and throats than the SNOW algorithm. Pore diameter and throat length from both the algorithms are nearly equal, but the MB algorithm's throat diameter almost half that of the SNOW algorithm. The pore and throat size distributions from both algorithms show that MB algorithm produces a smooth Gaussian-like distribution. The SNOW algorithm produces a wave-like pattern in all the distributions. Moreover, SNOW algorithm produces a large fraction of pores with the connectivity of one, while the MB algorithm produces pores such that the largest fraction has a connectivity of two.

Table 6.8: Details of the extracted networks, Part-II: showing connectivity details, and the number of pores and throats detected

Connectivity

Sample	snow		MB	
IEK07	5.0	36	5.5	35
IEK08	4.5	40	4.3	27
IEK90	3.9	39	3.7	27
IEK91	4.4	42	4.2	35
IEK41	3.8	29	4.6	31
IEK44	3.5	23	3.9	25

Pores and throats

Sample	snow		MB	
	pores	throats	pores	throats
IEK07	18578	46453	20291	55540
IEK08	16018	36076	32335	68814
IEK90	16384	32384	31768	59183
IEK91	16184	35405	31725	66205
IEK41	6601	12457	5944	13644
IEK44	12153	21278	12045	23337

6.1.3 Simulation of Two-phase Flow

Two-phase flow simulations were carried out to determine the relative permeability of the extracted networks. To achieve this invasion percolation simulation was performed from one of the surfaces of the network. Then different network configurations were obtained for different water saturation values. Pore and throat accessibility by a given phase was determined based on the occupancy of that phase in each configuration. Then stokes flow simulations were performed to compute effective permeability. Invasion percolation is based on the method by [75]. Washburn equation is used to calculate the entry pressure for each throat.

$$\frac{\qquad}{\qquad} \qquad (6.1)$$

Thereafter the throats are sorted in the order of increasing entry-pressure. The invading phase enters through the inlet surface such that at each step only throats/pores connected to a given pore can be invaded, only if the applied pressure is higher than the throat entry pressure. To ensure zero starting saturation at the beginning of percolation, fictitious pores with zero volume are added on the inlet side. Once percolation is complete, the pore and throat occupancy configuration for a given saturation can be obtained. While computing the effective permeability, these occupied pores and throats can be marked as inaccessible

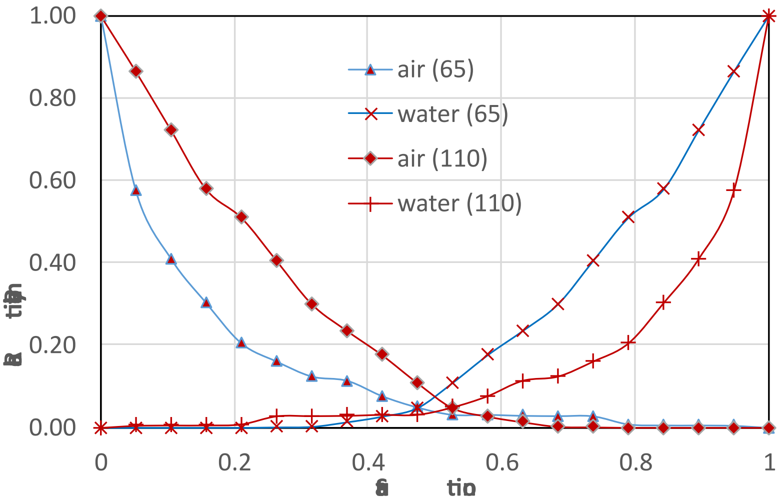

Figure 6.20: Effect of wettability on relative permeability of IEK07 (x-direction) is shown in the figure. The number in the bracket indicates the contact angle of water. Changing the contact angle shifts the relative permeability curve

to the second phase based on certain conditions. It is evident from the Washburn equation that when the same values of surface tension and contact angle are defined for the whole network, any change in its value would only shift the entry-pressure values. However, the network's configuration for different saturations will remain the same unless local modifications are implemented. Thus, this model can only capture change with respect to wetting and non-wetting contact angles. Any value of contact angle would produce the same results for these two cases.

In Figure 6.20 the effect of wettability is shown for the sample IEK07 in the x-direction. One face along this axis was used as the inlet surface for the invasion percolation process. The number in the brackets indicate the assumed contact angle between water and PTL surface. The figure shows that for non-wetting contact angle (110°), the curves shifts towards the right. This shift means air relative permeability is higher than the same for wetting contact angle until it crosses the water relative permeability line and water relative permeability is lower compared to the same for wetting contact angle beyond this point. Since titanium PTLs used in the electrolysis process are not treated with a hydrophobic substance, a contact angle value of 65° was chosen for the simulations.

In OpenPNM, three conduit models can be defined for the access to the pores and throats of the displacing phase for each configuration of the occupant phase. A conduit consists

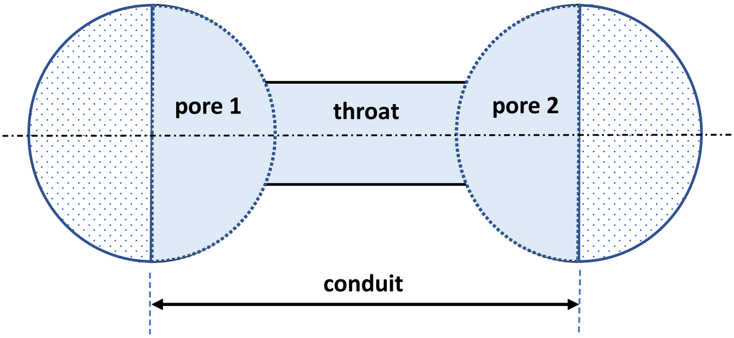

Figure 6.21: A throat and one half from each connected pore and forms a conduit

of a throat and half of each pore on either side. Based on Figure 6.21, the conduit models can be described as follows [191]:

- 'strict': if any pore or throat in a given conduit is not occupied by the given phase then it is closed to that phase
- 'medium': if either the throat or both pores are not occupied by the given phase then it is closed to that phase
- 'loose': if the throat is not occupied by the given phase then it is closed to that phase

In Figure 6.22 the conduit model's influence on the computed relative permeability curves is shown for both wetting and non-wetting contact angle between water and PTL surface. When we use wetting contact angle between water and PTL surface air is used as the invading phase in the percolation simulation. The conduit models apply to the wetting phase only. Hence, the air relative permeability line for all three conduit models remains the same. Similarly, when a non-wetting contact angle between water and PTL surface is considered, the line for water relative permeability remains the same. Relative permeability computation for titanium PTLs through pore network simulation has been reported by Hoeh [27, p. 129]. It is observed that a model similar to the 'loose' conduit flow model was used for the simulation. But based on the permeability measurements discussed in Section 5.3, and on literature from [20–22, 163], it becomes clear that the 'strict' conduit flow model is more likely to produce realistic results. Thus, our samples' relative permeability was computed assuming wetting contact angle (i.e. °) between water and pore surface, and 'strict' mode for conduit flow.

The results for relative permeability computation of the extracted networks are shown in Figure 6.23. For the sample IEK07, the curves in all three directions look nearly identical. But for the samples IEK08, IEK90 and IEK91 the water permeability lines

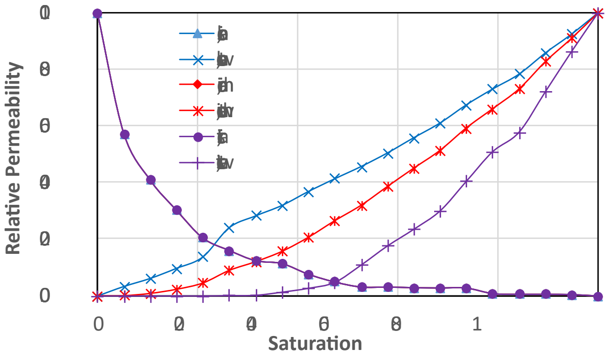

(a)

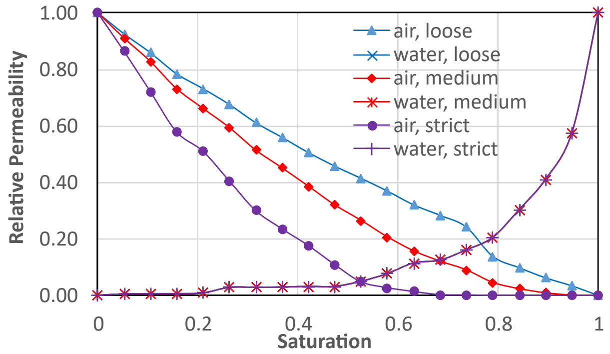

(b)

Figure 6.22: Influence of conduit model on relative permeability a) Curve with a wetting contact angle. The air relative permeability curve remains unchanged b) Curve with a non-wetting contact angle. The water relative permeability curve remains unchanged

along x-direction (inlet direction for invasion percolation) remain almost flat until around 90% water saturation; and then, it suddenly increases to 1. This can be explained from the pore and throat diameter distribution, as shown in. Figure 6.18 and Figure 6.19. The samples IEK08, IEK90, and IEK91, have higher fractions of smaller size pores and throats than the other samples. Thus, when the pores on the inlet side of the non-wetting phase (air) remain blocked, it lowers the effective permeability of water in that direction. The samples IEK41 and IEK44 show different behaviour in all three directions. Moreover, the curves appear to be more wavelike. The pore and throat sizes reveal that these two samples have a relatively higher fraction of pores between 8-20 µm size as compared to the other samples. This is an outcome of the fact that these two samples were sintered from irregularly shaped titanium particles while the others were sintered

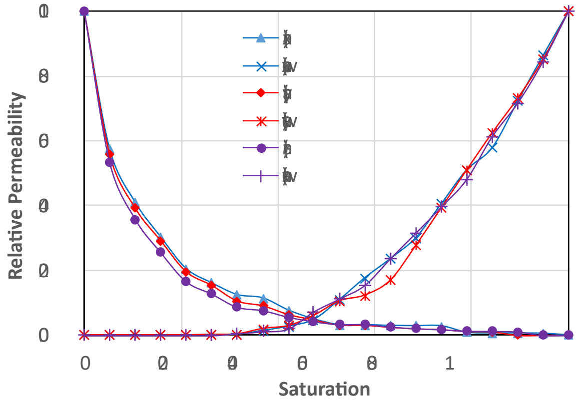

(a) IEK 07

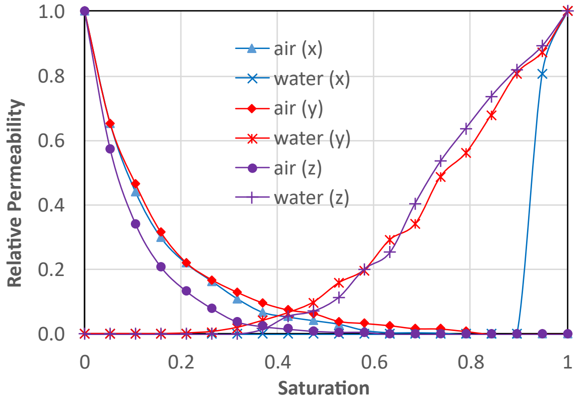

(b) IEK 08

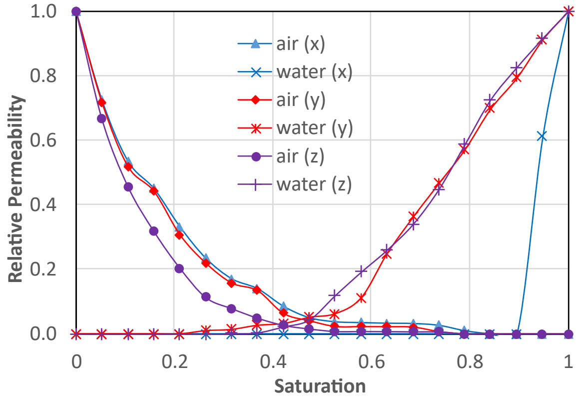

(c) IEK 90

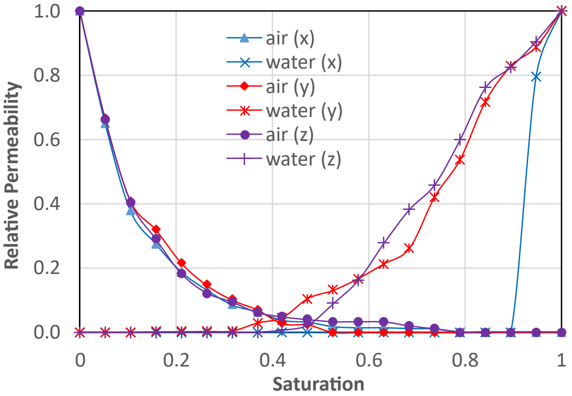

(d) IEK 91

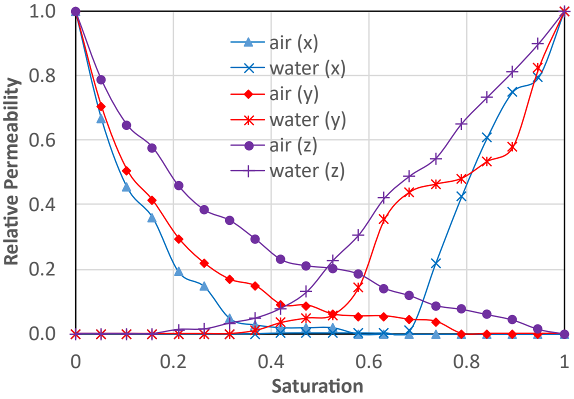

(e) IEK 41

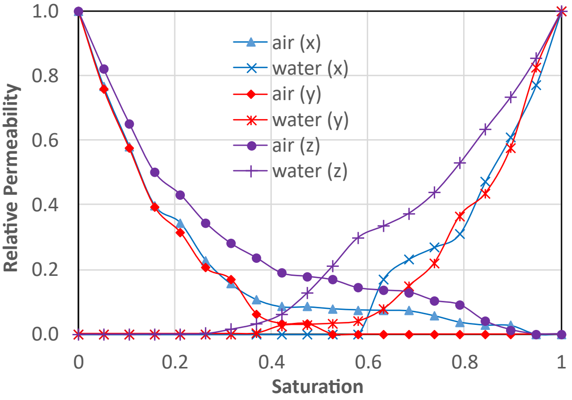

(f) IEK 44

Figure 6.23: Relative permeability of PTLs computed from simulation. Letters within brackets indicate the direction of calculation; contact angle=65°

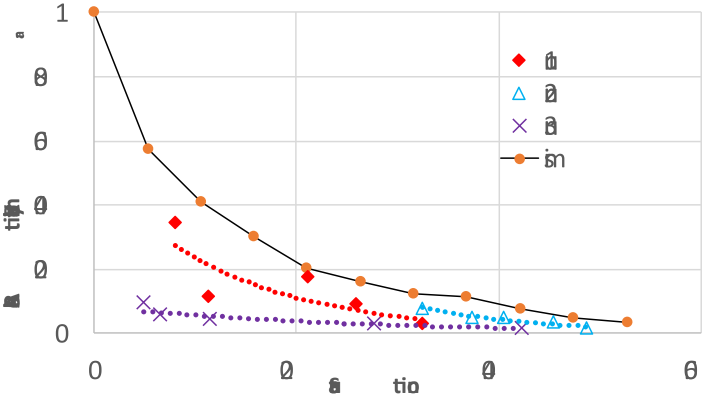

(a) IEK07

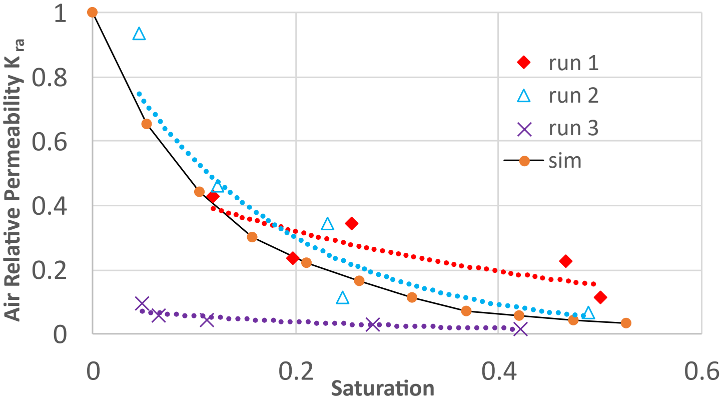

(b) IEK08

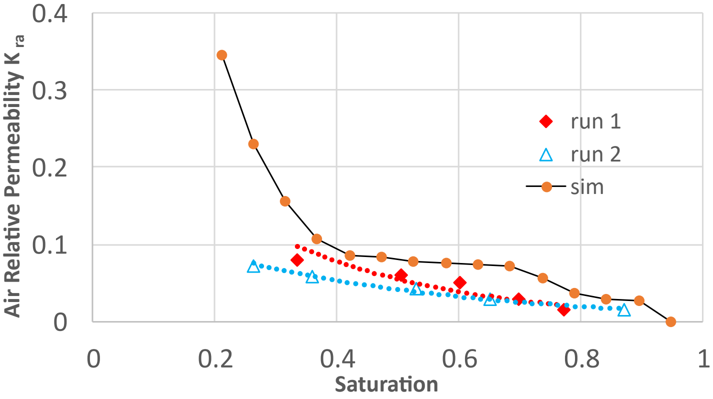

(c) IEK44

Figure 6.24: Comparison of computed air relative permeability with experiments

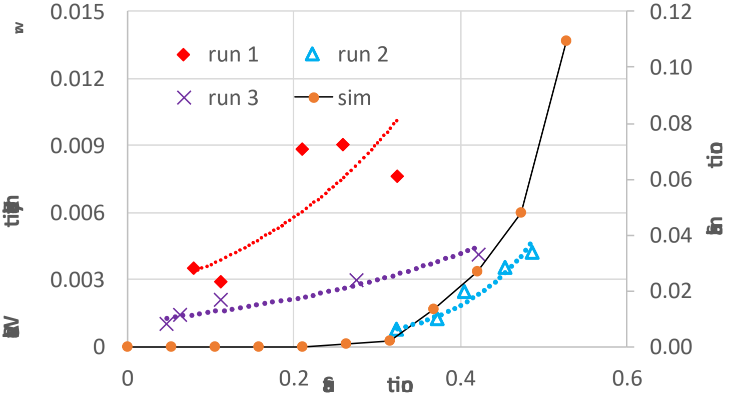

(a) IEK07

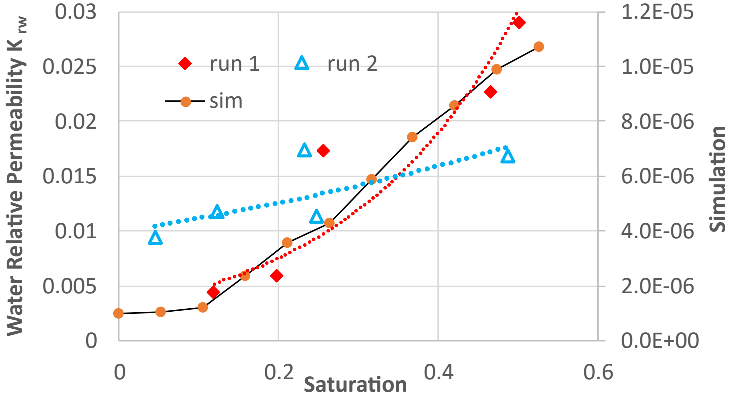

(b) IEK08

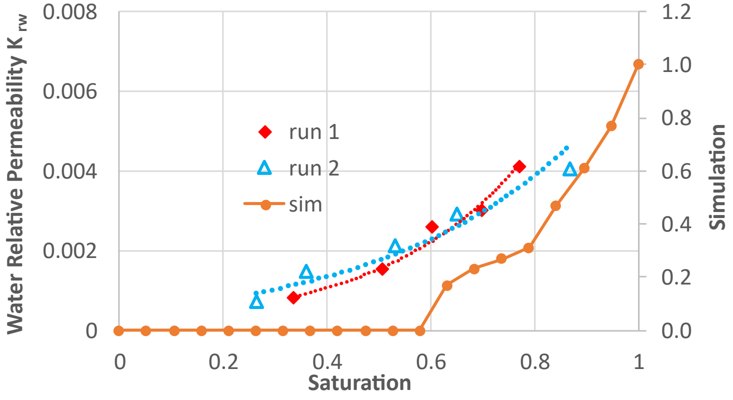

(c) IEK44

Figure 6.25: Comparison of computed water relative permeability with experiments

form spherical particles. The computed relative permeability values are compared with the experimental values in Figure 6.24 and Figure 6.25. To visualize the curves properly, the part of simulation data corresponding to a similar range of saturations as that of the experiments are used. It is observed that computed air relative permeability curves match closely with the experimental values. However, the relative permeability curves for water differ significantly between simulations and experiments. For the samples IEK07 and IEK44, the simulations overestimate water effective permeability; but for the sample IEK08, the simulations underestimate the same although relative permeability for both simulations and experiments are close to zero.

The experimental curves show that water relative permeability is higher for IEK08 sample than the other two for the same range of water saturation. From the pore and throat size distribution, it can be observed that IEK07 and IEK44 have a higher fraction of pores within the range 6-10 µm as compared to IEK08, which means that it is difficult for water to enter the larger pores and throats to displace the air. This results in the lower relative permeability of these two samples.

6.2 Comparison of Simulation Tools

The previous section discussed absolute and relative permeability computation of PTL samples using pore network model. There are other simulation methods such as Lattice-Boltzmann methods, conventional Computational Fluid Dynamics (CFD), and Morphological methods. Numerical simulations provide a cheaper and less time-consuming alternative to experimental measurements. However, it is essential to ensure that different tools conform to one another with respect to the computation of parameters of interest. Apart from conformity among the software, it is equally important that they are experimentally validated. Therefore, in this section, the permeability computation between different tools and experiments are compared. As discussed earlier, Geodict, Palabos[4] and Ansys[5] Fluent results are compared with OpenPNM and experimental results.

For the simulations involving OpenPNM and Geodict, the same 3-D image stacks were used for each of the materials. All these samples had a cross-section of 600x600 pixels. The 3-D image stacks for Palabos were larger in size. However, all of them were larger than the representative element volume calculated based on the change of porosity with respect to change in domain cross-section. It was also separately verified by computing permeability with pore network model so that the change of domain cross-section does

---

[4] Simulations were performed by Dieter Froning at JURECA cluster, Forschungszentrum Juelich.

[5] Simulations were part of a master thesis supervised as a part of this doctoral work. Simulations carried out by Simson Julian Rodrigues

Table 6.9: Comparison of permeability computed from different simulation tools, permeability values in mD

Sample	IEK07	IEK08	IEK90	IEK91	IEK41	IEK44
GeoDict	211	75	50	73	231	118
	169	56	36	52	189	91
	194	57	32	60	266	122
	191	63	39	62	228	110
LBM	220	80	55	76	230	110
	170	59	41	56	190	93
	200	56	44	65	290	120
	197	65	47	66	237	108
Fluent	244	216	166	166	324	333
	204	103	51	44	1344	220
	93	144	105	139	887	352
	180	155	107	117	851	302
MB+VB	162	49	29	44	228	89
	136	35	20	34	207	70
	162	38	19	40	324	112
	153	41	23	39	253	90
MB+HP	264	78	48	73	321	132
	215	56	35	54	275	108
	258	60	33	66	456	166
	246	65	39	64	351	135
Experimental	280	72	77	72	163	120
Experimental	420	127	159	165	270	123
Porosity (fluent samples) %	34.4	28.6	26.6	26.1	36.0	33.5
Porosity (others) %	27.8	24.1	21.3	24	33.1	26.4

not change the permeability. Based on this, the domain of 600x600 pixels was considered satisfactory. The same does not hold for Fluent simulations. Because of computational limitations, only a small cross-section of up to 200x200 pixels could be used.

The results of the simulations are shown in Table 6.9 and Figure 6.26. For the pore network simulations only ‘MB+VB’ and ‘MB+HP’ results are considered because the former is nearly identical to the ’snow 2’ method, and the latter closely matches the experimental results. The results show that even though the same domain size was not used, Geodict and LBM produces nearly identical results. The ‘MB+HP’ method produces values higher than either of these methods. So far, this is the method that produces results closer to the experimental values. The permeability computed from Fluent simulations differs significantly from all the simulations and experiments. Although the fluent results match with simulations in specific directions for a given sample, that is not valid for each direction and each sample. This can be attributed to the smaller domain size, which

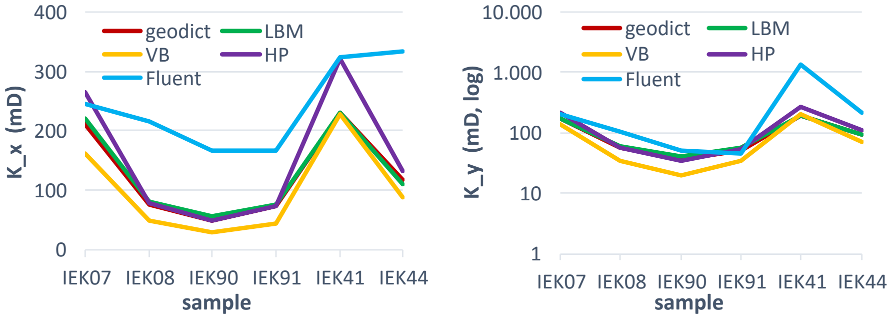

(a) x- direction **(b)** y-direction

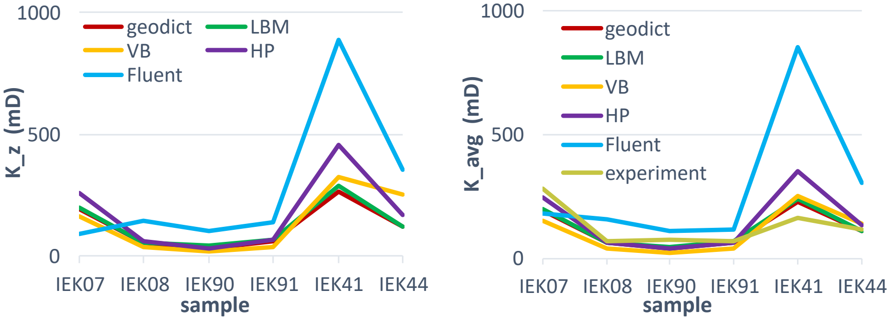

(c) z-direction **(d)** average

Figure 6.26: Comparison of permeability computed by different simulation tools. In d) The average values are compared against the through-plane experimental permeability as well. The figures show that the fluent results do not represent actual materials as only small portions could be used for modelling.

cannot represent the material properties accurately. The porosity of the samples used for the fluent simulations also confirms this fact.

6.3 Summary

In this chapter, the numerical characterization of the PTLs was described. A sensitivity analysis of different network parameters was performed while considering reference dimensions from actual PTLs. Based on this, the effect of manipulating these parameters that can also occur due to different manufacturing or physical processes was considered. The effect of thickness of PTLs on the computed values was analyzed to show that image processing and network extraction would impact the final computed values. Then extracted network details for all the six samples were presented, including size distributions. Computation of permeability for different network extraction and pore-scale models were compared to determine the most suitable methods. It was found that SNOW network extraction with effective diameter for hydraulic conductance produces results comparable to the MB network extraction with VB method for hydraulic conductance. However, MB extraction with simple Hagen-Poiseuille model was found to be closer to the experimental values. A comparison of different simulation tools, namely OpenPNM, GeoDict, Palabos (LBM) and Fluent, was performed. The Fluent results deviated from the other simulations and experiments because the domain size did not represent the actual PTLs. Moreover, it was complicated and computationally intensive to model actual two-phase flow. Among the other methods GeoDict and LBM methods produce nearly identical results. Pore network model was used to compute relative permeability of the extracted networks. It was found that computed air relative permeability curves closely match with the experimental values, but the water relative permeability values differ by multiple orders of magnitude from experimental values.

Chapter 7

Discussion

This work attempted to characterize PTLs used in PEM electrolysers. PTLs play a crucial role in mass transport inside PEM electrolysers. A suitable PTL must ensure proper mass transport as well as electric conduction. Thus, it becomes necessary to develop an understanding of flow inside PTLs to improve electrolyser performance. A study of existing literature on PEM electrolyser modelling and simulation revealed that the PTL is one component that has not received much attention. It was also found that only a few authors have experimentally characterized two-phase flow behaviour of the PTLs. Therefore, it was aimed to measure relative permeability of the PTLs and to compare them with simulations. Pore network model was the chosen method for simulations. But it was also decided to benchmark it against other existing computational tools, namely ANSYS Fluent, GeoDict, and Palabos (LBM).

To experimentally measure absolute and relative permeability, six different PTL samples were chosen. Four were sintered from spherical titanium particles of size 45 µm, while two were sintered from irregularly shaped particles. The samples sintered from spherical particles are IEK07, IEK08, IEK90 and IEK91, and they have thicknesses 567, 507, 499 and 499 µm respectively. These were sintered at 800 °C, 800 °C, 850 °C, and 850 °C respectively. The respective porosity values are 34.5 %, 28.8 %, 27.3 % and 26.6 %. The two samples sintered from irregularly shaped particles are IEK41 and IEK44, sintered at 1000 °C with porosity of 34.3 % and 33.4 % respectively. They have thicknesses 153 µm and 387 µm respectively. Even though sintered at different temperatures, the samples IEK08, IEK90, and IEK91 had approximately the same porosities, and their measured absolute permeability values in the through-plane direction were within a very close range (70-83 mD). In-plane permeability values showed a slightly wider range (115-165 mD). Thus, these results show that when porosity values are close for the same raw material, their permeability values lie within a close range. Even though IEK07 and IEK08 are sintered at the same temperature with the same raw material, they have different porosity values, and they also differ significantly in their permeability values. The samples IEK41 and IEK44 were sintered at the same temperature from the same raw material. The thickness of IEK41 was half of IEK44, and this effect is also visible in their measured permeability values. The analysis of through-plane permeability data also show that the values of IEK07 and IEK41 have possible errors, as the measured pressure drops for different flow rates were not large enough to differentiate between intermediate points. Following the absolute permeability measurement, relative permeability was measured for IEK07, IEK08, IEK90, IEK91 and IEK44. Relative permeability in the in-plane direction could not be measured.

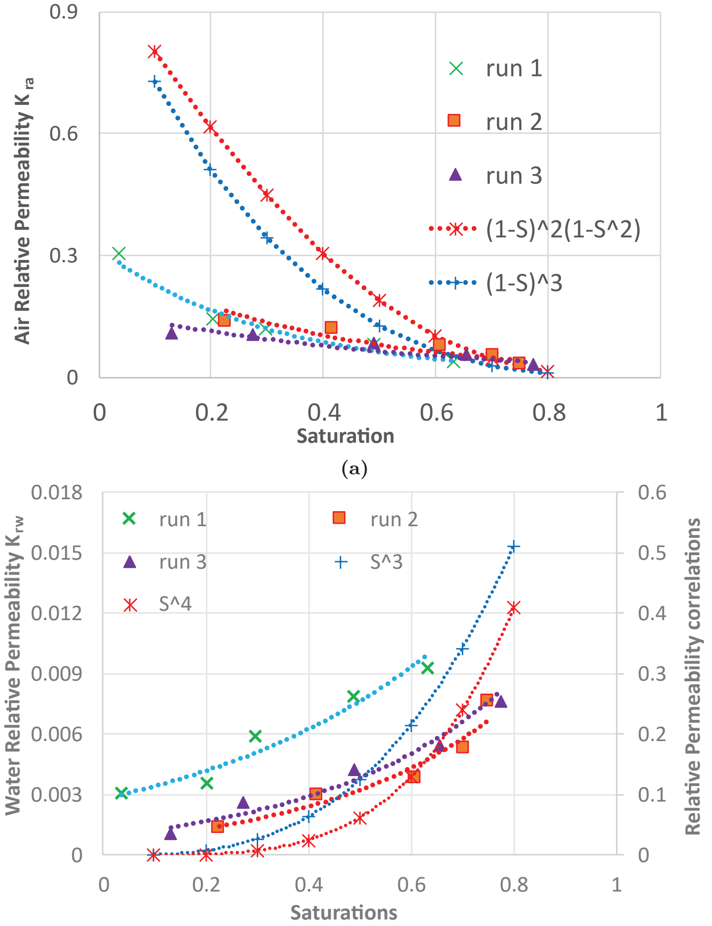

(a)

(b)

Figure 7.1: Comparison of measured relative permeability with typically used correlations from literature for the sample IEK90

From the relative permeability curves, it was observed that air relative permeability for the samples IEK07 and IEK44 decreased faster than the other three samples for the increase in water saturation. For all the samples, effective air permeability decreased to 5-10 % of the absolute permeability at around 50 % water saturation. Water effective permeability remained within 3 % of absolute permeability up to 50-60 % saturation. These values lie within a similar range for measurements done on carbon-based gas diffusion layers of fuel cells [20–22].

The experimentally measured quantities were also computed from simulations. Four different methods were tried with the pore network-based approach, and for two of them, values closer to experimental results could be computed. Except for IEK41, permeability for all other samples were under-predicted. This is an outcome of the very small thickness of the sample IEK41 pore network. However, it was noticed that the simulations did not show strong anisotropy similar to the experimental results. The distributions in Figure 6.19 prove that samples IEK08, IEK90 and IEK91 indeed have near-identical size distributions and hence exhibit similar transport properties which are also validated from experiments.

The air relative permeability curves generated from pore network simulations closely match the experimental measurements, but the water relative permeability curves show a difference. The discrepancies between experiments and simulations could be due to the fact that the simulations are quasi-dynamic and do not entirely represent the dynamic behaviour of the actual two-phase flow.

Any experimental process involves errors. The work done here is also susceptible to errors. The steady-state method of relative permeability measurement is time-consuming, and gravimetric determination of water saturation involves movement of the sample that disturbs the equilibrium. Due to time constraints, more measurements could not be carried out to rule out possible errors completely. Hence, an error analysis is not carried out.

The simulations are based on certain assumptions. Effect of changing contact angle was not studied here. It is possible to design such a scenario with a distribution of pore and throat contact angles with a mean value, but without experimental validation it would not be meaningful.

In geological studies, different relative permeability-saturation correlations exist. A list of these correlations can be found here [20, P. 48]. A comparison of the measured relative permeability curves against such correlations is shown in Figure 7.1. The figure shows that the measured values lie within the same order of magnitude as PEMFC GDL materials. Hussaini and Wang [22] have discussed that commonly used correlations do not agree to the experimentally obtained values of GDL permeability. In agreement with these authors, we also conclude that such correlations do not apply to porous materials used in PEM fuel cells or electrolysers.

Chapter 8

Conclusion

This thesis has dealt with the experimental and numerical characterization of mass transport inside PEM electrolyser porous transport layers. As a part of the work, an extensive survey of the literature was carried out to understand the state of the art. Simulations were performed with multiple software which was then validated against experiments for a number of materials. From the experiments, for the first time, relative permeability curves were produced for sintered titanium porous transport layers. These are described in the relevant chapters. In this chapter conclusions derived from the current work and the possible future work pertaining to the related problems will be discussed.

8.1 Conclusion

The extensive literature survey has shown that PTL mass transport modelling and simulation has not received much attention. Fundamental level modelling of membrane degradation or catalyst layer has only started.

The physical measurements show that PTLs sintered from irregularly shaped particles (IEK41 and IEK44) have higher porosity and permeability even though they are sintered at a much higher temperature. Experimentally measured in-plane permeability values are approximately two times larger than the through-plane permeability values. However, the simulations do not show this behaviour. This means that probably the image samples were not representative of the actual PTL material.

The simulations show that the pore networks require at least 100 layers in a given direction for the results to be independent of size. However, this cannot be guaranteed in PTLs with thicknesses in the range of 100-1000 microns. Thus, care needs to be taken during image processing and defining the boundary region.

Simulations on the artificial networks show that the effect of connectivity had a more significant influence than the size of the pores and throats for a given porosity range. SNOW network extraction with effective diameter for hydraulic conductance estimation produces results comparable to MB extraction with VB method for hydraulic conductance. The MB+VB method has been previously validated for rock samples used in the petroleum industry. A similar validation is required for PTLs used PEM electrolysers. However, the simulations on networks extracted using MB algorithm estimated permeability values closer to the experimentally measured values. But the simulations show no correlation with the experimentally determined in-plane permeability values. Relative permeability simulation assuming a wetting contact angle between water and pore surface and allowing a phase to invade a conduit, only if that phase occupies both the pores and throat, produced the most accurate relative permeability curve. The simulation results of air relative permeability closely matched with experiments, but the same could not be observed for water relative permeability.

From the simulations, it can be concluded that irregularly shaped particles produce pore structure having different directional properties. The relative permeability curves for the PTLs sintered from spherical particles look nearly identical in all directions (except for the side where boundary condition is imposed), but the other PTLs display three distinct curves with zig-gag patterns.

It is observed that relative permeability-saturation correlation from geological studies cannot be directly used for PEM electrolyser modelling without experimental validation.

8.2 Future Work

This work was concerned with the simulation of absolute and relative permeability of the porous transport layers and their validation with experimental results. The work involved multiple challenges, and in the process, scopes for future improvements were identified. Based on the experience following recommendations can be made for the future work:

- Standardization of measurement cell for determining the permeability of the PTLs is an important step. While carrying out experiments with the 5 mm diameter samples, the apparatus's size affected the measurements. Moreover, with the 20 mm diameter samples, tests were carried out only in one experimental cell. It would be beneficial to experiment with different cell designs and eliminate effects that can influence the measurements.

- Carrying out permeability measurements using different fluids is also necessary. That would finally enable to determine the absolute permeability correctly.
- Creating a repository of benchmark PTL materials, including all CT-image data, simulation data, and experimental data, would be a logical next step. This would help any future research on PTLs or similar materials.
- Validation and calibration of different simulation results with respect to the repository, as mentioned above, would be helpful for any further research in this domain.

Appendix A

Methods and Materials

A.1 Image Processing in GeoDict

Table A.1: Steps for image processing in GeoDict

Image Processing Steps	
Step	**Action**
1	Create stack in 3-D using ImageJ
2	Apply median filter
3	Apply threshold
4	Make sure that the solid part is white
5	Save as .RAW file[1]
6	Open .RAW in GeoDict and *import images*
7	Use rotate with *auto threshold* and *Suggest Full Image (Enlarge image automatically)*
8	Use crop option to crop to the desired size [2]
9	*Permute axes* to align the thinnest section along the z-axis
10	Apply threshold using the single threshold option
11	*Import Image*
12	Export .RAW from the export menu[3]
12	Use for Maximal Ball or SNOW[4]

---

[1] When a file name is written as *Filename*_LxHxS.RAW, where L=Length, H=Height, and S= no. of slices, ImageJ can automatically retrieve the details when the file is imported later on.

[2] No threshold required. Ensure that (X+20), (Y+20), and (Z+20) have prime factorisation less than 30. This is important for computation in GeoDict. It is assumed that 10 voxels are added to both inlet and outlet during computation.

[3] When exported from the 3-D image processing menu the pixels have values 0-255. When exported from export menu they have 0s and 1s

[4] Check that 0s and 1s are at the right places for both algorithms.

GeoDict offers useful preprocessing tools for the 3-D images. When the planes of the images are not correctly aligned, the rotate tool of GeoDict can be used. This greatly improves the network extraction procedure later on. The sequence of steps is shown in Table A.1.

A.2 Representative Element Volume

Table A.2: Representative Element Volume calculation

Sample	Size (Pixel)	Porosity %
IEK07	850x680x490	27.9
	600x600x490	27.8
	500x500x490	27.7
	400x400x490	27.5
	300x300x490	27.5
IEK08	792x700x455	24.1
	600x600x455	24.0
	500x500x455	24.1
	400x400x455	24.0
	300x300x455	24.1
IEK90	850x760x460	21.3
	600x600x460	21.4
	500x500x460	21.4
	400x400x460	21.3
	300x300x460	21.0
IEK91	850x700x450	24.0
	600x600x450	23.9
	500x500x450	23.8
	400x400x450	23.8
	300x300x450	23.9
IEK41	900x825x130	33.1
	600x600x130	33.2
	400x400x130	33.0
	300x300x130	32.5
IEK44	600x600x288	26.4
	500x500x288	26.5
	400x400x288	26.9
	300x300x288	26.8
	200x200x288	26.5

The determination of REV is shown in Table A.2. The change of porosity with respect to domain size was calculated to find out the smallest volume representing the material. All simulations used domain cross-section of 600x600 pixels or larger.

Appendix B

Experimental Characterization

B.1 Through-plane 20 mm diameter samples

The pressure-time plots related to the through-plane permeability measurement of 20 mm diameter samples are provided below:

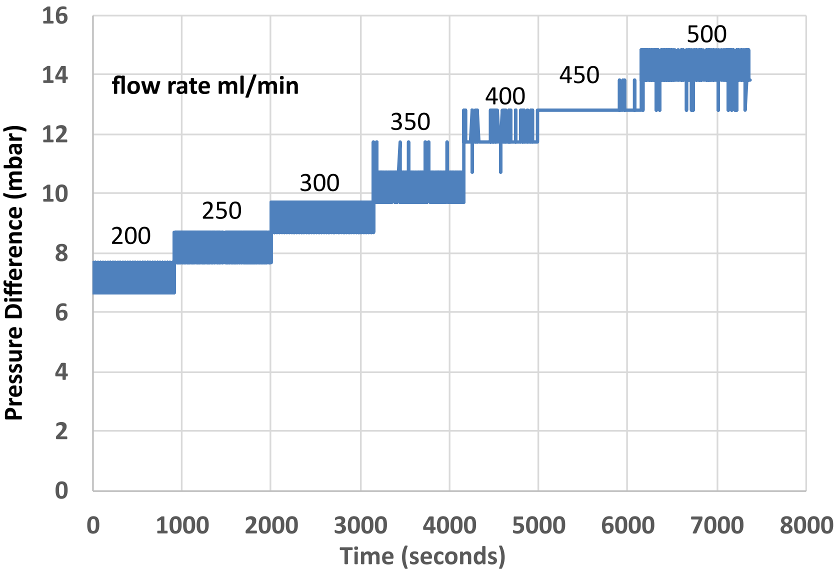

Figure B.1: IEK07 through-plane pressure-time measurement data

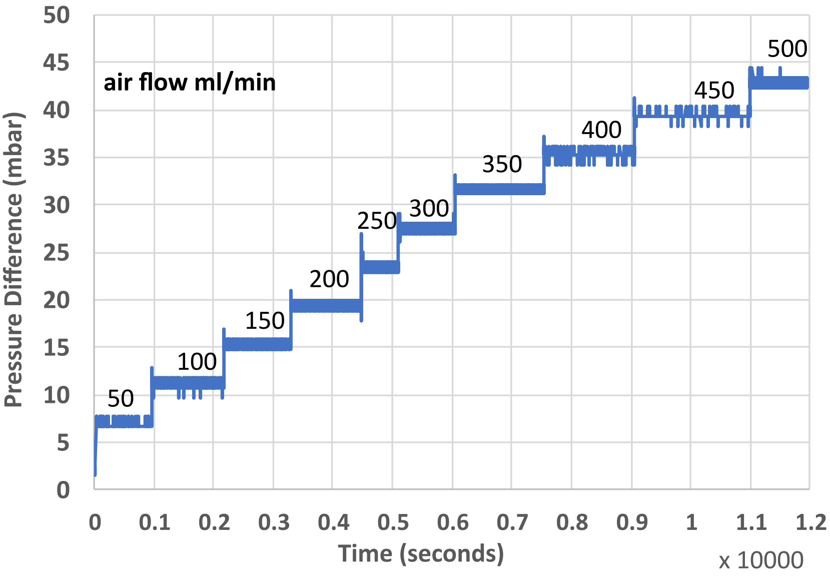

Figure B.2: IEK08 through-plane pressure-time measurement data

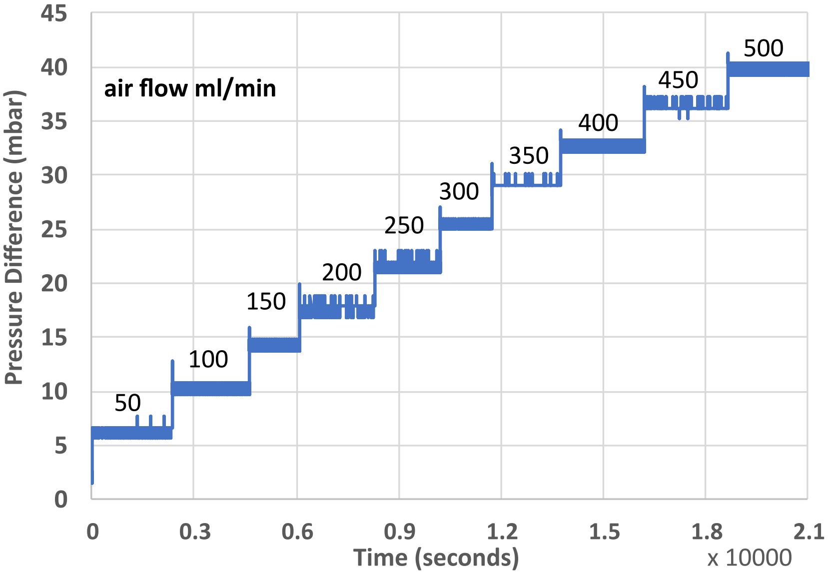

Figure B.3: IEK08 through-plane pressure-time measurement data for the repeated experiment

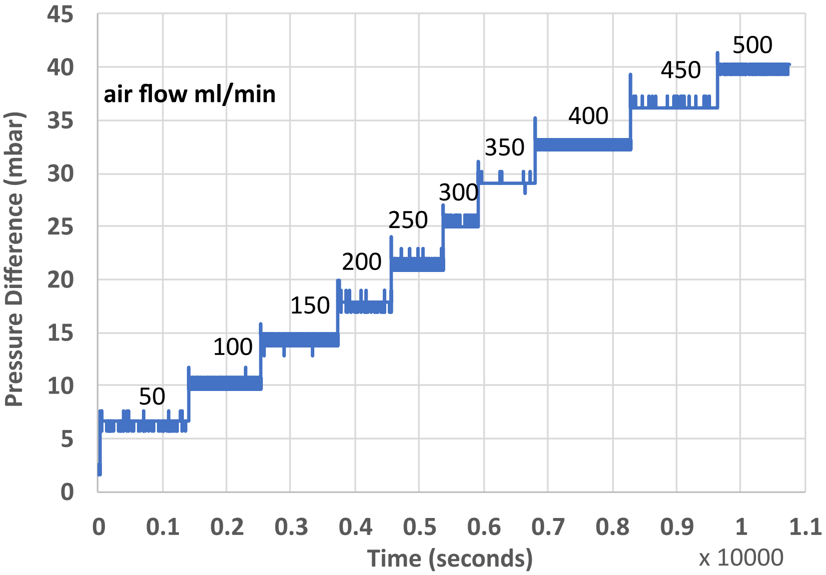

Figure B.4: IEK90 through-plane pressure-time measurement data

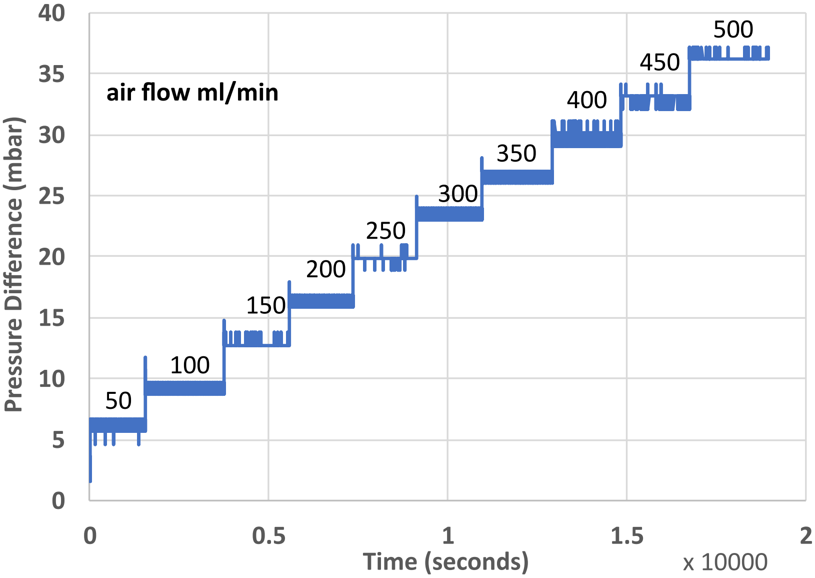

Figure B.5: IEK90 through-plane pressure-time measurement data for the repeated experiment

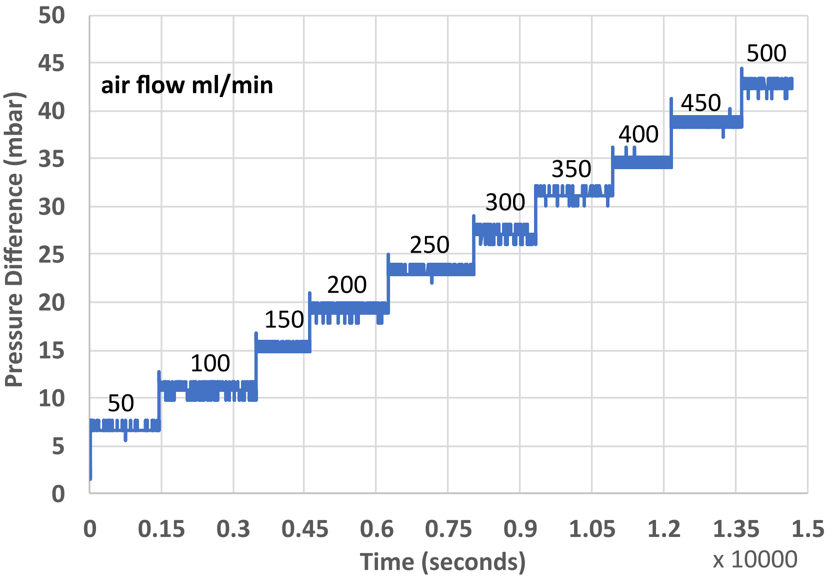

Figure B.6: IEK91 through-plane pressure-time measurement data

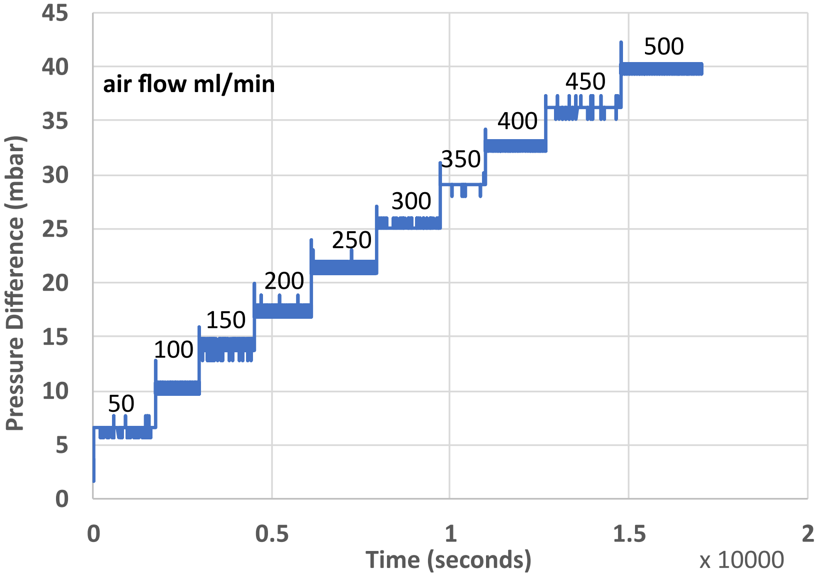

Figure B.7: IEK91 through-plane pressure-time measurement data for the repeated experiment

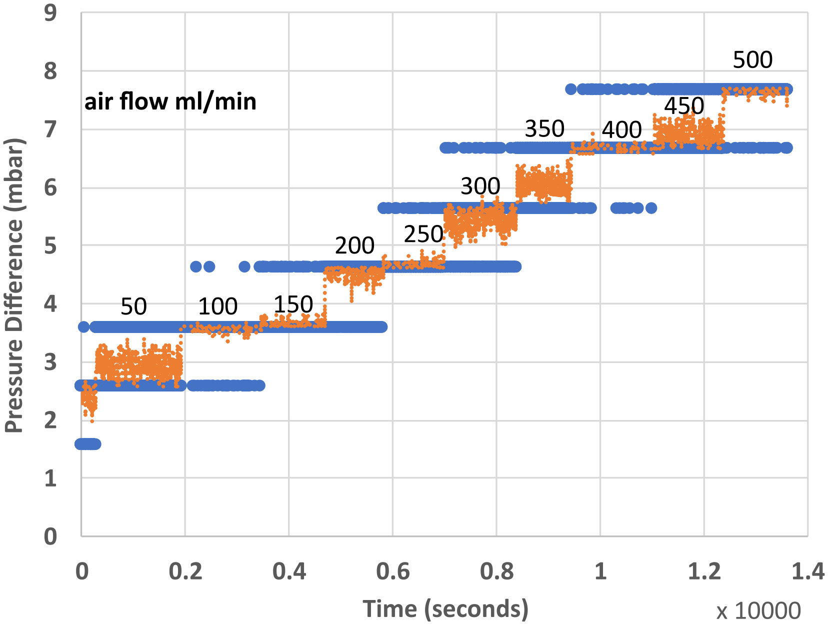

Figure B.8: IEK41 through-plane pressure-time measurement data

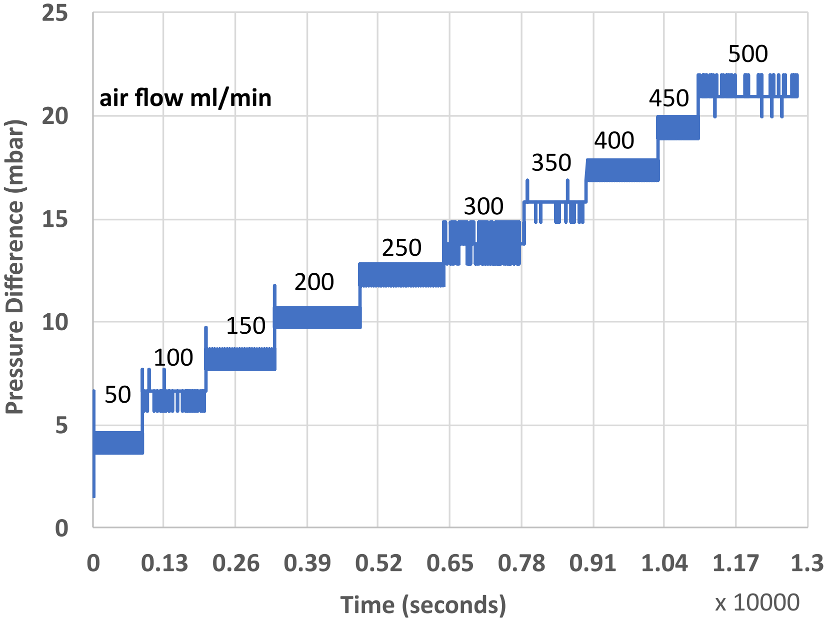

Figure B.9: IEK44 through-plane pressure-time measurement data

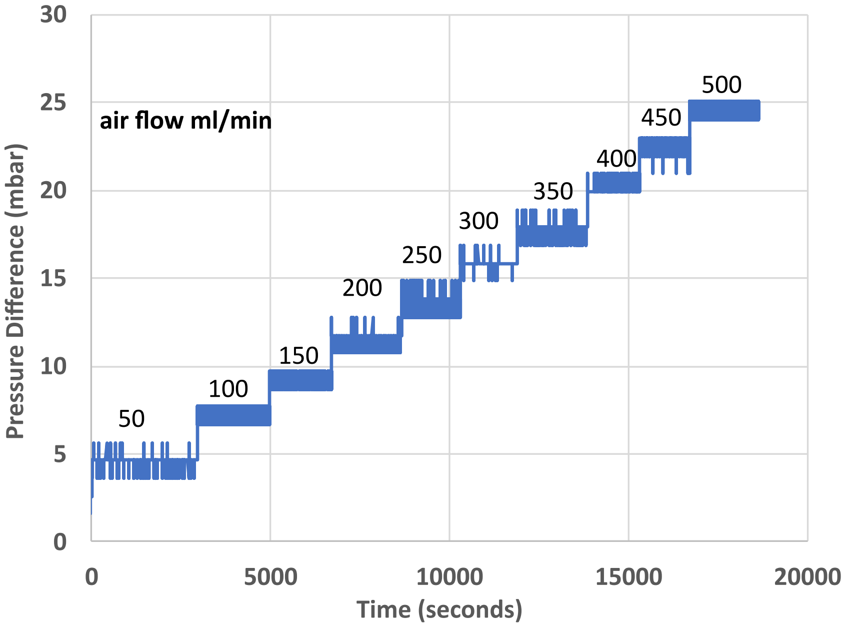

Figure B.10: IEK44 through-plane pressure-time measurement data for the repeated experiment

B.2 In-plane 20 mm diameter samples

The pressure-time plots related to the in-plane permeability measurement of 20 mm diameter samples are provided below:

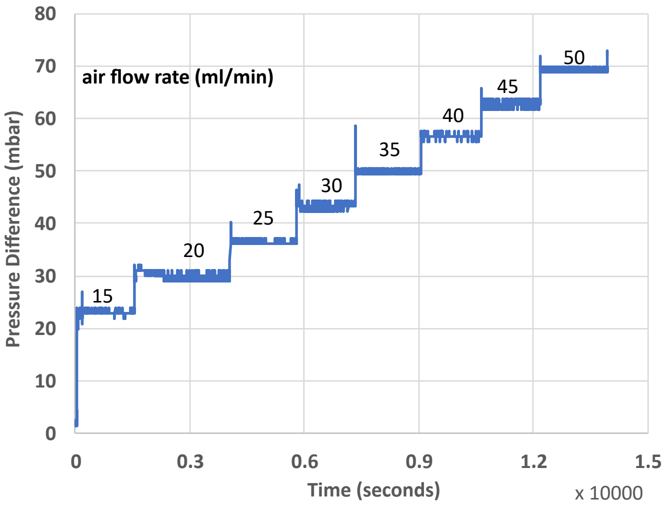

Figure B.11: IEK07 in-plane pressure-time measurement data

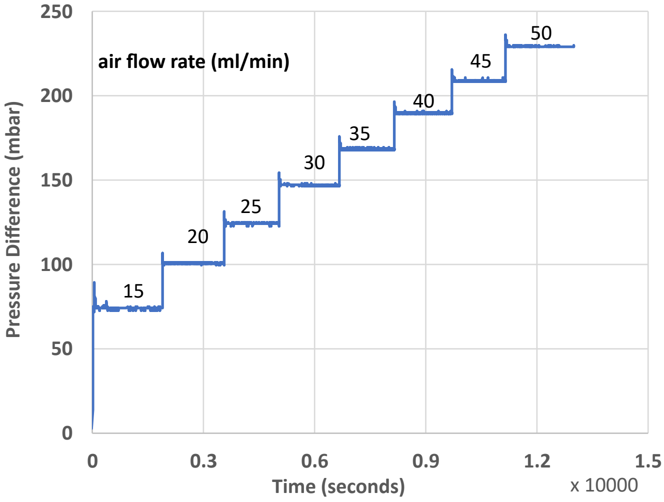

Figure B.12: IEK08 in-plane pressure-time measurement data

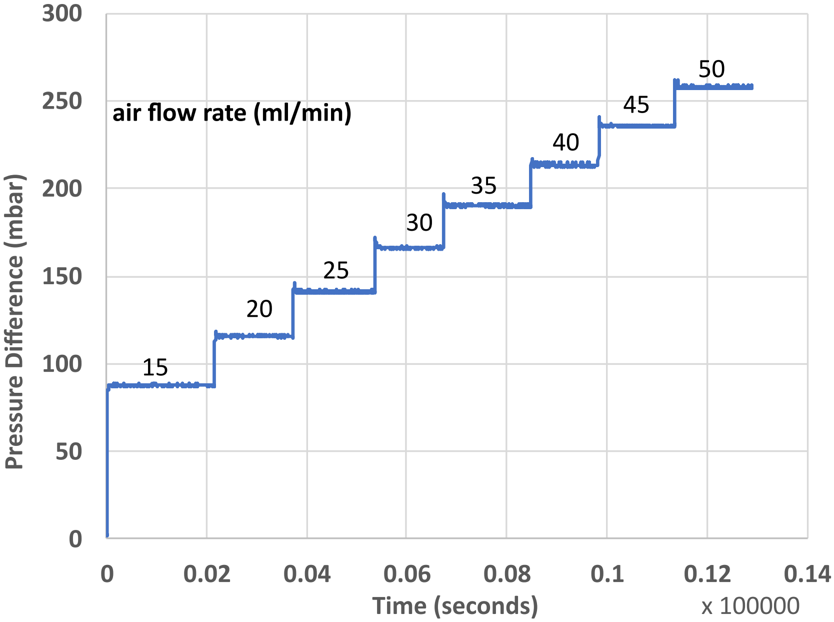

Figure B.13: IEK08 in-plane pressure-time measurement data for the repeated experiment

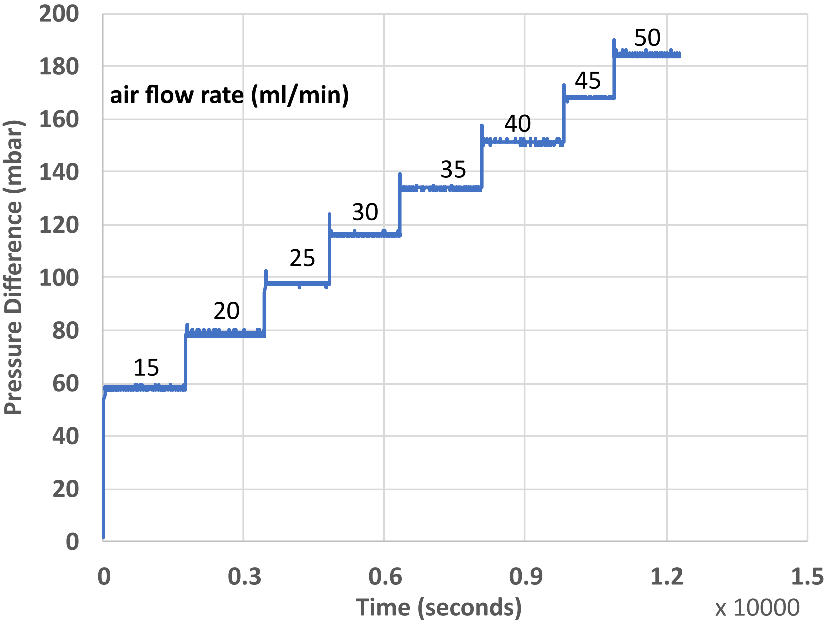

Figure B.14: IEK90 in-plane pressure-time measurement data

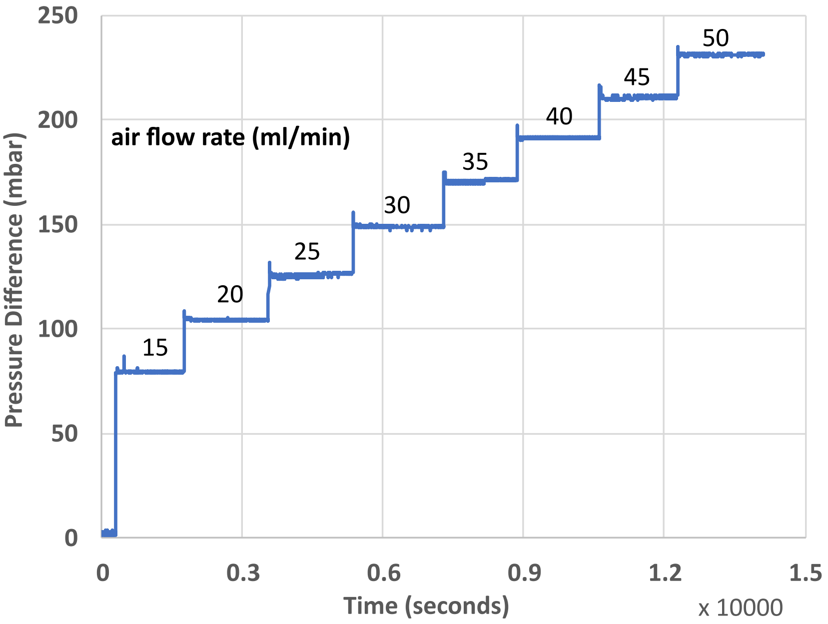

Figure B.15: IEK90 in-plane pressure-time measurement data for the repeated experiment

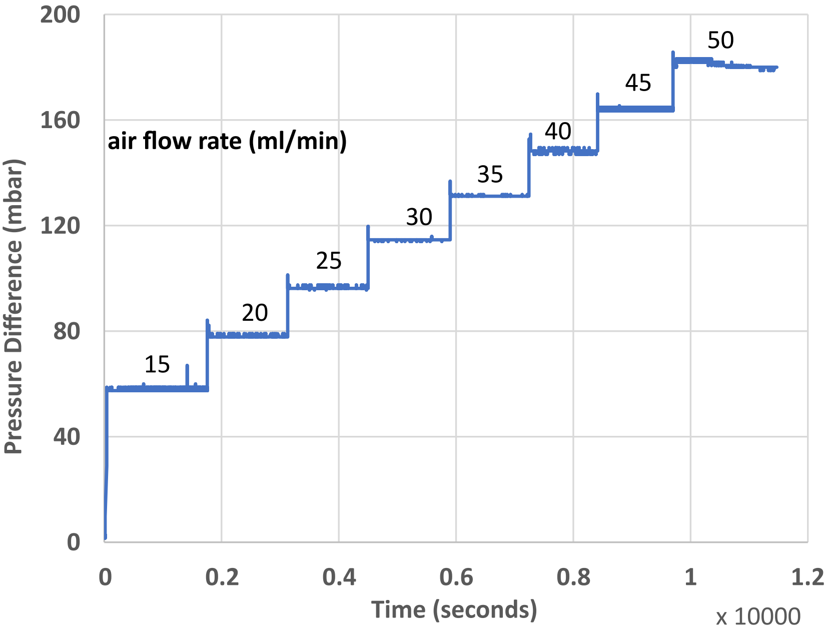

Figure B.16: IEK91 in-plane pressure-time measurement data

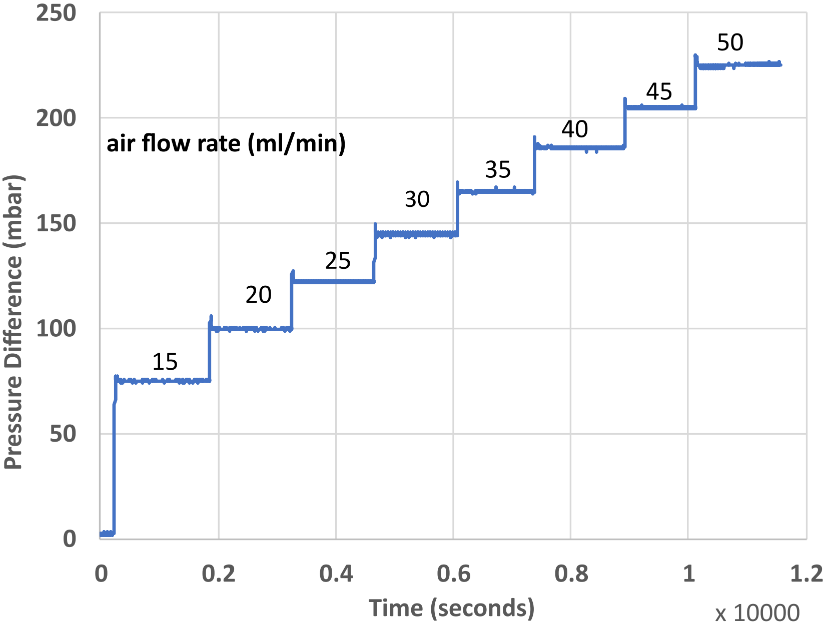

Figure B.17: IEK91 in-plane pressure-time measurement data for the repeated experiment

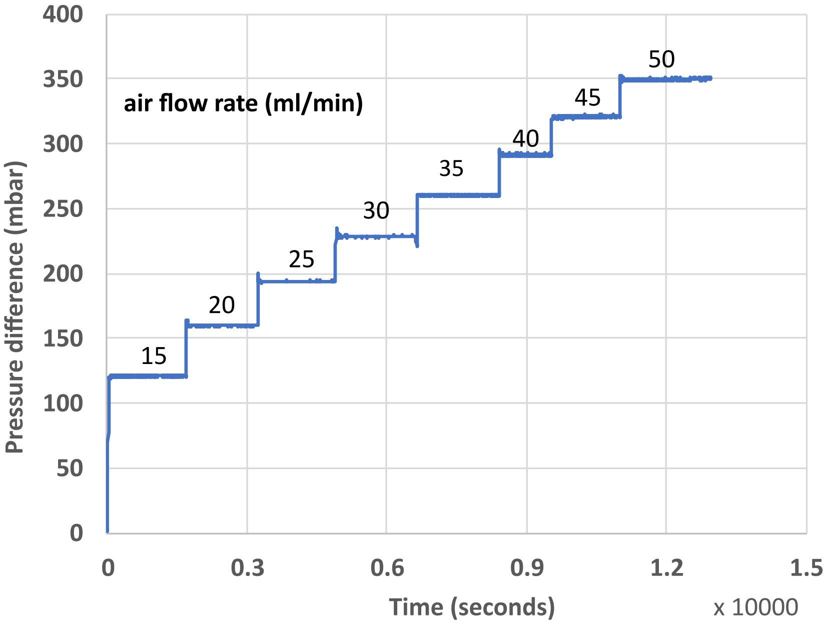

Figure B.18: IEK41 in-plane pressure-time measurement data

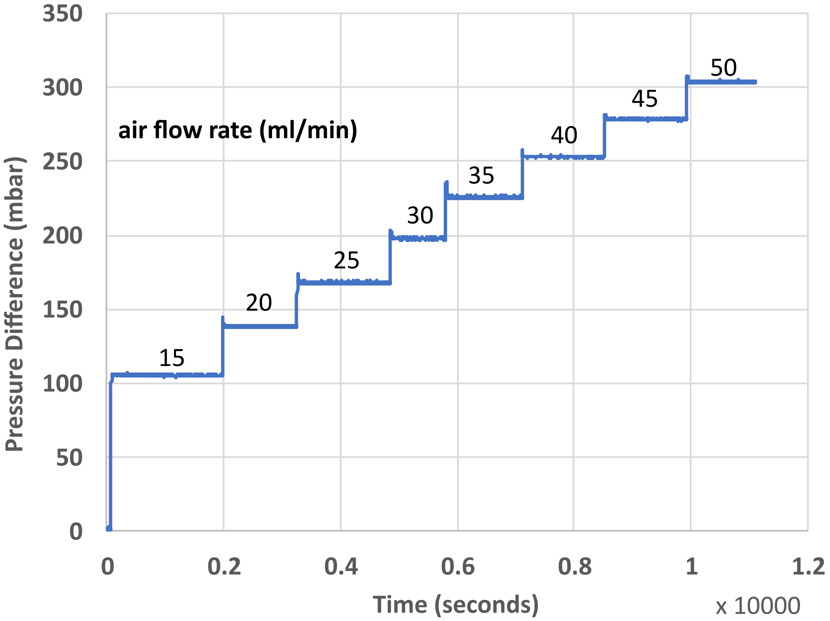

Figure B.19: IEK44 in-plane pressure-time measurement data

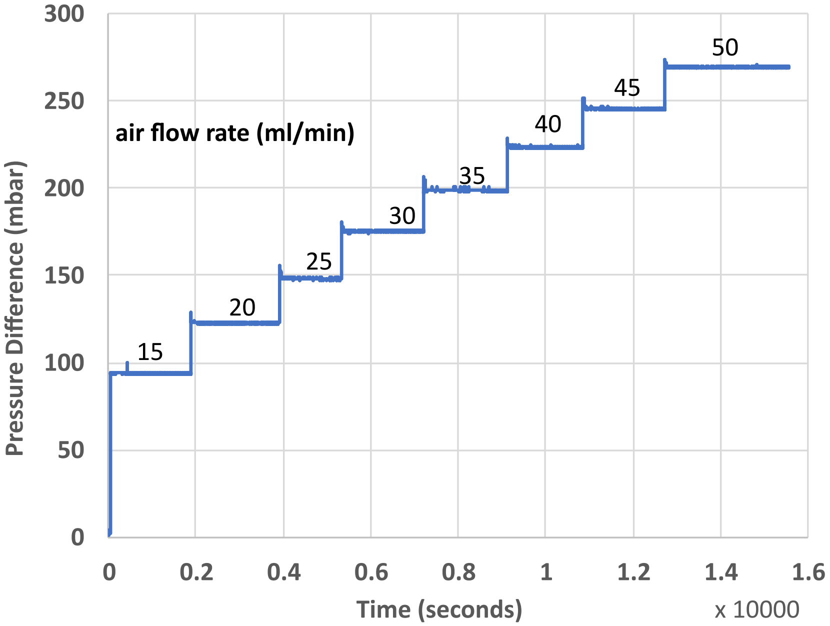

Figure B.20: IEK44 in-plane pressure-time measurement data for the repeated experiment

Appendix C

Other Experimental Measurements

C.1 Permeability Measurement with Isopropyl Alcohol

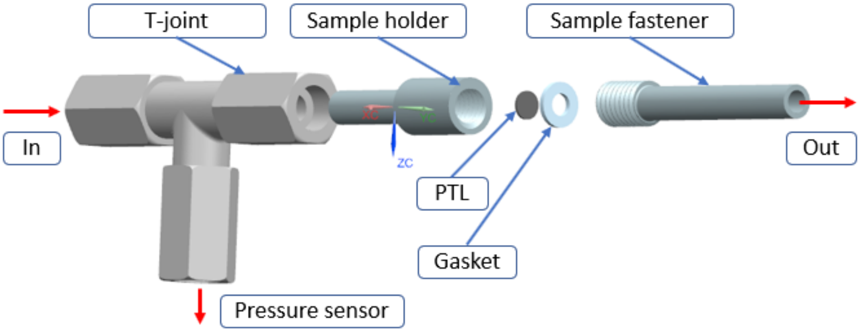

Figure C.1: Cell design 3

In chapter 5 experimental characterisation of the PTLs were described. Through-plane and in-plane permeability were measured for the 20 mm diameter samples using nitrogen gas as the working fluid. To measure permeability using a different working fluid, another test cell was constructed. This cell measured through-plane permeability using Isopropyl alcohol (IPA). The test cell is shown in Figure C.1. As there was no facility to pump IPA in large volumes, a small cell design was considered so that sufficient flow could be provided with a syringe pump.

Test Cell Description

This cell is designed for PTL samples of diameter mm. This cell has a sample holder and a sample fastener made out of aluminium. Both of them have an inner diameter of mm, and the holder has a groove of mm diameter inside which the PTL sample is placed. The fastener is then screwed into the holder after placing the gasket in between. The holder is tightly fixed on a nut that is connected to a plastic T-joint. IPA is supplied from the opposite end. The third opening of the joint is connected to a pressure transducer.

IPA Viscosity Data

Table C.1: Viscosity of IPA within the experimental temperature range. The data is obtained from [192], and a polynomial curve is fitted to interpolate between intermediate points

T[K]	T[°C]	Viscosity [mPas]	Fitted	error [%]
282.15	10	3.3079	3.3166	0.1
293	19.85	2.3810	2.3973	0.7
298.15	25	2.0120	2.0351	1.1
303.15	30	1.240	1.7596	2.1

Viscosity data of IPA is obtained from The Dortmund Data Bank [192]. Then the data is fitted with a polynomial function to interpolate within the measurement temperature range. For temperature in °C the following polynomial is fitted:

Measurement Procedure

To carry out the experiments, IPA was supplied using a KD scientific syringe pump and pressure was recorded using WIKA transducer connected to a LabVIEW data acquisition system (for details refer to Section 4.5.3). Prior to measurement the PTL samples are soaked in IPA. It is also ensured that the connected tubes are filled with IPA. Flow is changed between 0.5-1 ml/min.

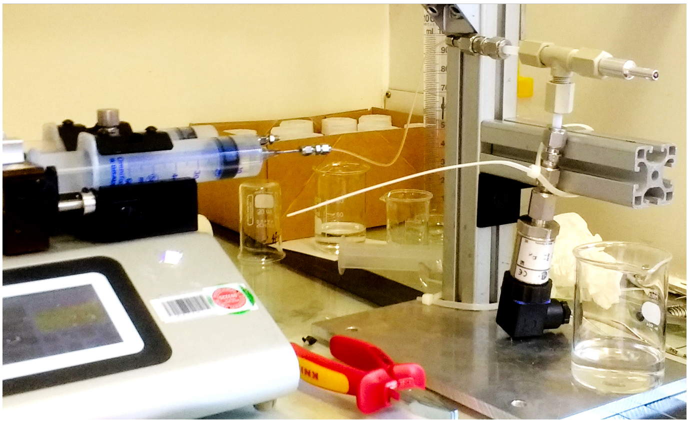

Figure C.2: Experimental setup for permeability measurement using IPA

Experimental Results

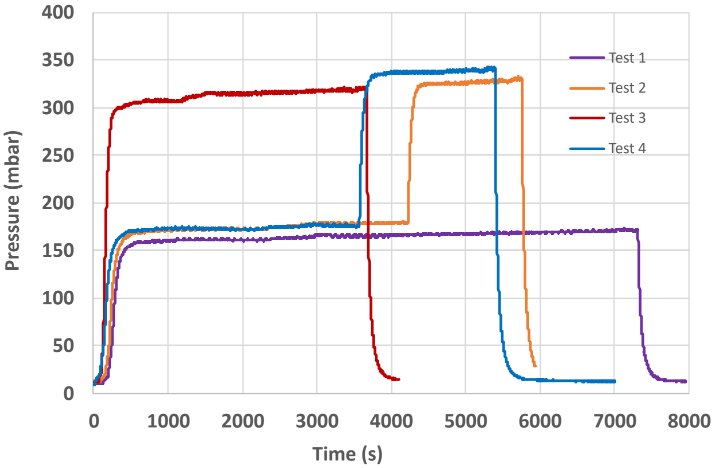

Figure C.3: Pressure-time data of IEK91 for permeability measurements using IPA. The lower lines correspond to flow rate of 0.5 ml/min, the higher lines correspond to flow rate of 1 ml/min

Through-plane permeability of IEK91 is presented in Table C.2. The corresponding pressure-time data are plotted in Figure C.3. It is observed the measured permeability changes over time for the same experiment. For this setup, the measured permeability varies between 312-364 mD. In Section 5.2.1, the same material's permeability varied between 72-77 mD in the through-plane direction. Ideally the permeability of a material should be the same irrespective of the fluid. As discussed in Section 3.2, Feser et al. [24]

Table C.2: Permeability measurement of IEK91 sample with IPA. ^{1} and ^{2} refer to permeability at the beginning and at the end of a particular flow setting, respectively. The recorded pressure shows some difference over time. Hence, two permeability values are reported here

Test	Temp [°C]	Flow [lm/min]	[mD]	[mD]
1	23	0.5	364	346
2	24	0.5	327	312
2	24	1.0	341	340
3	22	0.5	371	355
4	22	0.5	353	328
4	23	1.0	344	342

measured the same permeability for water and gas while Dohle et al. [156] reported having measured different values. The results presented here need further investigation.

Bibliography

[1] Joan M Ogden. Prospects for building a hydrogen energy infrastructure. *Annu. Rev. Energy Environ*, 24:227–279, 1999.

[2] L. Barreto, A. Makihira, and K. Riahi. The hydrogen economy in the 21st century: a sustainable development scenario. *International Journal of Hydrogen Energy*, 28 (3):267–284, 2003. doi: 10 1016/S0360-3199(02)00074-5.

[3] G. W. Crabtree, Mildred S. Dresselhaus, and Michelle V. Buchanan. The hydrogen economy. *Physics Today*, 57(12):39–44, 2004. doi: 10 1063/1 1878333.

[4] J.M. Ogden. Hydrogen - the fuel of the future? *Physics Today*, 55(4):69–75, 2002. doi: 10 1063/1 1480785.

[5] Seth Dunn. Hydrogen futures: Toward a sustainable energy system. *International Journal of Hydrogen Energy*, 27(3):235–264, 2002. doi: 10 1016/S0360-3199(01)00131-8.

[6] G.W. Crabtree and M.S. Dresselhaus. The Hydrogen Fuel Alternative. *MRS Bulletin*, 33(04):421–428, 2008. doi: 10 1557/mrs2008 84.

[7] P. P. Edwards, V. L. Kuznetsov, W. I F David, and N. P. Brandon. Hydrogen and fuel cells: Towards a sustainable energy future. *Energy Policy*, 36(12):4356–4362, 2008. doi: 10 1016/j enpol 2008 09 036.

[8] Sunita Sharma and Sib Krishna Ghoshal. Hydrogen the future transportation fuel: From production to applications. 43:1151–1158, 2015. doi: 10 1016/ j rser 2014 11 093.

[9] Joan M. Ogden. Cost and performance sensitivity studies for solar photovoltaic/-electrolytic hydrogen systems. *Solar Cells*, 30(1-4):515–523, 1991. doi: 10 1016/ 0379-6787(91)90082-Z.

[10] Joan Ogden. High Hopes for Hydrogen. *Scientific American*, 295(3):94–1901, 2006.

[11] Victor A. Goltsov and T. Nejat Veziroglu. From hydrogen economy to hydrogen civilization. *International Journal of Hydrogen Energy*, 26(9):909–915, 2001. doi: 10 1016/S0360-3199(01)00045-3.

[12] Victor A. Goltsov and T. Nejat Veziroglu. A step on the road to Hydrogen Civilization. *International Journal of Hydrogen Energy*, 27(7-8):719–723, 2002. doi: 10 1016/S0360-3199(01)00122-7.

[13] V. A. Goltsov, T. N. Veziroglu, and L. F. Goltsova. Hydrogen civilization of the future - A new conception of the IAHE. *International Journal of Hydrogen Energy*, 31(2):153–159, 2006. doi: 10 1016/j ijhydene 2005 04 045.

[14] Kerry Ann Adamson. Hydrogen from renewable resources-the hundred year commitment. *Energy Policy*, 32(10):1231–1242, 2004. doi: 10 1016/S0301-4215(03)00094-6.

[15] Alfredo Ursua, Luis M. Gandia, and Pablo Sanchis. Hydrogen Production From Water Electrolysis : Current Status and Future Trends. In *Proceedings of the IEEE*, volume 100, pages 410–426, 2012. doi: doi:10 1109/JPROC 2011 2156750.

[16] S Trasatti. Water electrolysis: who first? *Journal of Electroanalytical Chemistry*, 476(1):90–91, 1999. doi: 10 1016/s0022-0728(99)00364-2.

[17] Marcelo Carmo, David L. Fritz, Jürgen Mergel, and Detlef Stolten. A comprehensive review on PEM water electrolysis. *International Journal of Hydrogen Energy*, 38(12): 4901–4934, 2013. doi: 10 1016/j ijhydene 2013 01 151.

[18] W. Dönitz and E. Erdle. High-temperature electrolysis of water vapor- status of development and perspectives for application. *International Journal of Hydrogen Energy*, 10(5):191–295, 1985.

[19] J. H. Russel, L. J. Nuttall, and A. P. Fickett. Hydrogen Generation by Solid Polymer Electrolyte Water Electrolysis. In *Paper presented at American Chemical Society Division of Fuel Chemistry Meeting*, pages 24–40, 1973.

[20] Joshua David Sole. *Investigation of Water Transport Parameters and Processes in the Gas Diffusion Layer of PEM Fuel Cells.* PhD thesis, Virginia Polytechnic Institute, 2008.

[21] I. S. Hussaini and C. Y. Wang. Experimental Measurement of Relative Permeability Functions for Fuel Cell GDL Materials. *ECS Transactions*, 25(1):1539–1550, 2009.

[22] I S Hussaini and C Y Wang. Measurement of relative permeability of fuel cell diffusion media. *Journal of Power Sources*, 195:3830–3840, 2010. doi: 10 1016/ j jpowsour 2009 12 105.

[23] Jeff T. Gostick, Michael W. Fowler, Mark D. Pritzker, Marios A. Ioannidis, and Leya M. Behra. In-plane and through-plane gas permeability of carbon fiber electrode backing layers. *Journal of Power Sources*, 162(1):228–238, 2006. doi: 10 1016/j jpowsour 2006 06 096.

[24] J. P. Feser, A. K. Prasad, and S. G. Advani. Experimental characterization of in-plane permeability of gas diffusion layers. *Journal of Power Sources*, 162(2 SPEC. ISS.):1226–1231, 2006. doi: 10 1016/j jpowsour 2006 07 058.

[25] Stefan Dwenger. *Transport interactions between gas and water in thin hydrophobic porous layers*. PhD thesis, 2016.

[26] Chung Hyuk Lee, James Hinebaugh, Rupak Banerjee, Stephane Chevalier, Rami Abouatallah, Rainey Wang, and Aimy Bazylak. Influence of limiting throat and flow regime on oxygen bubble saturation of polymer electrolyte membrane electrolyzer porous transport layers. *International Journal of Hydrogen Energy*, 44:2724–2735, 2017. doi: 10 1016/j ijhydene 2016 09 114.

[27] Michael Andreas Höh. *Poröse Transportschichten für die Polymerelektrolytmembran-Wasserelektrolyse*. PhD thesis, RWTH Acchen University, 2017.

[28] Asier Goñi-Urtiaga, Dimitrios Presvytes, and Keith Scott. Solid acids as electrolyte materials for proton exchange membrane (PEM) electrolysis: Review. *International Journal of Hydrogen Energy*, 37(4):3358–3372, 2012. doi: 10 1016/ j ijhydene 2011 09 152.

[29] Guoqiang Wei, Li Xu, Chengde Huang, and Yuxin Wang. SPE water electrolysis with SPEEK/PES blend membrane. *International Journal of Hydrogen Energy*, 35 (15):7778–7783, 2010. doi: 10 1016/j ijhydene 2010 05 041.

[30] S. S. Ivanchev. Fluorinated proton-conduction nafion-type membranes, the past and the future. *Russian Journal of Applied Chemistry*, 81(4):569–584, 2008. doi: 10 1134/s1070427208040010.

[31] Wu Xu and Keith Scott. The effects of ionomer content on PEM water electrolyser membrane electrode assembly performance. *International Journal of Hydrogen Energy*, 35(21):12029–12037, 2010. doi: 10 1016/j ijhydene 2010 08 055.

[32] A. Damjanovic, A. Dey, and J. O.M. Bockris. Kinetics of oxygen evolution and dissolution on platinum electrodes. *Electrochimica Acta*, 11(7):791–814, 1966. doi: 10 1016/0013-4686(66)87056-1.

[33] Mark D. Symes and Leroy Cronin. Decoupling hydrogen and oxygen evolution during electrolytic water splitting using an electron-coupled-proton buffer. *Nature Chemistry*, 5(5):403–409, 2013. doi: 10 1038/nchem 1621.

[34] Ho Young Jung, Sheng Yang Huang, Prabhu Ganesan, and Branko N. Popov. Performance of gold-coated titanium bipolar plates in unitized regenerative fuel cell operation. *Journal of Power Sources*, 194(2):972–975, 2009. doi: 10 1016/ j jpowsour 2009 06 030.

[35] Tom Smolinka, Emile Ojong, and Thomas Lickert. Fundamentals of PEM Water Electrolysis. In D. Bessarabov, editor, *PEM Electrolysis for Hydrogen Production*, pages 11–33. CRC Press, first edition, 2015. doi: 10 1201/b19096-3.

[36] Michel Suermann, Thomas J. Schmidt, and Felix N. Büchi. Investigation of Mass Transport Losses in Polymer Electrolyte Electrolysis Cells Michel Suermann. *ECS Transactions*, 69(17):1141–1148, 2015. doi: 10 1149/06917 1141ecst.

[37] Henry Darcy. *Les fontaines publiques de la ville de Dijon.* 1856.

[38] G. O. Brown. Henry Darcy and the making of a law. *Water Resources Research*, 38 (7):11–1–11–12, 2002. doi: 10 1029/2001wr000727.

[39] W. Sobieski and A. Trykozko. Darcy's and Forchheimer's laws in practice. Part 1. The experiment. *Technical Sciences / University of Warmia and Mazury in Olsztyn*, nr 17(4)(4):321–335, 2014.

[40] Vishal A Jambhekar. Forchheimer Porous-media Flow Models - Numerical Investigation and Comparison with Experimental Data. *Master Dissertation*, (November): 85, 2011. doi: 10 1080/10942910600853774.

[41] Douglas Ruth and Huiping Ma. On the derivation of the Forchheimer equation by means of the averaging theorem. *Transport in Porous Media*, 7(3):255–264, 1992. doi: 10 1007/BF01063962.

[42] Stephen Whitaker. The Forchheimer equation: A theoretical development. *Transport in Porous Media*, 25(1):27–61, 1996. doi: 10 1007/BF00141261.

[43] P. Forchheimer. Wasserbewegung durch boden. *Zeitschrift des Vereines Deutscher Ingenieuer*, 45, 1901.

[44] H. Teng and T. S. Zhao. An extension of Darcy's law to non-Stokes flow in porous media. *Chemical Engineering Science*, 55:2727–2735, 2000.

[45] Donald A. Nield and Adrian Bejan. *Convection in porous media.* Springer, fifth edition, 2017. doi: 10 1007/978-3-319-49562-0.

[46] Melina G. Sidiropoulou, Konstadinos N. Moutsopoulos, and Vassilios A. Tsihrintzis. Determination of Forchheimer equation coefficients a and b. *Hydrological Processes*, 21:534–554, 2007.

[47] Masoud Ziabasharhagh, Faezeh Mosallat, and Mohammad Reza Shahnazari. Experimental Investigation of the Permeability and Inertial Effect on Fluid Flow through Homogeneous Porous Media. *Iranian Journal of Chemistry and Chemical Engineering*, 27(2):33–38, 2008.

[48] Sabri Ergun and A. A. Orning. Fluid Flow through Randomly Packed Columns and Fluidized Beds. *Industrial & Engineering Chemistry*, 1949. doi: 10 1021/ie50474a011.

[49] Sabri Ergun. Fluid Flow Through Packed Columns. 48:89–94, 1952.

[50] F. A. L. Dullien. *Porous Media: Fluid Transport and Pore Structure.* Academic Press Inc., second edition, 1992. doi: 10 1016/0300-9467(81)80049-4.

[51] E. W. Washburn. Note on a Method of Determining the Distribution of Pore Sizes in a Porous Material. *Proceedings of the National Academy of Sciences*, 1921. doi: 10 1073/pnas 7 4 115.

[52] A. Fick. Ueber Diffusion. *Analan der Physik*, 94(1):59–86, 1855. doi: 10 1002/andp 18551700105.

[53] Suhas. V. Patankar. *Numerical Heat Transfer and Fluid Flow.* Hemisphere Publishing Corporation, 1980. doi: 10 13182/nse81-a20112.

[54] *ANSYS FLUENT Theory Guide 14.5.* ANSYS Inc., 2012.

[55] M. Ishii and K. Mishima. Two-fluid Model and Hydrodynamic Constitutive Relations. *Nuclear Engineering and Design*, 82(2-3):107–126, 1984. doi: 10 1016/0029-5493(84)90207-3.

[56] Christopher E. Brennen. *Fundamentals of Multiphase Flows.* Cambridge University Press, 2005.

[57] Mikko Manninen and Veikko Taivassalo. *On the mixture model for multiphase flow.* VTT Publications, 1996.

[58] Kai Hiltunen, Sirpa Kallio, Hannu Karema, Markku Kataja, Antti Koponen, Mikko Manninen, and Veikko Taivassalo. *Multiphase Flow Dynamics: Theory and Numerics*, volume 722. VTT Publications, 2009.

[59] C. W. Hirt and B. D. Nichols. Volume of Fluid (VOF) Method for the Dynamics of Free Boundaries. *Journal of Computational Physics*, 39:201–225, 1981. doi: 10 1016/0021-9991(81)90145-5.

[60] J. U. Brackbill, D. B. Kothe, and C. Zemach. A Continuum Method for Modeling Surface Tension. *Journal of Computational Physics*, 100(2):335–354, 1992. doi: 10 1016/0021-9991(92)90240-Y.

[61] Denis Gueyffier, Jie Li, Ali Nadim, Ruben Scardovelli, and Stéphane Zaleski. Volume-of-Fluid Interface Tracking with Smoothed Surface Stress Methods for Three-Dimensional Flows. *Journal of Computational Physics*, 152:423–456, 1999. doi: 10 1006/jcph 1998 6168.

[62] Ali Q Raeini, Martin J Blunt, and Branko Bijeljic. Modelling two-phase flow in porous media at the pore scale using the volume-of-fluid method. *Journal of Computational Physics*, 231(17):5653–5668, 2012. doi: 10 1016/j jcp 2012 04 011.

[63] Georg May. Numerical Methods for Partial Differential Equations. Lecture Notes, RWTH Aachen University, 2013.

[64] J. Hardy, O. De Pazzis, and Y. Pomeau. Molecular dynamics of a classical lattice gas: Transport properties and time correlation functions. *Physical Review A*, 1976. doi: 10 1103/PhysRevA 13 1949.

[65] Uriel Frisch, Dominique D'humieres, Brosl Hasslacher, Pierre Lallemand, Y Ves Pomeau, and Jean-Pierre R Ivet. Lattice Gas Hydrodynamics in Two and Three Dimensions. *Complex Systems*, 1:649–707, 1987.

[66] U. Frisch, B. Hasslacher, and Y. Pomeau. Lattice-Gas Automata for the Navier-Stokes Equation. 56(14):1505–1508, 1986.

[67] Guy R. McNamara and Gianluigi Zanetti. Use of the Boltzmann Equation to Simulate Lattice-Gas Automata. *Physical Review Letters*, 61(20):2332–2335, 1988. doi: 10 1103/PhysRevLett 61 2332.

[68] F. J. Higuera and J. Jiménez. Boltzmann Approach to Lattice Gas Simulations. *EPL*, 9, 1989. doi: 10 1209/0295-5075/9/7/009.

[69] Y. H. Qian, D. D'Humières, and P. Lallemand. Lattice bgk models for navier-stokes equation. *Epl*, 17(6):479–484, 1992. ISSN 12864854. doi: 10 1209/0295-5075/17/6/001.

[70] Joerg Bernsdorf. *Simulation of Complex Flows and Multi-Physics with the Lattice-Boltzmann Method*. PhD thesis, University of Amsterdam, 2008.

[71] Hu Dong and Martin J. Blunt. Pore-network extraction from micro-computerized-tomography images. *Physical Review E - Statistical, Nonlinear, and Soft Matter Physics*, 80(3):1–11, 2009. doi: 10 1103/PhysRevE 80 036307.

[72] Jeff T. Gostick. Versatile and efficient pore network extraction method using marker-based watershed segmentation. *Physical Review E*, 96(2):1–15, 2017. doi: 10 1103/PhysRevE 96 023307.

[73] Jeff Gostick, Mahmoudreza Aghighi, James Hinebaugh, Tom Tranter, Michael A Hoeh, Harold Day, Brennan Spellacy, Mostafa Sharqawy, Aimy Bazylak, Alans Burns, Werner Lehnert, and Andreas Putz. OpenPNM: A Pore Network Modeling Package. *Computing in Science and Engineering*, 48:60–74, 2016.

[74] Varvara Sygouni, Christos D. Tsakiroglou, and Alkiviades C. Payatakes. Capillary pressure spectrometry: Toward a new method for the measurement of the fractional wettability of porous media. *Physics of Fluids*, 18(5):053302, 2006. doi: 10 1063/1 2203667.

[75] David Wilkinson and Jorge F. Willemsen. Invasion percolation: a new form of percolation theory. *Journal of Physics A: Mathematical and General*, 16(14):3365–3376, 1983.

[76] Mathieu Jurgawczynski. *PREDICTING ABSOLUTE AND RELATIVE PERMEABILITIES OF CARBONATE ROCKS USING IMAGE ANALYSIS AND EFFECTIVE MEDIUM THEORY.* PhD thesis, Imperial College London, 2007.

[77] P. Millet. Water Electrolysis Using EME Technology: Temperature Profile inside a Nafion Membrane During Electrolysis. *Electrochimica Acta*, 36(2):263–267, 1991. doi: 10 1016/0013-4686(91)85247-5.

[78] A. B. Goldberg, L. I. Kheifets, A. G. Vaganov, S. G. Ogryz'ko-zhoukovskaya, and A. V. Shabalin. A hydrodynamic model for water decomposition in electrolyzers with a solid polymer electrolyte. *Journal of Applied Electrochemistry*, 22:1147–1154, 1992.

[79] Pyoungho Choi, Dmitri G. Bessarabov, and Ravindra Datta. A simple model for solid polymer electrolyte (SPE) water electrolysis. *Solid State Ionics*, 175(1-4):535–539, 2004. doi: 10 1016/j ssi 2004 01 076.

[80] Meng Ni, Michael K H Leung, and Dennis Y C Leung. Electrochemistry Modeling of Proton Exchange Membrane (PEM) Water Electrolysis for Hydrogen Production. In *WHEC 16*, pages 1–7, 2006.

[81] K W Harrison, E Hernandez-Pacheco, M Mann, and H Salehfar. Semiempirical model for determining PEM electrolyzer stack characteristics. *Journal Of Fuel Cell Science And Technology*, 3(2):220–223, 2006. doi: 10 1115/1 2174072.

[82] R. García-Valverde, C. Miguel, R. Martínez-Béjar, and A. Urbina. Optimized photovoltaic generator-water electrolyser coupling through a controlled DC-DC converter. *International Journal of Hydrogen Energy*, 33(20):5352–5362, 2008. doi: 10 1016/j ijhydene 2008 06 015.

[83] Francisco da Costa Lopes and Edson H. Watanabe. Experimental and theoretical development of a PEM electrolyzer model applied to energy storage systems. *2009 Brazilian Power Electronics Conference*, (2):775–782, 2009. doi: 10 1109/COBEP 2009 5347619.

[84] Alhassan Salami Tijani and Mohd Ariffuddin Haiyoon. Simulation Analysis of the Effect of Temperature and Exchange Current Density on Power and Hydrogen Production of (PEM) Electrolyzer. *Applied Mechanics and Materials*, 660(2014):411–415, 2014.

[85] F. Marangio, M. Santarelli, and M. Calì. Theoretical model and experimental analysis of a high pressure PEM water electrolyser for hydrogen production. *International Journal of Hydrogen Energy*, 34(3):1143–1158, 2009. doi: 10 1016/ j ijhydene 2008 11 083.

[86] D. L. Fritz, J. Mergel, and D. Stolten. PEM Electrolysis Simulation and Validation. *ECS Transactions*, 58(19):1–9, 2014. doi: 10 1149/05819 0001ecst.

[87] Bo Han, Stuart M. Steen, Jingke Mo, and Feng-Yuan Zhang. Electrochemical performance modeling of a proton exchange membrane electrolyzer cell for hydrogen energy. *International Journal of Hydrogen Energy*, 40(22):7006–7016, 2015. doi: 10 1016/j ijhydene 2015 03 164.

[88] Z. Abdin, C. J. Webb, and E. Maca Gray. Modelling and simulation of a proton exchange membrane (PEM) electrolyser cell. *International Journal of Hydrogen Energy*, 40(39):13243–13257, 2015. doi: 10 1016/j ijhydene 2015 07 129.

[89] Bo Han, Jingke Mo, Zhenye Kang, Gaoqiang Yang, William Barnhill, and Feng Yuan Zhang. Modeling of two-phase transport in proton exchange membrane electrolyzer cells for hydrogen energy. *International Journal of Hydrogen Energy*, 42 (7):4478–4489, 2017. ISSN 03603199. doi: 10 1016/j ijhydene 2016 12 103.

[90] Ishanka Dedigama, Kathy Ayers, Paul R. Shearing, and Daniel J L Brett. An experimentally validated steady state polymer electrolyte membrane water electrolyser model. *International Journal of Electrochemical Science*, 9(5):2662–2681, 2014.

[91] Abdul Hadi Abdol Rahim and Alhassan Tijani. Simulation Analysis of the Effect of Temperature on Overpotentials in PEM Electrolyzer System. *Journal of Mechanical Engineering*, 12(1):47–65, 2015.

[92] M. E. Lebbal and S. Lecœuche. Identification and monitoring of a PEM electrolyser based on dynamical modelling. *International Journal of Hydrogen Energy*, 34(14): 5992–5999, 2009. doi: 10 1016/j ijhydene 2009 02 003.

[93] R. García-Valverde, N. Espinosa, and A. Urbina. Simple PEM water electrolyser model and experimental validation. *International Journal of Hydrogen Energy*, 37 (2):1927–1938, 2012. doi: 10 1016/j ijhydene 2011 09 027.

[94] Houcheng Zhang, Shanhe Su, Guoxing Lin, and Jincan Chen. Efficiency Calculation and Configuration Design of a PEM Electrolyzer System for Hydrogen Production. *International Journal of Electrochemical Science*, 7(5):4143–4157, 2012.

[95] A. Awasthi, Keith Scott, and S. Basu. Dynamic modeling and simulation of a proton exchange membrane electrolyzer for hydrogen production. *International Journal of Hydrogen Energy*, 36(22):14779–14786, 2011. doi: 10 1016/j ijhydene 2011 03 045.

[96] Massimo Guarnieri, Piergiorgio Alotto, and Federico Moro. Modeling the performance of hydrogen-oxygen unitized regenerative proton exchange membrane fuel cells for energy storage. *Journal of Power Sources*, 297:23–32, 2015. doi: 10 1016/j jpowsour 2015 07 067.

[97] Dawn M Bernardi, Mark W Verbrugge, J Electrochem Soc, Dawn M Bernardi, and Mark W Verbrugge. Fuel Cell A Mathematical Model of the Solid-Polymer-Electrolyte Fuel Cell. *Journal of Electrochemical Society*, 139(9):2477–2491, 1992. doi: 10 1149/1 2221251.

[98] Shanthi P. Katukota, Jianhu Nie, Yitung Chen, Robert F. Boehm, and Hsuan Tsung Hsieh. Numerical Modeling of Electrochemical Process for Hydrogen Production from PEM Electrolyzer Cell. In *Proceedings of the Energy Sustainability Conference 2007*, 2007. doi: 10 1115/ES2007-36108.

[99] Haluk Görgün. Dynamic modelling of a proton exchange membrane (PEM) electrolyzer. *International Journal of Hydrogen Energy*, 31(1):29–38, 2006. doi: 10 1016/j ijhydene 2005 04 001.

[100] T E Springer, T A Zawodzinski, and S Gottesfeld. Polymer Electrolyte Fuel Cell Model. *Journal of The Electrochemical Society*, 138(8):2334–2342, 1991. doi: 10 1149/1 2085971.

[101] M. Chandesris, V. Médeau, N. Guillet, S. Chelghoum, D. Thoby, and F. Fouda-Onana. Membrane degradation in PEM water electrolyzer: Numerical modeling and experimental evidence of the influence of temperature and current density. *International Journal of Hydrogen Energy*, 40(3):1353–1366, 2015. doi: 10 1016/j ijhydene 2014 11 111.

[102] S. Busquet, C. E. Hubert, J. Labbé, D. Mayer, and R. Metkemeijer. A new approach to empirical electrical modelling of a fuel cell, an electrolyser or a regenerative fuel cell. *Journal of Power Sources*, 134(1):41–48, 2004. ISSN s. doi: 10 1016/j jpowsour 2004 02 018.

[103] C. Marr and X. Li. An engineering model of proton exchange membrane fuel cell performance. *ARI - An International Journal for Physical and Engineering Sciences*, 50(4):190–200, 1998. doi: 10 1007/s007770050014.

[104] P. Millet. Water Electrolysis Using EME Technology: Electric Potential Distribution inside a Nafion Membrane during Electrolysis. *Electrochimica Acta*, 39(17): 2501–2506, 1994. doi: 10 1016/0013-4686(94)00261-4.

[105] Kazuo Onda, Toshio Murakami, Takeshi Hikosaka, Misaki Kobayashi, Ryouhei Notu, and Kohei Ito. Performance Analysis of Polymer-Electrolyte Water Electrolysis Cell at a Small-Unit Test Cell and Performance Prediction of Large Stacked Cell. *Journal of The Electrochemical Society*, 149(8):A1069, 2002. doi: 10 1149/1 1492287.

[106] S. Kélouwani, K. Agbossou, and R. Chahine. Model for energy conversion in renewable energy system with hydrogen storage. *Journal of Power Sources*, 140(2): 392–399, 2005. doi: 10 1016/j jpowsour 2004 08 019.

[107] M. J. Khan and M. T. Iqbal. Dynamic modeling and simulation of a small wind-fuel cell hybrid energy system. *Renewable Energy*, 30(3):421–439, 2005. doi: 10 1016/ j renene 2004 05 013.

[108] Jianhu Nie, Yitung Chen, and Robert F. Boehm. Numerical modeling of two-phase flow in a bipolar plate of a PEM electrolyzer cell. In *Proceedings of the ASME IMECE2008*, volume 10, pages 36–46, Boston, 2008. ISBN 01496115. doi: 10 1393/ ncr/i2004-10001-9. URL http://www epjap org/10 1051/epjap/2012110475.

[109] Jianhu Nie, Jianfei Wu, Steve Cohen, Blake Carter, and Yitung Chen. Numerical Simulations of Coupled Flow and Heat Transfer Distributions in a Bipolar Plate of

the PEM Electrolysis Cell. In *2008 ASME Fluids Engineering Conference*, pages 733–739, 2008.

[110] Jianhu Nie, Yitung Chen, Robert F. Boehm, and Shanthi Katukota. A photoelectrochemical model of proton exchange water electrolysis for hydrogen production. In *Journal of Heat Transfer*, 2008. doi: 10 1115/1 2789722.

[111] Xiaojin Li, Shuguo Qu, Hongmei Yu, Ming Hou, Zhigang Shao, and Baolian Yi. Membrane water-flow rate in electrolyzer cells with a solid polymer electrolyte (SPE). *Journal of Power Sources*, 190(2):534–537, 2009. doi: 10 1016/j jpowsour 2008 12 147.

[112] Jephanya Kasukurthi, K. M. Veepuri, Jianhu Nie, and Yitung Chen. Numerical Modeling of Velocity and Temperature Distributions in a Bipolar Plate of PEM Electrolysis Cell with Greatly Improved Flow Uniformity. In *ASME 2009 International Mechanical Engineering Congress and Exposition*, pages 595–601, 2009. doi: 10 1115/IMECE2009-10519.

[113] Jianhu Nie, Yitung Chen, Steve Cohen, Blake D. Carter, and Robert F. Boehm. Numerical and experimental study of three-dimensional fluid flow in the bipolar plate of a PEM electrolysis cell. *International Journal of Thermal Sciences*, 48(10): 1914–1922, 2009. doi: 10 1016/j ijthermalsci 2009 02 017.

[114] S. A. Grigoriev, A. A. Kalinnikov, P. Millet, V. I. Porembsky, and V. N. Fateev. Mathematical modeling of high-pressure PEM water electrolysis. *Journal of Applied Electrochemistry*, 40(5):921–932, 2010. doi: 10 1007/s10800-009-0031-z.

[115] P. Medina and M. Santarelli. Analysis of water transport in a high pressure PEM electrolyzer. *International Journal of Hydrogen Energy*, 35(11):5173–5186, 2010. doi: 10 1016/j ijhydene 2010 02 130.

[116] Jianhu Nie and Yitung Chen. Numerical modeling of three-dimensional two-phase gas-liquid flow in the flow field plate of a PEM electrolysis cell. *International Journal of Hydrogen Energy*, 35(8):3183–3197, 2010. doi: 10 1016/j ijhydene 2010 01 050.

[117] Özcan Atlam. A small scale education experiment kit with wind generator-PEM electrolyser system and modelling. *Turkish Journal of Electrical Engineering and Computer Sciences*, 18(4):583–595, 2010. doi: 10 3906/elk-0812-18.

[118] Steffen Becker and Vishy Karri. Predictive models for PEM-electrolyzer performance using adaptive neuro-fuzzy inference systems. *International Journal of Hydrogen Energy*, 35(18):9963–9972, 2010. ISSN 03603199. doi: 10 1016/j ijhydene 2009 11 060. URL `http://dx doi org/10 1016/j ijhydene 2009 11 060`.

[119] Steffen Becker and Vishy Karri. Implementation of neural network models for parameter estimation of a PEM-electrolyzer. *Journal of Advanced Computational Intelligence and Intelligent Informatics*, 14(6):735–740, 2010.

[120] K. S. Agbli, M. C. Péra, D. Hissel, O. Rallires, C. Turpin, and I. Doumbia. Multiphysics simulation of a PEM electrolyser: Energetic Macroscopic Representation approach. *International Journal of Hydrogen Energy*, 36(2):1382–1398, 2011. doi: 10 1016/j ijhydene 2010 10 069.

[121] Ozcan Atlam and Mohan Kolhe. Equivalent electrical model for a proton exchange membrane (PEM) electrolyser. *Energy Conversion and Management*, 52 (8-9):2952–2957, 2011. doi: 10 1016/j enconman 2011 04 007.

[122] Timothy D. Myles, George J. Nelson, Aldo A. Peracchio, Robert J. Roy, Bryan L. Murach, Gary A. Adamson, and Wilson K. S. Chiu. Species transport in a high-pressure oxygen-generating proton-exchange membrane electrolyzer. *International Journal of Hydrogen Energy*, 37(17):12451–12463, 2012. doi: 10 1016/ j ijhydene 2012 05 123.

[123] Luiz Fernando L. Oliveira, Slimane Laref, Eric Mayousse, Christian Jallut, and Alejandro a. Franco. A multiscale physical model for the transient analysis of PEM water electrolyzer anodes. *Physical Chemistry Chemical Physics*, 14(29):10215, 2012. doi: 10 1039/c2cp23300b.

[124] Maximilian Schalenbach, Marcelo Carmo, David L. Fritz, Jürgen Mergel, and Detlef Stolten. Pressurized PEM water electrolysis: Efficiency and gas crossover. *International Journal of Hydrogen Energy*, 38(35):14921–14933, 2013. doi: 10 1016/ j ijhydene 2013 09 013.

[125] Bonghwan Lee, Kiwon Park, and Hyung Man Kim. Dynamic simulation of PEM water electrolysis and comparison with experiments. *International Journal of Electrochemical Science*, 8(1):235–248, 2013.

[126] Pouria Ahmadi, Ibrahim Dincer, and Marc A. Rosen. Energy and exergy analyses of hydrogen production via solar-boosted ocean thermal energy conversion and PEM electrolysis. *International Journal of Hydrogen Energy*, 38(4):1795–1805, 2013. doi: 10 1016/j ijhydene 2012 11 025.

[127] Luiz Fernando L Oliveira, Christian Jallut, and Alejandro A. Franco. A multiscale physical model of a polymer electrolyte membrane water electrolyzer. *Electrochimica Acta*, 110:363–374, 2013. doi: 10 1016/j electacta 2013 07 214.

[128] F. Z. Aouali, M. Becherif, A. Tabanjat, M. Emziane, K. Mohammedi, S. Krehi, and A. Khellaf. Modelling and experimental analysis of a PEM electrolyser powered by a solar photovoltaic panel. *Energy Procedia*, 62(0):714–722, 2014. doi: 10 1016/j egypro 2014 12 435.

[129] Nabil Tlili, Bechir Neily, and Fatma Ben Salem. Modeling and simulation of hybrid system coupling a photovoltaic generator, a PEM fuel cell and an electrolyzer (Part II). *2014 IEEE 11th International Multi-Conference on Systems, Signals and Devices, SSD 2014*, (Part II):1–7, 2014. doi: 10 1109/SSD 2014 6808808.

[130] Anissia Beainy, Nabil Karami, and Nazih Moubayed. Simulink model for a PEM electrolyzer based on an equivalent electrical circuit. *2014 International Conference on Renewable Energies for Developing Countries, REDEC 2014*, pages 145–149, 2014. doi: 10 1109/REDEC 2014 7038547.

[131] Ekin Özgirgin, Yılser Devrim, and Ayhan Albostan. Modeling and simulation of a hybrid photovoltaic (PV) module-electrolyzer-PEM fuel cell system for micro-cogeneration applications. *International Journal of Hydrogen Energy*, 40(44): 15336–15342, 2015. doi: 10 1016/j ijhydene 2015 06 122.

[132] Yılser Devrim and Kübra Pehlivanoğlu. Design of a hybrid photovoltaic-electrolyzer-PEM fuel cell system for developing solar model. *Physica Status Solidi (C)*, 12(9-11): 1256–1261, 2015. doi: 10 1002/pssc 201510091.

[133] Alhassan Salami Tijani and A. H. Abdol Rahim. Numerical Modeling the Effect of Operating Variables on Faraday Efficiency in PEM Electrolyzer. *Procedia Technology*, 26:419–427, 2016. doi: 10 1016/j protcy 2016 08 054.

[134] Anders Christian Olesen, Carsten Rømer, and Søren Knudsen Kær. A numerical study of the gas-liquid, two-phase flow maldistribution in the anode of a high pressure PEM water electrolysis cell. *International Journal of Hydrogen Energy*, 41(1):52–68, 2016. doi: 10 1016/j ijhydene 2015 09 140.

[135] Tevfik Yigit and Omer Faruk Selamet. Mathematical modeling and dynamic Simulink simulation of high-pressure PEM electrolyzer system. *International Journal of Hydrogen Energy*, 41(32):13901–13914, 2016. doi: 10 1016/j ijhydene 2016 06 022.

[136] Brahim Laoun, Abdallah Khellaf, Mohamed W. Naceur, and Arunachala M. Kannan. Modeling of solar photovoltaic-polymer electrolyte membrane electrolyzer direct coupling for hydrogen generation. *International Journal of Hydrogen Energy*, 41(24): 10120–10135, 2016. doi: 10 1016/j ijhydene 2016 05 041.

[137] Blal Mohamed, Benattilah Alli, and Bellassri Ahmed. Using the hydrogen for sustainable energy storage: Designs, modeling, identification and simulation membrane behavior in PEM system electrolyser. *Journal of Energy Storage*, 7:270–285, 2016. doi: 10 1016/j est 2016 06 006.

[138] P. Olivier, C. Bourasseau, and B. Bouamama. Modelling, simulation and analysis of a PEM electrolysis system. *IFAC-PapersOnLine*, 49(12):1014–1019, 2016. doi: 10 1016/j ifacol 2016 07 575.

[139] Saeed Sadeghi Lafmejani, Anders Christian Olesen, and Søren Knudsen Kær. VOF modelling of gas-liquid flow in PEM water electrolysis cell micro-channels. *International Journal of Hydrogen Energy*, 42(26):16333–16344, 2017. doi: 10 1016/ j ijhydene 2017 05 079.

[140] Saeed Sadeghi Lafmejani, Martin Müller, Anders Christian Olesen, and Søren Knudsen Kær. Experimental and numerical study of flow in expanded metal plate for water electrolysis applications. *Journal of Power Sources*, 397(February):334–342, 2018. doi: 10 1016/j jpowsour 2018 07 032.

[141] Guillaume Fontès. *Modèlisation et caractérisation de la pile PEM pour l'étude des interactions avec les convertisseurs statiques.* PhD thesis, L'INSTITUT NATIONAL POLYTECHNIQUE DE TOULOUSE, 2005.

[142] Maximilian Schalenbach. Corrigendum: Pressurized PEM water electrolysis: Efficiency and gas crossover (Int J Hydrogen Energy (2013) 38 (14921-14933)). *International Journal of Hydrogen Energy*, 41(1):729–732, 2016. doi: 10 1016/ j ijhydene 2015 11 009.

[143] Rui B. Ferreira, D. S. Falcão, V. B. Oliveira, and A. M. F. R. Pinto. Numerical simulations of two-phase flow in proton exchange membrane fuel cells using the volume of fluid method - A review. *Journal of Power Sources*, 277:329–342, 2015. doi: 10 1016/j jpowsour 2014 11 124.

[144] S. S. Lafmejani, A. C. Olesen, and S. K. Kaer. Analysing Gas-Liquid Flow in PEM Electrolyser Micro-Channels S. *ECS Transactions*, 75(14):1121–1127, 2016.

[145] Alejandro A. Franco, Pascal Schott, Christian Jallut, and Bernhard Maschke. A Dynamic Mechanistic Model of an Electrochemical Interface. *Journal of The Electrochemical Society*, 153(6):A1053–A1061, 2006. doi: 10 1149/1 2188353.

[146] A. A. Franco, P. Schott, C. Jallut, and B. Maschke. A multi-scale dynamic mechanistic model for the transient analysis of PEFCs. *Fuel Cells*, 7(2):99–117, 2007. doi: 10 1002/fuce 200500204.

[147] Alejandro A. Franco, Universite Claude, and Bernard Lyon. *A multiscale modeling framework for the transient analysis of PEM Fuel Cells From the fundamentals to the engineering practice*. PhD thesis, Universite Claude Bernard Lyon 1, 2010.

[148] Jeff T Gostick, Marios A Ioannidis, Michael W Fowler, and Mark D Pritzker. Pore network modeling of fibrous gas diffusion layers for polymer electrolyte membrane fuel cells. *Journal of Power Sources*, 173:277–290, 2007. doi: 10 1016/ j jpowsour 2007 04 059.

[149] J. T. Gostick. Random pore network modeling of GDLs using Voronoi and Delaunay Tessellations. *ECS Transactions*, 41(1):125–130, 2011.

[150] Jeff T Gostick. Random Pore Network Modeling of Fibrous PEMFC Gas Diffusion Media Using Voronoi and Delaunay Tessellations. *Journal of The Electrochemical Society*, 160(F731-F743), 2013. doi: 10 1149/2 009308jes.

[151] Jeff T. Gostick and Adam Z. Weber. Resistor-Network Modeling of Ionic Conduction in Polymer Electrolytes Jeff. *Electrochimica Acta*, 179:137–145, 2015. doi: 10 1016/ j electacta 2015 03 126.

[152] M. Aghighi and J.T. Gostick. Pore network modeling of the full membrane electrode assembly of a polymer electrolyte membrane fuel cell. *ECS Transactions*, 64(3): 19–25, 2014.

[153] Mahmoudreza Aghighi, Michael A Hoeh, Werner Lehnert, Geraldine Merle, and Jeff Gostick. Simulation of a Full Fuel Cell Membrane Electrode Assembly Using Pore Network Modeling. *Journal of The Electrochemical Society*, 163(5):384–392, 2016. doi: 10 1149/2 0701605jes.

[154] P. Lettenmeier, S. Kolb, F. Burggraf, A. S. Gago, and K. A. Friedrich. Towards developing a backing layer for proton exchange membrane electrolyzers. *Journal of Power Sources*, 311:153–158, 2016. doi: 10 1016/j jpowsour 2016 01 100.

[155] K. S. Agbli, D. Hissel, M. C. Péra, and Issa Doumbia. Energetic Macroscopic Representation (EMR): New approach for multiphysics energetic flows modelling. *IFAC Proceedings Volumes (IFAC-PapersOnline)*, 8(PART 1):723–728, 2012. doi: 10 3182/20120902-4-fr-2032 00126.

[156] H. Dohle, R. Jung, N. Kimiaie, J. Mergel, and M. Müller. Interaction between the diffusion layer and the flow field of polymer electrolyte fuel cells - Experiments and simulation studies. *Journal of Power Sources*, 124(2):371–384, 2003. doi: 10 1016/ S0378-7753(03)00800-0.

[157] Minkmas V. Williams, Eric Begg, Leonard Bonville, H. Russel Kunz, and James M. Fenton. Characterization of gas diffusion layers for PEMFC. *Journal of Electrochemical Society*, 151(8):A1173–A1180, 2004. doi: 10 1016/j electacta 2008 02 057.

[158] Jari Ihonen, Mikko Mikkola, and Göran Lindbergh. Flooding of Gas Diffusion Backing in PEFCs. *Journal of The Electrochemical Society*, 151(8):A1152, 2004. doi: 10 1149/1 1763138.

[159] M. Prasanna, H. Y. Ha, E. A. Cho, S. A. Hong, and I. H. Oh. Influence of cathode gas diffusion media on the performance of the PEMFCs. *Journal of Power Sources*, 131(1-2):147–154, 2004. doi: 10 1016/j jpowsour 2004 01 030.

[160] Vladimir Gurau, Michael J. Bluemle, Emory S. De Castro, Yu Min Tsou, Thomas A. Zawodzinski, and J. Adin Mann. Characterization of transport properties in gas diffusion layers for proton exchange membrane fuel cells. 2. Absolute permeability. *Journal of Power Sources*, 165(2):793–802, 2007. doi: 10 1016/ j jpowsour 2006 12 068.

[161] Mehdi Honarpour, Leonard Koederitz, and A. Herbert Harvey. *Relative Permeability of Petroleum Reservoirs.* CRC Press, 1986.

[162] E. F. Johnson, D. P. Bossler, and V.O. Naumann. Calculation of Relative Permeability from Displacement Experiments. *TRANSACTIONS OF THE AMERICAN INSTITUTE OF MINING AND METALLURGICAL ENGINEERS*, 216(2):370–372, 1959. doi: 10 1393/ncr/i2004-10001-9.

[163] T. V. Nguyen, Guangyu Lin, Heebong Ohn, Dan Hussey, David Jacobson, and Muhammad Arif. Measurements of Two-Phase Flow Properties of the Porous Media Used in PEM Fuel Cells. *ECS Transactions*, 3(1):415–423, 2006. doi: 10 1149/ 1 2356162.

[164] Bladimir Ramos-Alvarado, Joshua D. Sole, Abel Hernandez-Guerrero, and Michael W. Ellis. Experimental characterization of the water transport properties of PEM fuel cells diffusion media. *Journal of Power Sources*, 218:221–232, 2012. doi: 10 1016/j jpowsour 2012 05 069.

[165] Andreas Putz, James Hinebaugh, Mahmoudreza Aghighi, Harold Day, Aimy Bazylak, and Jeff Gostick. Introducing OpenPNM: An Open Source Pore Network Modeling Software Package. *ECS Transactions*, 58(1):79–86, 2013.

[166] Jonas Latt, Orestis Malaspinas, Andrea Parmigiani, and Federico Brogi. Palabos, parallel lattice Boltzmann solver. *Preprint*, (October), 2019. doi: 10 13140/ RG 2 2 20836 94086.

[167] Dieter Froning, Jan Brinkmann, Uwe Reimer, Volker Schmidt, Werner Lehnert, and Detlef Stolten. 3D analysis, modeling and simulation of transport processes in compressed fibrous microstructures, using the Lattice Boltzmann method. *Electrochimica Acta*, 110:325–334, 2013. doi: 10 1016/j electacta 2013 04 071.

[168] Dieter Froning, Gerd Gaiselmann, Uwe Reimer, Jan Brinkmann, Volker Schmidt, and Werner Lehnert. Stochastic Aspects of Mass Transport in Gas Diffusion Layers. *Transport in Porous Media*, 103(3):469–495, 2014. doi: 10 1007/s11242-014-0312-9.

[169] Dieter Froning, Junliang Yu, Gerd Gaiselmann, Uwe Reimer, Ingo Manke, Volker Schmidt, and Werner Lehnert. Impact of compression on gas transport in non-woven gas diffusion layers of high temperature polymer electrolyte fuel cells. *Journal of Power Sources*, 318:26–34, 2016. doi: 10 1016/j jpowsour 2016 03 102.

[170] A. Wiegmann. Computation of the permeability of porous materials from their microstructure by FFF-Stokes. Technical Report 129, Fraunhofer ITWM, 2007.

[171] A. Wiegmann and A. Zemitis. EJ-HEAT: A Fast Explicit Jump Harmonic Averaging Solver for the Effective Heat Conductivity of Composite Materials. Technical Report 94, Fraunhofer (ITWM), 2006.

[172] Volker Paul Schulz, Jürgen Becker, Andreas Wiegmann, Partha P. Mukherjee, and Chao Yang Wang. Modeling of two-phase behavior in the gas diffusion medium of PEFCs via full morphology approach. *Journal of the Electrochemical Society*, 154 (4), 2007. doi: 10 1149/1 2472547.

[173] T.W. Ridler and S. Calvard. Picture Thresholding Using an Iterative Method. *IEEE Transactions on Systems, Man and Cybernetics*, smc-8(8):630–632, 1978.

[174] Per H. Valvatne and Martin J. Blunt. Predictive pore-scale modeling of two-phase flow in mixed wet media. *Water Resources Research*, 40(7):1–21, 2004. doi: 10 1029/ 2003WR002627.

[175] Per Henrik Valvatne. *PREDICTIVE PORE-SCALE MODELLING OF MULTI-PHASE FLOW.* PhD thesis, Imperial College London, 2004.

[176] A. Boujelben. *A New Pore-Scale Numerical Simulator for Investigating Special Core Analysis Data.* PhD thesis, Hariot-Watt University, 2017.

[177] Ali Reza Khaz'ali and Jamshid Moghadasi. Capillary-dominated two-phase flow modeling in porous media using Starfish. *Journal of Petroleum Exploration and Production Technology*, 9(2):1211–1223, 2019. doi: 10 1007/s13202-018-0529-1.

[178] Hu Dong. *MICRO-CT IMAGING AND PORE NETWORK EXTRACTION.* PhD thesis, Imperial College London, 2007.

[179] Abhinav Hazarika. VOF Modelling of Two-phase Flow Inside Porous Transport Layer Reconstructed from CT Images. Master thesis, RWTH aachen University, 2017.

[180] Simson Julian Rodrigues. Simulation of Two-phase Flow Inside of PEM Electrolyzer Porous Electrodes. Master's thesis, Otto Von Guericke University, 2019.

[181] *ANSYS ICEM CFD 14.5 User Manual.* ANSYS Inc., 2012.

[182] Nagadatta Madhu. Measurement of Relative Permeability of Porous Electrodes. Master's thesis, Otto-von-Guericke Universität, 2019.

[183] J. Geertsma. Estimating the Coefficient of Inertial Resistance in Fluid Flow Through Porous Media. *Society of Petroleum Engineers Journal*, 14(5):445–450, 1974. doi: 10 2118/4706-pa.

[184] S. E. Buckley and M. C. Leverett. Mechanism of Fluid Displacement in Sands. *Transactions of the AIME*, 146(01):107–116, 1942. doi: 10 2118/942107-g.

[185] M. Honarpour and S. M. Mahmood. Relative-Permeability Measurements: An Overview. *Journal of Petroleum Technology*, 40(08):963–966, 1988. doi: 10 2118/18565-PA.

[186] J. S. Osoba, J. G. Richardson, J. K. Kerver, J. A. Hafford, and P. M. Blair. Laboratory Measurements of Relative Permeability. *Petroleum Transactions, AIME*, 192: 47–56, 1951. doi: 10 2118/951047-g.

[187] T. M. Geffen, W. W. Owens, D. R. Parrish, and R. A. Morse. Experimental Investigation of Factors Affecting Laboratory Relative Permeability Measurements. *Petroleum Transactions, AIME*, 192:99–110, 1951.

[188] Jan H. van Lopik, Roy Snoeijers, Teun C. G. W. van Dooren, Amir Roof, and Ruud J. Schotting. The Effect of Grain Size Distribution on Nonlinear Flow Behavior in Sandy Porous Media. *Transport in Porous Media*, 120(1):37–66, 2017. doi: 10 1007/s11242-017-0903-3.

[189] Lidia Bloshanskaya, Akif Ibragimov, Fahd Siddiqui, and Mohamed Y Soliman. Productivity Index for Darcy and pre-/post-Darcy Flow (Analytical Approach). *Journal of Porous Media*, (January), 2015. doi: 10 1615/JPorMedia v20 i9 10.

[190] Ulla Panchenko. *Massentransportphänomene in Schichtsystemen eines Elektrolyseurs.* PhD thesis, RWTH Acchen University, 2019.

[191] Multiphase model. Online, 2020. URL https://github com/PMEAL/OpenPNM/blob/dev/openpnm/models/physics/multiphase py. Last Checked 2020-11-20.

[192] Dortmund Databank, 2020. URL http://www ddbst com/en/EED/PCP/VIS_C95 php. Last checked 2021-01-18.

List of Figures

List of Tables

Abbreviations

PEM	**P**roton **E**xchange **M**embrane
PTL	**P**orous **T**ransport **L**ayer
GDL	**G**as **D**iffusion **L**ayer
SOEC	**S**olid **O**xide **E**lectrolysis **C**ell
SPE	**S**olid **P**olymer **E**lectrolyte
PEMFC	**P**roton **E**xchange **M**embrane **F**uel **C**ell
CT	**C**omputer **T**omography
CL	**C**atalyst **L**ayer
PFS	**P**er**F**louro**S**ulfonate
SPEEK	**S**ufonated **P**olytheretherketone
CCM	**C**atalyst **C**oated **M**embrane
CCG	**C**atalyst **C**oated **G**DL
HER	**H**ydrogen **E**volution **R**eaction
OER	**O**xygen **E**volution **R**eaction
VOF	**V**olume **O**f **F**luid
HRIC	**H**igh **R**esolution **I**nterface **C**apturing
CICSAM	**C**ompressive **I**nterface **C**apturing **S**cheme for **A**rbitrary **M**eshes
CSF	**C**ontinuum **S**urface **F**orce
CSS	**C**ontinuum **S**urface **S**tress
FDM	**F**inite **D**ifference **M**ethod
FVM	**F**inite **V**olume **M**ethod
BEM	**B**oundary **E**lement **M**ethod
FEM	**Finite** **E**lement **M**ethod
LBM	**L**attice **B**oltzmann **M**ethod

CFD	**C**omputational **F**luid **D**ynamics
PNM	**P**ore **N**etwork **M**odel
LGCA	**L**attice **G**as **C**ellular **A**utomata
SIMPLE	**S**emi **I**mplicit **M**ethod for **P**ressure **L**inked **E**quations
PTFE	**P**oly**T**etra**F**luoro**E**thylene
REV	**R**epresentative **Element****V**olume
MB	**M**aximal **B**all
SNOW	**S**ub**N**et of the **O**versegmented **W**atershed
MFC	**M**ass **F**low **C**ontroller
JBN	**J**ohnson **B**ossler **N**eumann

Band / Volume 534
Techno-economic Assessment of Hybrid Post-combustion Carbon Capture Systems in Coal-fired Power Plants and Steel Plants
Y. Wang (2021), IV, xx, 230 pp
ISBN: 978-3-95806-545-1

Band / Volume 535
Wissenschaftliche Begleitstudie der Wasserstoff Roadmap Nordrhein-Westfalen
S. Cerniauskas, P. Markewitz, J. Linßen, F. Kullmann, T. Groß,
P. Lopion, P-M. Heuser, T. Grube, M. Robinius und D. Stolten
(2021), IV, 89 pp
ISBN: 978-3-95806-547-5

Band / Volume 536
High-Resolution Photocurrent Mapping of Thin-Film Silicon Solar Cells Using Scanning Near-Field Optical Microscopy
Z. Cao (2021), xiii, 148 pp
ISBN: 978-3-95806-548-2

Band / Volume 537
Kompressionseigenschaften der Gasdiffusionslage einer Hochtemperatur-Polymerelektrolyt-Brennstoffzelle
E. Hoppe (2021), viii, 153 pp
ISBN: 978-3-95806-549-9

Band / Volume 538
Transparent Passivating Contact for Crystalline Silicon Solar Cells
M. Köhler (2021), 186 pp
ISBN: 978-3-95806-550-5

Band / Volume 539
Distribution of trace gases with adverse effects on fuel cells
D. Klemp, R. Wegener, R. Dubus, L. Karadurmus, N. Kille, Z. Tan (2021),
160 pp
ISBN: 978-3-95806-551-2

Band / Volume 540
Cyclotron Irradiation on Tungsten & Co-relation of Thermo-Mechanical Properties to Displacement and Transmutation Damage
R. Rayaprolu (2021), xiv, 211 pp
ISBN: 978-3-95806-552-9

Band / Volume 541
Smart Energy in Haushalten:
Technologien, Geschäftsmodelle, Akzeptanz und Wirtschaftlichkeit
H. Shamon, T. Rehm, B. Helgeson, F. Große-Kreul, M. Gleue, U. Paukstadt, G. Aniello, T. Schneiders, C. Frings, A. Reichmann, A. Löschel, T. Gollhardt, W. Kuckshinrichs, K. Gruber, P. Overath, C. Baedeker, F. Chasin, K. Witte, J. Becker
(2021), VI, 142 pp
ISBN: 978-3-95806-554-3

Band / Volume 542
Deployment Status of Fuel Cells in Road Transport: 2021 Update
R. C. Samsun, L. Antoni, M. Rex, D. Stolten (2021), 37 pp
ISBN: 978-3-95806-556-7

Band / Volume 543
Processing and creep resistance of short SiC fiber containing Ti_3SiC_2 MAX phase composites
A. Dash (2021), vii, 125 pp
ISBN: 978-3-95806-558-1

Band / Volume 544
Synthese und Charakterisierung von Geopolymeren für die Entsorgung der Spaltprodukte ^{137}Cs und ^{90}Sr
S. K. Weigelt (2021), VI, 186 pp
ISBN: 978-3-95806-559-8

Band / Volume 545
Potential depletion of ozone in the mid-latitude lowermost stratosphere in summer under geoengineering conditions
S. Robrecht (2021), 185 pp
ISBN: 978-3-95806-563-5

Band / Volume 546
Two-phase Flow in Porous Transport Layers of Polymer Electrolyte Membrane Electrolysers
D. Borah (2021), xi, 196 pp
ISBN: 978-3-95806-564-2

Weitere ***Schriften des Verlags im Forschungszentrum Jülich*** unter
http://wwwzb1.fz-juelich.de/verlagextern1/index.asp

Energie & Umwelt / Energy & Environment
Band / Volume 546
ISBN 978-3-95806-564-2

Mitglied der Helmholtz-Gemeinschaft

JÜLICH
Forschungszentrum